Nuclear excitation functions for medical isotope production: Targeted radionuclide therapy via $^{\mathrm{nat}}\mathrm{Ir}(d,x)^{193\mathrm{m}}\mathrm{Pt}$

by

Hannah Lovise Okstad Ekeberg

Thesis

for the degree of

Master of Science

Faculty of Mathematics and Natural Sciences
University of Oslo

June 2020

Abstract

This thesis was motivated by the need to measure the ^{nat}Ir(d,x) reactions for a better characterization of their experimental cross sections. A special emphasis was drawn to improving the nuclear data to support optimized production pathways of the medically-valuable auger-emitting radionuclide ^{193m}Pt. ^{193m}Pt is believed to have therapeutic potential when labelled to the chemotherapeutic drug cisplatin. This thesis is a part of larger campaign to yield well-characterized cross sections for novel medical radionuclides. A stack of ten natural iridium (99.9% purity) foils were irradiated with a 33 MeV incident deuteron beam at the Lawrence Berkeley National Laboratory's 88-Inch Cyclotron. This experiment has resulted in measurements spanning approximately 5-30 MeV in the activated foils as the beam energy decreased with the deuterons traversing through the foils. In addition, ten monitor foils of nickel and copper and three monitor foils of iron were placed within each compartment of iridium, to measure the deuteron current in each compartment, via the well-characterized monitor reactions ^{nat}Ni(d,x)^{61}Cu,^{56,58}Co, ^{nat}Cu(d,x)^{62,63,65}Zn and ^{nat}Fe(d,x)^{56}Co. Products from reactions in the monitor foils are also reported to increase the amount of deuteron-induced nuclear reaction data. The deuteron-induced activity in each foil as a function of time since end-of-beam was obtained using gamma-ray spectroscopy with pre-calibrated high purity germanium detectors. The measured activities were fitted to decay curves to find the activity at end-of-beam. Along with the weighted average beam currents measured using the monitor reactions, the flux weighted cross sections were calculated for each observed reaction channel. This work, along with previous experimental data suggests an energy window between 11–18 MeV which maximises the production of ^{193m}Pt, while minimizing contamination from competing reaction channels. In addition, the use of an enriched ^{193}Ir target would suggest that the radiopurity and specific activity of ^{193m}Pt could be further improved by reducing unwanted production of the radio-contaminant ^{191}Pt. A total of 42 reaction cross sections for deuteron-induced reactions on natural iridium, natural iron, natural nickel and natural copper are reported in this work, including the first experimental measurements of ^{nat}Ir(d,x)$^{188m1+g,190m1+g}$Ir (cumulative), ^{nat}Fe(d,x)^{48}V, ^{51}Cr (cumulative), ^{nat}Ni(d,x)^{56,57,58m,58g}Co (independent) and ^{53}Fe (cumulative). The results are compared to experimental data from the EXFOR database, along with the results from the nuclear reaction modelling codes TALYS-1.9, TENDL-2019, CoH-3.5.3, ALICE-2017 and EMPIRE-3.2.3. The experimental results from cross section experiments are important feedback to improve the codes globally, but particularly for reactions in the A=190 region, which proves difficult to model using CoH-3.5.3. This work illustrates another example of the lack of predictive capabilities for this set of modern nuclear reaction modelling codes.

Acknowledgements

Firstly, I want to say thank you to my supervisors Andrew Voyles and Professor Sunniva Siem, you have both given me excellent, constructive feedback during the writing process. Andrew, thank you for taking the time to answer all of my questions, and giving constructive feedback on my work, in addition to introducing me to this very exciting field of nuclear medicine. Sunniva, thank you for providing the opportunity to do this experiment, including the three months stay I had in Berkeley. I also want to thank the isotope production group in Berkeley, in particular Professor Lee Bernstein, for including me in your group, and to all who helped out during the experiment. In addition, all the people who have made the five years at Blindern to an amazing experience!

Hannah Lovise Okstad Ekeberg

June 14th, 2020

Contents

Chapter 1

Introduction

Nuclear medicine is a fast growing field, with great potential in both diagnostic imaging and therapy, where it is possible to study physiological processes, diagnose and treat diseases [1]. In particular, nuclear medicine has many benefits in diagnosing and treatment of cancer. Targeted radionuclide therapy is an emerging alternative to conventional treatment methods. This therapeutic approach can reduce damage to healthy tissue using short-range radiation from radionuclides coupled with a targeting molecule (called a tracer) which seek out and target cancerous cells through the biochemical pathways in the body. In addition, the use of targeting molecules makes it possible to treat metastasis, potentially even before they are detectable. Conventional methods for treatment can have a large impact on the patient, through radiation exposure of healthy tissue and general cell damage via chemotherapy. According to World Nuclear Association (per May 2020), over 10,000 hospitals utilize medical radionuclides worldwide, where over 90% are for diagnostic procedures [2]. Today, targeted radionuclide therapy is mainly used to treat thyroid cancer, relieve pain from bone metastases, or treat blood disorders [1]. Many potential therapeutic radionuclides are under investigation, and the work presented in this thesis is part of a larger campaign to develop production cross sections for novel potential medical radionuclides. This particular work focuses on the products produced from ^{nat}Ir(d,x), with a special emphasis on the production of the auger-emitter ^{193m}Pt. The cascade of short-range auger electrons emitted in its decay is believed to have great potential in treatment of small metastasis and cell clusters if bound to the cellular DNA [3, p. 493]. The auger-emitter can easily be incorporated into the DNA labelled with the chemotherapeutic drug cisplatin, and a long half-life of 4.33 days [4] allows for high uptake in the desired tissue.

Cancer is a collective term for cellular diseases, where a tumor arises due to uncontrolled cell division. Malignant cancer spreads over time by invading nearby tissue or use the blood or lymphatics systems to spread to other organs in the body [5, p. 295]. Cancer is a global health problem, and according to WHO, in

2018, cancer was responsible for approximately 9.6 million deaths worldwide [6]. Per 2012, more than 3.7 million were diagnosed with cancer annually, with more than 1.9 millions deaths per year in Europe alone [7]. The numbers are high, but with development of methods for treatment and early diagnosis, there is a wide range of opportunities to fight these cellular diseases.

The field of nuclear medicine is a diciplnary of multiple scientific fields, involving medicine, physics, chemistry and biology. Before a radionuclide can be used clinically, a production route yielding high specific activity, purification of the radionuclide, labelling to a targeting molecule and finally delivery to the desired tissue must be well-established, and the radiation effects and uptake must be accurately known. The wide range of radionuclides with promising characteristics such as half-life, decay mode and chemical properties make it possible to use a radionuclide coupled with a suited tracer. This can give a personalized treatment for the patient, dependent on cancer type, location and state of disease.

To utilize the characteristics of a radionuclide, the decay data (decay mode, radiation energy, half-life, etc) must be precisely known. In addition, the nuclear reaction data is necessary, for the optimization of the production, achieving maximum yield combined with minimal level of impurities [8, p. 3]. For each nuclear reaction, there is an associated energy-dependent excitation function, which yields the probability distribution of the production leading to a specific radionuclide. The excitation function provides information on the energy window that maximises the production. Due to separation difficulties between isotopes of the same element, an energy window which ideally minimizes production of any product of the element formed in the same energy window is desired. By measurements of the reaction cross sections of all products which are activated in a specific energy window, a detailed overview of the radio-contaminants of the same element can be obtained, along with other competing reaction channels. This is typically done with measurements of the induced activity from irradiation of a thin targets [9] Therefore, an important first step for a potential radionuclide is to establish a production route and measure the production cross sections in the appropriate energy region, which is the main focus of this thesis. For charged particles, the use of the stacked target activation method using one incident beam is effective, as it yields multiple cross section measurements using one incident beam, which is why this method was used in this work.

There exists large amounts of information on low-energy neutron induced reactions. For charged particles, the database is not equally well characterized [9]. This is in particular true for deuteron induced reactions, which have been limited by cyclotrons availability to accelerate deuterons. In addition, with a period of "neutron dryness" following research reactors aging [10], it is important to find

alternative routes for neutron induced reactions. Production via accelerators or cyclotrons offers a large variety of production routes only limited by the ion source and the maximum beam energy of the cyclotron, in addition to the availability of the target material. In addition, deuteron and proton induced reactions often lead to a higher yield and purity than other heavier charged particles [8, p. 4].

The proposed production route for ^{193}Ir(d,2n)^{193m}Pt is investigated in this thesis. The experimental data for the reaction is currently limitedto two measurements (over the energy windows: 1.7–38.0 MeV and 17.09–49.50 MeV) [11, 12]. The modern reaction model codes TALYS, CoH, EMPIRE and ALICE [13–17] disagree regarding magnitude and shape of the excitation function. This experiment is a further improvement of the characterization and the accuracy of the cross sections for the ^{nat}Ir(d,x) reaction. Therefore, this thesis work is motivated by two aspects: report a set of cross sections measurements for the ^{nat}Ir(d,x) reactions using the stacked target activation method, with a special emphasis on the production of ^{193m}Pt. In addition to iridium targets, the stack consisted of monitor foils for precise determination of the deuteron beam current through the stack. The products from the monitor foil reactions: ^{nat}Fe(d,x), ^{nat}Ni(d,x) and ^{nat}Cu(d,x) are reported to strengthen the nuclear reaction database of deuterons.

This thesis proceeds in five main parts. The background and concepts in targeted radionuclide therapy is described in chapter 2. Description of the stacked-target activation set-up is represented in chapter 3. Chapter 4 describes the method used for analysis, including analysis of the gamma-ray spectra, calculation of end-of-beam activities from the radionuclides produced in the foils, calculations of deuteron beam current and energy assignments from the monitor reactions and finally calculations of experimental cross sections. In chapter 5 the main results are represented and a discussion of the optimal energy window for production of ^{193m}Pt. Finally, a summary of the main results, along with an outlook for potential future work is represented in chapter 6.

Chapter 2

Background and concepts in targeted radionuclide therapy

This chapter will give an introduction to the concept of targeted radionuclide therapy. Section 2.1 explains the basic concept of this treatment approach. Sectuib 2.2 explains how various particles interact in matter, and how this can be utilized in cancer treatment. Section 2.3 gives a brief introduction to how radionuclides are produced today. Section 2.4 introduces nuclear reactions and cross sections. Finally, section 2.5 explains how ^{193m}Pt can be used as a therapeutic agent.

2.1 Targeted radionuclide therapy

Today, multiple options for treatment of cancerous tissue are available. Chemotherapy, surgery, external beam therapy and brachytherapy are common treatment methods, and over the recent years targeted radionuclide therapy have gained interest. Ideally, targeted radionuclide therapy should pose the same benefits of chemotherapy (which attacks rapidly dividing cells) and external beam therapy combined. This implies a systematic treatment throughout the body, where cancerous cells in tumor (and metastasis if present) are targeted and exposed to a lethal radiation dose [18]. External beam therapy, brachytherapy and targeted radionuclide therapy utilize ionizing particles to induce damage to the DNA. In external beam therapy, X-rays, high-energetic gamma-rays, or accelerated particles like protons and heavier ions are focused externally towards the tumor. In brachytherapy an unsealed radioactive source (usually a wire or pellet typically containing a β^--emitter), is placed in proximity to tumor [19, p. 2180]. A radiopharmaceutical consists of a radionuclide and a cell-targeting molecule called a tracer. Brachytherapy and targeted radionuclide therapy are limited by the cancer location and the existence of metastasis, along with required knowledge of the

tumor (to maximise the dose over the tumor and minimizing the dose to healthy tissue) [19, p. 2180]. Targeted radionuclide therapy utilizes radiopharmaceuticals which are typically injected intravenously and are transported to desired cells or location with the biochemical pathways in the body. Thus with an appropriate tracer, targeted tissue with a high uptake of the radiopharmaceutical will receive a high dose, and healthy tissue can be spared [10].

A good therapeutic agent should be optimized so the radiation from the radionuclide has a high probability of being deposited in the tumor and ideally deliver a cytotoxic dose to all cancerous cells within a tumor while sparing all healthy cells. For instance, a high uptake-rate of the tracer suggests a shorter half-life of the radionuclide than slow uptake and long retention in tumor. The decay mode and radiation range need to be in coherence with the size and location. By the use of short-range particles located within or close to cancerous cells, the radiation dose to healthy cells can be minimized. This includes that the uptake is minimal in healthy normal tissue, and both the concentration and retention in the tumor are stable during the decay of the radionuclide [8, p. 2]. Ranges from multi-cellular, cellular and sub-cellular are typically accomplished respectively with β^--particles, α-particles and auger electrons [19, p. 2180-2182]. Figure 2.1 shows how the ranges of β^-, α and auger electrons differ on the cellular scale, where low energetic auger electrons have ranges on the scale of the cellular nucleus, α-particles have ranges on the scale of one or two cell dimension, while high energetic β^--particles have ranges of up to several hundred cell diameters. β^--emitters have traditionally been used in targeted radionuclide therapy. α and auger-emitters are increasing in interest due to their short ranges. The use of them involves that they decay close to the cellular nucleus [8, p. 2-3]. Geometrical factors of both the distribution of the radionuclide and the tumor itself can have an effect on the radiation dose to the tumor. In addition, radionuclides emit radiation isotropically. It is important that the dose distribution over the tumor is homogeneous to assure that all cells are killed, ensuring that there is no relapse and regrowth from untreated cancer cells [19, p. 2183].

Important characteristics for the tracer is: a rapid blood clearance and transport [20, p. 145], high uptake and retention in the tumor [8, p. 2] and tissue-targeting [10]. It can target the desired cells with a specific receptor, enzyme, membrane, transporters or antigens [20, 145]. Radiometals are also used, which consists of a bifunctional chelator, a molecule containing atoms which can donate a lone pair of electrons, like nitrogen, oxygen or sulfur. If the radiometal has an oxidation state of 3^+, it will be tightly bound by the chelator, and can transported to the tumor. Figure 2.2 shows an illustration of how a radionuclide can be transported into the desired cell attached to a chelator, via a specific peptide.

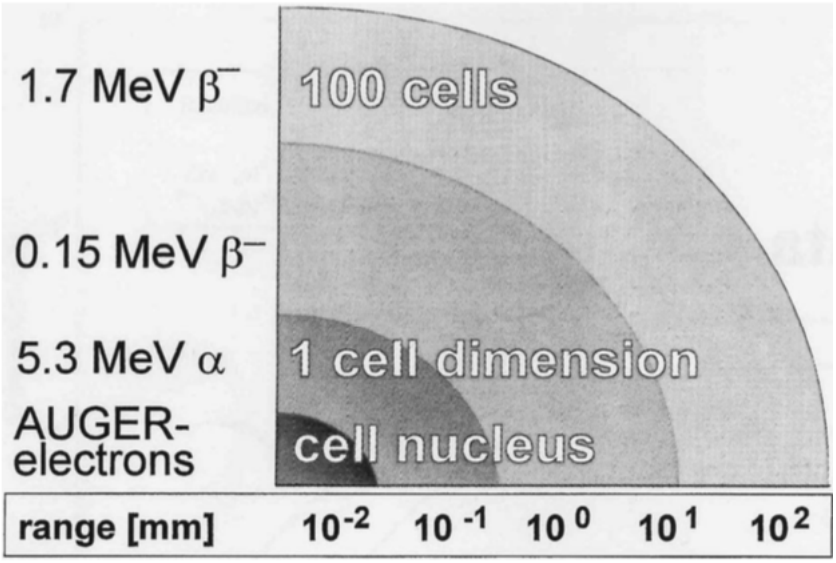

Figure 2.1: The figure illustrates the ranges of auger electrons, 5.3 MeV alpha particles and low and high energetic β^- particles. Figure is from [8, p. 2].

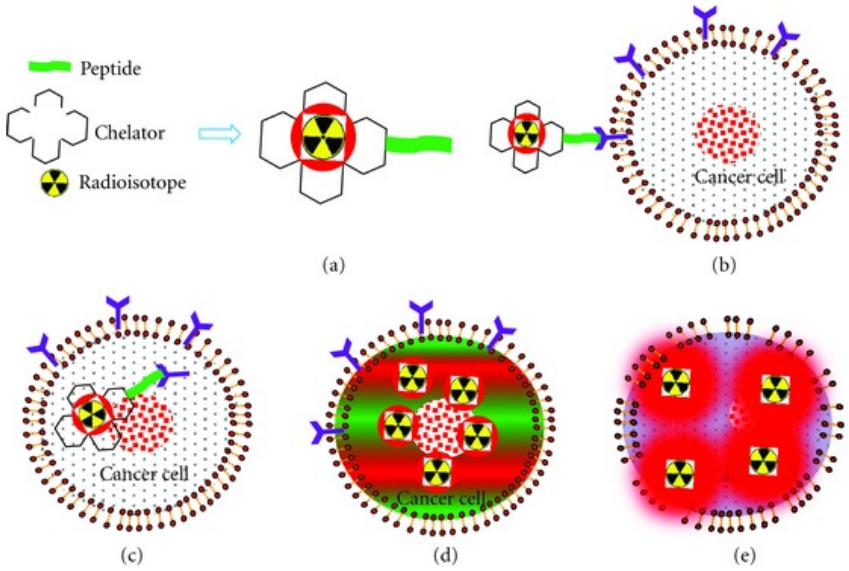

Figure 2.2: A radionuclide is bound to a chelating agent, and with a peptide, the radiopharmaceutical targets the cancer cells. Figure is from [21].

For the radionuclide, along with range and decay mode, the half-life, production method, chemistry and biological behavior are important characteristics [19, p. 2181]. In nuclear medicine, the effective half-life of the radiopharmaceutical

is important as it combines both the physical half-life and the time for the radiopharmaceutical to be cleared or excreted from the body [10]. The physical half-life must be long enough to permit radio-synthesis and quality control, in addition to that the half-life must be long enough for uptake in the desired tissue [19, p. 2185]. At the same time, a high radiation dose to the desired tissue is easier to achieve with a shorter half-life, so there is a fine balance. The choice of radionuclide should match the uptake rate and the retention of the cell-targeting molecule, to avoid radioactive waste handling and dose to healthy tissue [10]. Therapeutic radionuclides typically have half-lives in order of a few hours to several days [8, p. 1]. The chemical-biological properties are also relevant, as it must be chemically possible to attach radionuclide to the targeting molecule. In addition, the binding must stay stable over a time period comparable to the physical half-life [19, p. 2185]. The decay product of the radionuclide may be naturally occurring or excreted from the body, toxic, or contribute to an undesired dose.

In addition to therapy, radionuclides can also be used for diagnostic purposes with PET (positron emission tomography) or SPECT (single photon emission tomography). In PET, positron emitters are used where the positron annihilates with an atomic electron close to the site of decay, emitting two 511 keV photons co-linear in opposite directions. In SPECT, only a single gamma-ray is observed. PET provides a better resolution, but SPECT is cheaper and is therefore the most used imaging method. The combination of both, an imaging and a therapeutic agent, with similar chemical properties coupled to the same targeting molecule yields information of how the uptake is distributed in the body, and that the desired tissue is targeted. This is a relatively new approach called theranostics, and an imaging and therapeutic agent is called a theranostic pair [22]. Ideally, coupling an imaging agent to a therapeutic agent is the ultimate goal for treatment with radionuclides [18].

2.2 Particle interaction in matter

Ionizing radiation are particles with sufficient energy to cause ionizations along the particle track, thus separating one or more electrons from the atoms. The free electron(s) can ionize further, and the positive ion can cause undesired reactions. DNA is a large molecule with two strands bound in a double helix structure. Each strand is composed of sugar and phosphate groups, and nitrogenous bases which bind the two strands [5, p. 11]. These bases are called adenine & guanine and cytosine & thyamine (always bound pairwise), and are bound through weak hydrogen bonds which are exposed for strand breaks. The cell is equipped with an impressive repair mechanism, and unless both strands of the DNA are damaged, a double stranded break, most damages are repaired. Radiation damages in the DNA can be caused directly by the ionizing particle or indirectly via free

radicals. Since the body contains large amounts of water, ionization of water molecules giving for instance $H^{\bullet}$ or $OH^{\bullet}$ are important damaging factors. Damages induced in the DNA can be lethal to the cell and either cause apoptosis or mutation in which can cause cancer. In therapy, the goal is to make malignant cells undergo apoptosis, thus DNA is referred to as the target [5, p. 9]. Choosing a particle with a high probability of inducing damage will induce multiple double stranded breaks if passing near by.

Linear energy transfer (LET) describes the energy absorbed by the medium, and is defined as the average energy deposited per unit length of the material [5, p. 101].

$$\text{LET} = \frac{dE}{dx} \tag{2.1}$$

To maximise the chances of inducing damages in the DNA and minimizing exposure of healthy tissue, choosing a particle with a high linear energy transfer is important in targeted radionuclide therapy. Figure 2.3 illustrates how β^--particles, alpha-particles and auger electrons deposit energy on the scale of DNA, where it can be seen that the α-particle has a much higher LET-value than the β^--particle. Auger electrons typically have energies in the eV-range, and can have a large damaging effect when bound to the DNA with a high energy deposition over a short range.

β-decay occurs whenever there is an excess in the number of neutrons or protons. The two decay modes are β^- and β^+-decay, where the former transforms a neutron into an electron, proton and an antineutrino (β^--decay):

$$n \rightarrow p + e^- + \overline{\nu_e}$$

β^+ decay transforms a proton into a positron, neutron and a neutrino (β^+-decay):

$$p \rightarrow n + e^+ + \nu_e$$

Since the neutron mass is higher than proton mass, the access energy required to run the reaction must be present in the binding energy. Otherwise electron capture (ϵ) occurs. An electromagnetic interaction between an atomic electron (creating a vacancy in the atomic shells) and a nuclear proton that transform into a neutron and a neutrino:

$$p + e^-_{\text{atomic}} \rightarrow n + \nu_e$$

For β-decay, the energy is distributed between three particles, thus the en-

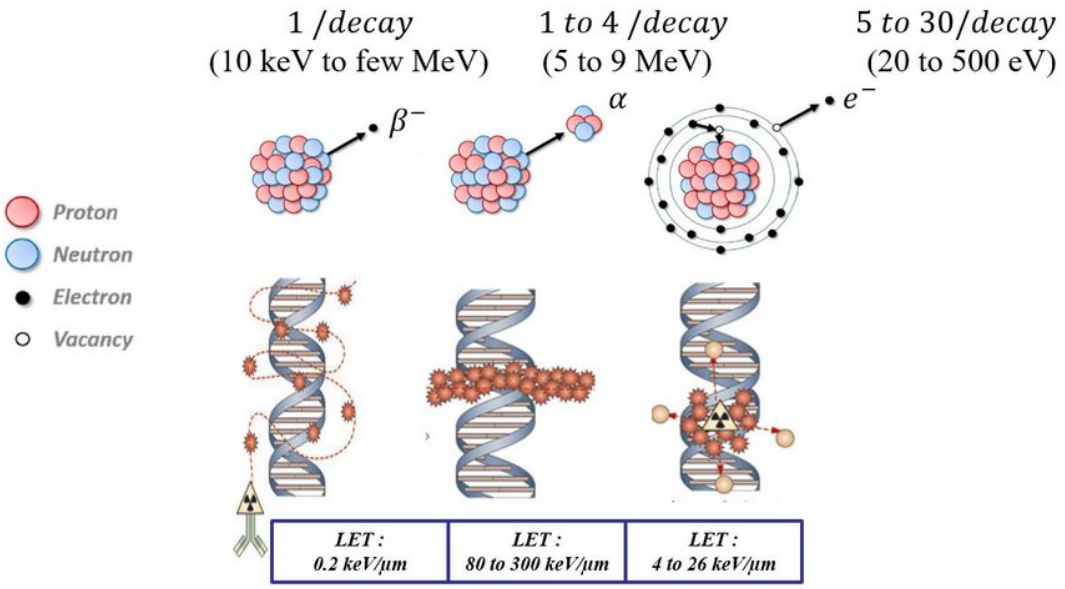

Figure 2.3: The figure illustrates how β^--particles (left), α-particles (center) and auger electrons (right) deposit their energy on the scale of DNA. The figure is assembled from [23], where the upper figure is from [24], and the lower figure is from [25].

ergy of the β-particle is not discrete. α-decay occurs for heavy nuclei where the Coulomb repulsion becomes significant. Thus emission of an alpha particle lowers the binding energy as the alpha particle carries a large amount of binding energy. The energy of the α-particle is discrete which can be detected using spectroscopy. From β and α decay, the daughter nucleus may be left in an excited state which decay by gamma-emission. Auger electrons are result from electron capture or internal conversion, which happens when a gamma-ray interacts electromagnetically with an atomic electron which is emitted. The vacancy in the atomic shell, caused by either reaction, can lead to a cascade of X-rays and auger electrons with energies in the X-ray range. These energies are discrete (as the X-ray energies is discrete). Auger electrons resulting from isomer transition is further described in section 2.5 [26, Chapters 8, 9, 10].

A medium consists of positively charged nuclei and negatively charged electrons. Charged particles have a short range in a medium compared to neutral particles, as the Coulomb force forces the particle to interact continuously along the path mainly with the atomic electrons. While Equation 2.1 describes the energy transferred per unit length (LET), the stopping power describes the energy loss of a charged particle per unit distance. The collision loss for heavy charged particles (protons and heavier ions) at high energies is therefore low. The stopping power for heavy charged particles is described by Bethe-Block ([27,

p. 24]):

$$-\frac{dE}{dx} = 2\pi N_a r_e^2 m_e c^2 \rho \frac{Z}{A}\frac{z^2}{\beta^2}\Big[\ln\Big(\frac{2m_e\gamma^2 v^2 W_{\max}}{I^2}\Big) - 2\beta^2 - \delta - 2\frac{C}{Z}\Big] \tag{2.2}$$

where

r_e : classical electron radius
m_e : electron mass
N_a : Avogadro's number
I : mean excitation energy
Z : atomic number of absorbing material
A : atomic weight of absorbing material
ρ : density of absorbing material
z : charge of incident particle
δ : density correction
C : shell correction
$W_{\max}$: maximum energy transfer in each collision
$\beta = v/c$: incident velocity of the particle
$\gamma = \frac{1}{\sqrt{1-\beta^2}}$: Lorentz factor

As the particle slows down, the more energy per unit length will be deposited, as the charged particle picks up electrons. This is known as the Bragg peak, where most of the energy is deposited, which is located right before the particle stops. The stopping power of heavy charged particles is proportional to the charge of particle and the inverse velocity squared. Therefore, particles with a higher charge will have a higher and narrower Bragg-peak and a shorter range in tissue, with the same initial energy. This behaviour of heavy charged particles is especially useful in external beam therapy and is utilized to have a high dose over tumor and minimal dose elsewhere [27, p. 27-28]. Electrons lose energy fast in matter, either from collisions with atomic electrons or electromagnetic radiation (bremsstrahlung). However, for energies up to a few MeV, the collision energy loss dominates [27, p. 37]. Therefore, electrons have short ranges and have large deflection angles.

Photons and neutrons on the other hand are neutrally charged particles and are not energy-degraded. Instead neutral particles are attenuated as a function of distance traversed, x and the absorption coefficient μ of the material:

$$I = I_0 e^{-\mu x} \tag{2.3}$$

where I is the intensity as a function of distance and I_0 is the intensity at x=0 [27, p. 53]. As gamma-emitters are not directly used in targeted radionuclide therapy, the dose from gamma-radiation following α or beta decay, or X-rays following electron capture or internal conversion needs to be taken into account.

2.3 Production of radionuclides

The radionuclide availability is an important factor in nuclear medicine. Reactors, cyclotrons and natural decay chains have traditionally been used as radionuclide sources [19, p. 2185]. Proton rich nuclei are typically produced in accelerators/cyclotrons using positively charged particles, and neutron rich nuclei are typically been products of fission or produced in the neutron flux from fission in a reactor. Thus therapeutic β^--emitters have traditionally been produced in reactors [9]. With research reactors today aging [10], alternative production routes to produce critical medical radionuclides are important. There is in particular a concern of a shortage of the important SPECT radionuclide ^{99m}Tc, produced in a generator system with the reactor-produced ^{99}Mo as parent nucleus [9]. For clinical applications, the quantities needed for for treatment need to be produced large scale. Prior to this stage, knowledge about the production such as target design, beam energy and particle type, radionuclide yield and purity and radio-chemical separation must be well-established [28], yielding a high specific activity.

There are sometimes several different production routes available for a single radionuclide, dependent on the choice of target (which should have a high natural abundance to avoid large costs related to targetry), particle beam and beam energy. The production route has an associated reaction cross section which is dependent on the beam energy. The nuclear cross section data is very important in optimization of production processes, achieving the maximum yield of the desired radionuclide combined with the minimum level of radionuclidic impurities [8]. It is impossible to chemically separate isotopes of the same element [9]. We want to be sure that what is injected into the patient does not have isotopic impurities which gives undesired dose to the tissue, nor isotopes with no therapeutic effect. This is to yield effective treatment, but especially in cases where the product nucleus is not naturally excreted from the body, which may result in toxicity effects . The only option to minimize isotopic impurities is to choose an appropriate energy window. Production of medical radionuclides should be cheap and available for everyday medical purposes. Accelerators can be small in size and handled easily by medical personnel. Many hospitals which performs nuclear medicine even have a cyclotron facility on site, which is advantageous as its practical to avoid travelling logistics and to have medical radionuclide supply in proximity of examination/treatment site.

2.4 Nuclear reactions and reaction cross sections

A nuclear reaction occurs when an interaction between two nuclei or a nucleus and a subatomic particle takes place. A nuclear reaction is denoted as:

$$X(a,b)Y \tag{2.4}$$

where X is the target, a is the incoming particle, b is the outgoing decay channel and Y is the product of the nuclear reaction [26, p. 378].

In a nuclear reaction, the total energy and linear momentum, proton and neutron number, angular momentum and parity are conserved quantities (assuming no meson formation) [26, p. 380]. A nuclear reaction can be a compound-reaction, pre-equilibrium-reaction or direct-reaction [29]. The compound nucleus model describes the formation of a compound nucleus by absorption of an incoming particle by a nucleus. The kinetic energy shared between the incoming particle and the nucleon which was struck leads to multiple collisions with other nucleons and rapid exchange of energy, achieving thermal equilibrium. The energy is distributed throughout the nucleus, leaving the original nucleus in an highly excited state. There is a statistical probability that enough energy will be concentrated on one single nucleon or group of nucleons such as protons, neutrons and α-particles, and escape the potential barrier of the nucleus (also refereed to as evaporation), which lowers the excitation energy [26, p. 416]. Since the nucleons collides rapidly, the information regarding the initial energy and the direction of the incoming particle is lost, and the outgoing decay channel depends only on conservation of the energy and angular momentum. Figure 2.4 shows an illustration of a ^{10}B nucleus interacting with a deuteron (^{2}H) in four different reactions. As illustrated, compound nuclear reactions can be divided into two stages; fusion of incoming particle and target nucleus, and evaporation of nucleons or groups of nucleons. A direct reaction involves interaction with single nucleons, and can be elastic, transfer or break up, as shown in Figure 2.4. Since the incoming particle interacts with a single nucleon, the exit channel depends heavily on conservation of spin and parity, in addition to energy and mass. An intermediate reaction between compound and direct reactions are the pre-equilibrium reactions, where the incoming particle does not lead to a thermal equilibrium, but the information of initial energy and direction is lost [29]. In this work, the reaction type or reaction channel is not distinguished. The total cross section of the formation of the product is reported. In the excitation function, the compound peak along with pre-equilibrium tale are observed.

A Nuclear reaction cross section represents the total probability that a nuclear reaction will occur. A way to visualize a nuclear reaction cross section is by

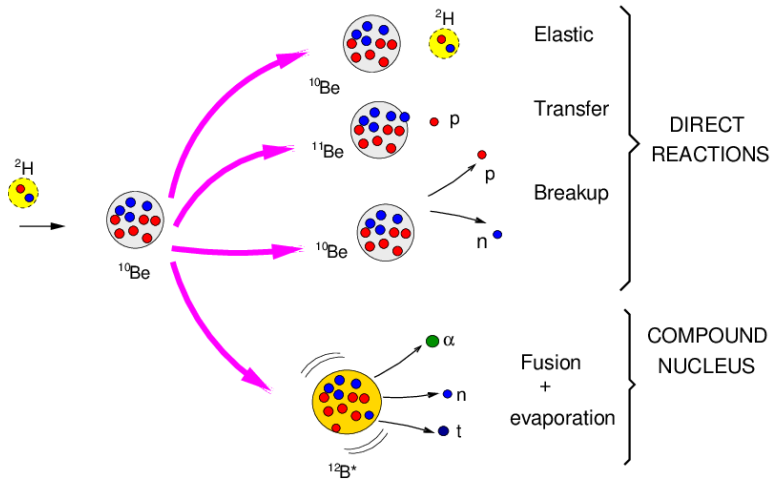

Figure 2.4: The figure shows how direct and compound nuclear reactions differ. Figure is from [30].

imagining the incoming particle and the target nucleus as spheres, and if they overlap, the reaction will occur. The total reaction cross section is therefore proportional to the cross-section area of the two spheres:

$$\sigma_R = \pi r_0^2 (A_X^{1/3} + A_a^{1/3})^2 \tag{2.5}$$

where r_0 is a constant (≈ 1.6 fm), A_X and A_a are the atomic mass number of target A and incoming particle a, and the radii of the nuclei are connected via $r_0 A^{1/3}$. The unit of a cross section is therefore in a unit of area, typically in millibarn ($1 \cdot 10^{-27}\text{cm}^2$) [31, p. 8]. The total reaction cross section between the incoming particle and the target nucleus is a more or less constant value, with the summation of the various nuclear reactions which can take place:

$$\sigma_{\text{tot}} = \sum_b \sigma(a, b) \tag{2.6}$$

The nuclear reactions can for instance be elastic and inelastic scattering:

$$X(a, a)X, \quad X(a, a)X^*)$$

radiative capture:

$$X(a, \gamma)Y$$

and absorption and compound nucleus formation:

$$X + a \rightarrow C^* \rightarrow Y + b$$

t When irradiating a target X with a particle beam a, there are sometimes multiple possible decay channels leading to one particular product Y. If a reaction cross section is denoted as $X(a,x)Y$, x represents different decay channels leading to the same product nucleus. The cross section for a nuclear absorption reaction to occur via the formation of the compound nucleus by the collision of a particle with a target nucleus, and the decay of the compound nucleus via decay channel b can be expressed as:

$$\sigma(a,b) = \frac{\sigma_c P_b}{\sum_b P_b} \tag{2.7}$$

The cross section of a certain reaction (in a thin target) to take place can be estimated based on the production rate, the number of target nuclei, the beam flux or beam current ([26], chapter 6)

$$\sigma(E) = \frac{R}{N_T \cdot \Phi} \tag{2.8}$$

Based on the induced activity in the target, the irradiation time and decay product nuclei during irradiation, the cross section can be find experimentally, with gamma-ray spectroscopy, which is used in this work:

$$\sigma(E) = \frac{A_0}{N_T \cdot \Phi(E)(1 - e^{-\lambda t_{\text{irr}}})} \tag{2.9}$$

where A_0 is the end of beam activity of the resulting product nucleus (Y) (the end of beam activity is $A_0 = R(1 - e^{-\lambda t_{\text{irr}}})$), t_{irr} is the irradiation time, N_T is the number of target nuclei (X), $\Phi(E)$ is the particle flux or current, and λ is the decay constant of the product nucleus.

2.4.1 Constraints in nuclear reactions

In a nuclear reaction, the mass-energy is conserved, which is denoted as the Q-value. The reaction Q-value is the mass difference before and after the nuclear reaction occurred [26, p. 381]. It is defined as:

$$Q = (m_i - m_f)c^2 = (m_X + m_a - m_Y - m_b)c^2 \tag{2.10}$$

where m_i is the initial mass, m_f is the final mass and c is the speed of light. If $Q > 0$, the reaction is exoergic, which means that energy is released in the reaction. There is no threshold energy of the incoming particle required for the reaction to occur. If $Q < 0$, the reaction is endoergic, which means that the

kinetic energy of the incoming particle is converted into nuclear mass or binding energy. For endoergic reactions to occur, there is a minimum threshold energy of the particle in order for the reaction to happen, which is defined as [26, p. 382]:

$$E_{\text{threshold}} = (-Q) \cdot \frac{m_Y + m_b}{m_Y + m_b - m_a} \tag{2.11}$$

Emission of protons and neutrons are the simplest decay channels of the compound nucleus, with masses $m_p = 938.28$ MeV/c^2, and $m_n = 939.57$ MeV/c^2 respectively. Emission of α-particles (with a mass difference of $\Delta = 28.3$ MeV/c^2 in comparison to two protons and two neutrons) is a common decay channel due to the large release of binding energy. In addition, tritons (with a mass difference of $\Delta = 8.5$ MeV/c^2 in comparison to two neutrons and one proton) is also common, but the gain is less, and is therefore less probable. Decay with other particles such as deuterons and ^{3}He is also possible, but the cross section is low as other decay routes are favoured. Emission of protons and neutrons are the most heavy fed channels when those are energetically accessible.

The Coulomb barrier of a nuclide is an additional constraint that can have a small impact on the reaction. The height of the Coulomb barrier is dependent on the radius and charge of the incoming or outgoing particle a and the target nucleus X [19, p.155]:

$$U_{\text{Coulomb}} = \frac{1}{4\pi\epsilon_0} \frac{e^2 Z_X Z_a}{r_X + r_a} \tag{2.12}$$

2.4.2 Nuclear reaction models

There exists multiple nuclear reaction models, where the aim is to predict the excitation function for products produced for a particular target and beam. Theoretical nuclear reaction models are important, for understanding the physics behind the results [8, p. 23]. One of the major issues with the reaction modeling codes is that they frequently do not reproduce experimental data when it comes to absolute value, location of compound peak and/or the shape. By changing the input parameters it is possible to tune the reaction model to match one product nucleus. The local optimization of that particular product does not improve the code globally. Experimental data are crucial to test reaction models and improve them, improving their predictive powers for reactions which are difficult to measure. Therefore, the codes were ran on default parameters, and not locally optimized. This is also how most other users in medical radionuclide production use these reaction modelling codes.

The reaction models which were used was EMPIRE-3.2.3, CoH-3.5.3, ALICE-2017, TALYS-1.9 and TENDL-2019 [13–17, 32]. The four former codes codes were ran with the same input models used in [33]. TENDL-2019 was taken from the TENDL database. Since this thesis does not focus extensively on the reaction modelling codes, the parameters which goes into the codes will not be described, but can be seen in the references. The TALYS, EMPIRE and CoH reaction modelling codes are based on the Hauser-Feshbach-model [34], and ALICE on standard Weisskopf-Ewing evaporation [35, 36].

2.5 ^{193m}Pt as a potential therapeutic agent

^{193m}Pt has a half-life of 4.33 days, and is an auger-emitting isomer which decays by isomeric transition (100%) to the long-lived ^{193g}Pt groundstate ($t_{1/2}$=50 years) [4]. Radionuclides produced from deuterons on natural iridium such as ^{191}Pt, ^{193m}Pt, ^{192}Ir and ^{194}Ir have potential to be used in medicine, for example in chemotherapy, brachytherapy, radioimmunotherapy and imaging [11]. Platinum radionuclides are of special interest. Platinum is the main element in chemotherapeutic agent cisplatin, a drug which is clinically used in treatment of testicular and ovarian cancer mainly, but also to treat esophagus, head and neck and bladder cancer [37]. Cisplatin (cis-dichlorodiammine platinum(II)) is an inorganic molecule which contains one stable platinum atom surrounded by two chlorine atoms and two ammonia molecules (NH_3). The cisplatin-molecule enters the cell nucleus, and binds to the DNA, example-wise shown in Figure 2.5, where the one or both chlorine-atoms are detached and the platinum-atom binds through covalent bonds to the DNA bases adenine and guanine, and breaks the bonds between the DNA nitrogenous bases. One of the major challenges with cisplatin is the chemical toxicity. However, when auger-emitters such as ^{193m}Pt or another potential auger emitter ^{195m}Pt (not produced via ^{nat}Ir(d,x)) replace the stable platinum atom, the local auger-damage effect increases the chemical damage of cisplatin. The combination of cisplatin and auger-emitting nuclei suggests that a smaller amount of the drug is required, and the toxicity-limitations can be avoided [3, p. 493].

Figure 2.6 represents the three routes which have been investigated for production of ^{193m}Pt. The proposed routes are production via ^{192}Pt(n,γ)^{193m}Pt using a neutron field in a reactor (the green arrow on 2.6) [39], or via ^{192}Os(α,3n)^{193m}Pt using accelerated alpha-particles (red arrow in Figure 2.6), where the highest measured cross section was $\sigma_{36.4\ \mathrm{MeV}}$=1531 mb [40, 41]. In addition, the ^{nat}Ir(d,x)^{193m}Pt reaction cross section have been reported ($\sigma_{12.6\ \mathrm{MeV}}$=233 mb) which is the route further investigated in this thesis (blue arrow in Figure 2.6) [11, 12]. For production of high-spin isomers, such as ^{193m}Pt (with a nuclear spin $13/2^+$), the angular momentum required to connect the target nucleus and

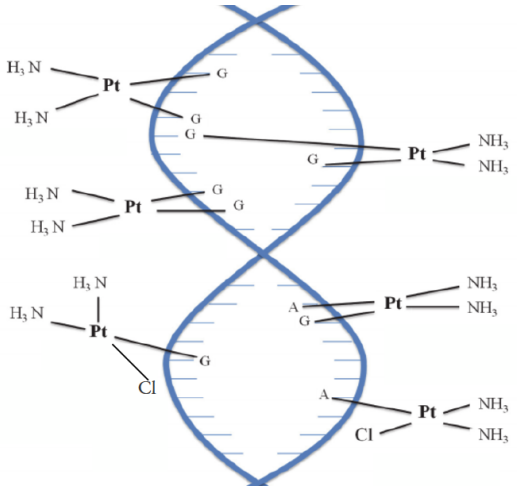

Figure 2.5: The figure shows how cisplatin binds to DNA bases. Figure is adapted from [38].

the product must be sufficient, so that the isomer-to-ground state ratio is large (since production of the ground state contributes as a contaminant). The angular momentum transfer increase with energy, along with mass of the particle. For the first reaction, using low-energetic neutrons produced in a reactor, the reaction will mainly populate the low-spin ground state. In addition, the need of an enriched target will be expensive (^{192}Pt has a natural abundance of 0.782%), and as explained in section 2.3, there is a clear benefit of producing in an accelerator using a charged particle beam. Otherwise, neutron induced reactions using for instance the UC Berkeley High Flux Generator [42] can be investigated, as it can provide high energetic neutrons. ^{192}Os(α,3n) has a high cross section. The alpha-particles transfers large amounts of angular momentum from the mass and the energy, and thus the production cross section of $^{193\mathrm{m}}$Pt is large. The production using α-particles at hospital cyclotrons can be limited by ion source availability and energy. However, the production route using highly toxic material pose challenges for both production of the target, and separation of $^{193\mathrm{m}}$Pt after irradiation. The production route $^{\mathrm{nat}}$Ir(d,x)$^{193\mathrm{m}}$Pt which is further investigated in this thesis demands low-energetic deuterons, and the targetry is more affordable, easier to work with and does not pose challenges related to targetry. However, the production cross section is expected to be less than the suggested route via ^{192}Os(α,3n)$^{193\mathrm{m}}$Pt.

Gamma-decay is a result of de-excitation of a nucleus with the release of a photon equal to the energy difference between the two states. The typical half-life of a populated excited state is less than 10^{-9} seconds, and states with longer half-lives are called isomeric states [26, p. 275], typically denoted with an m, or if a nucleus contains multiple isomer states, $m1, m2$, etc. In all decays, angular

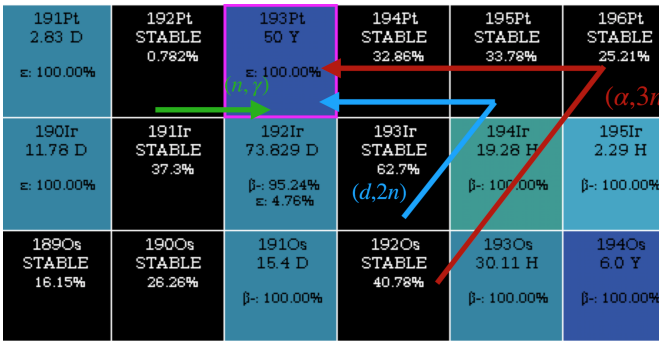

Figure 2.6: The figure shows the three current investigated routes for ^{193m}Pt. The blue arrow shows the production route investigated in this experiment. Figure is adapted from the Nudat 2.8 database [43].

momentum and parity are two properties that must conserved. A multipole of order ℓ transfers angular momentum $\ell\hbar$ per photon [26, p. 333]. A nuclear state has a definite spin and parity, and if a gamma transition is to happen between two states the photon must connect the two states by conserving spin and parity. In order for the spin to be conserved, the angular momentum must be integers between

$$|I_i - I_f| \leq \ell \geq I_i + I_f \tag{2.13}$$

where I_i is initial spin and I_f is final spin. The parity decides whether the radiation is electric multipole (EL) or magnetic multipole (ML) [26, p. 311]. The multipole of the gamma-ray is equal to ℓ.

$$\pi(ML) = (-1)^{\ell+1}, \quad \pi(EL) = (-1)^{\ell} \tag{2.14}$$

There are three populated states for ^{193m}Pt, which can be seen in Figure 2.7. For the decay of ^{193m}Pt (E level=149.8 keV) to the excited state (E level=14.3 keV), the spin and parity changes from $13/2^+$ to $5/2^-$, which gives possible values $\ell = 4, 5, 6, 7, 8, 9$. If the parity is unchanged in the decay ($\Delta\pi$=no), the electric multipoles are even and magnetic multipoles are odd. If the parity does change ($\Delta\pi$=yes) there would be odd electric and even magnetic multipoles. Hence, for the possible transitions between $13/2^+$ to $5/2^-$ are whenever $\Delta\pi$=yes and $\ell = 4, 5, 6, 7, 8, 9$, which gives possible M4, E5, M6, E7, M8 and E9 transitions. In general, the lowest possible multipole dominates, and the emission of a multipole of one higher order ($\ell + 1$ than ℓ) is reduced by a factor ca. 10^{-5} [26, p. 335]. Thus a multipole of order 4 or 5 has a low probability of occurring, and consequently the isomer has a long half-life. The remaining states (E level = 14.3 keV and 1.6 keV) have short half-lives due to possible M1 transitions.

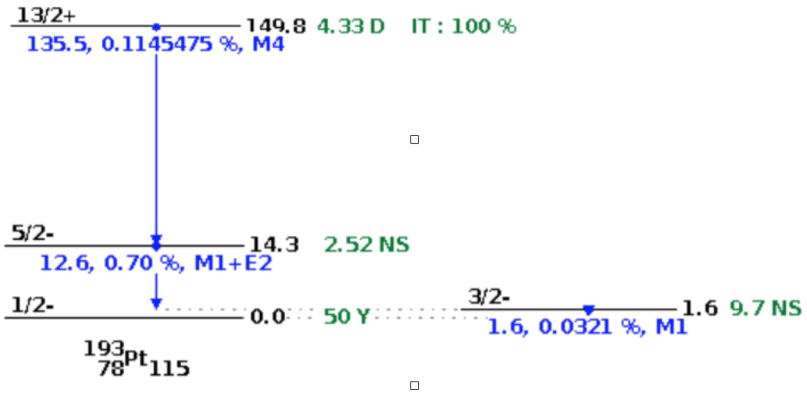

Figure 2.7: The decay scheme of ^{193m}Pt. Figure is adapted from Nudat 2.8 database [43].

The observed gamma-rays emitted from the isomer state (E=149.8 keV) of ^{193m}Pt are very weak. Whenever gamma-decay is possible, another process called internal conversion is competing. It is an electromagnetic process where the nucleus interacts electromagnetically with the atomic electrons, and an atomic electron is emitted instead of the photon ([26, p. 341]. The kinetic energy of the emitted electron is the transition energy minus the electron binding energy:

$$T_{e_C} = \Delta E - B_e \tag{2.15}$$

where B_e is the electron binding energy. The emitted electron is called a conversion electron, and the energy is comparable to the gamma-ray energy.

In general, the probability for internal conversion increases with Z^3, which will give a much greater coefficient for heavy nuclei than for lighter nuclei. In addition the coefficient decreases rapidly (approximately $E^{-2.5}$) with increasing transition energy. The multipole order also affects the coefficient, where a higher multipole order indicates a higher value. For higher atomic shells than the K shell in the atomic orbitals, the coefficient decreases like n^{-3} [26, p. 346].

From a therapeutic point of view, the most important process occurs after the release of the conversion electron. There is a vacancy in the shell following the emission of the atomic electron, and another atomic electron fills this vacancy. To conserve energy, an X-ray with the energy equal to the difference between the electron states is emitted. This X-ray can also interact electromagnetically with an atomic electron, which consequently is emitted if the energy transferred to the

atomic electron is larger than the electronic binding energy. The energy of these electrons are comparable to the X-ray energies which usually have lower energies than the gamma-ray energies (typically less than 100 keV). The origin of the emitted electron make them: Super Coster-Kronig if originating from the same shell, Coster-Kronig if originating from the same subshell, and auger electron if they originate from a higher subshell. In practice, the vacancy moves up to higher atomic shells and the result is a cascade of electrons and Auger electrons, until the reaction "fades out". Due to the low energies of the auger electrons, they need to be located close to the cellular nucleus or incorporated into the DNA to induce damage. When incorporated into DNA they are almost equally effective as α-emitters [44].

While the cell diameter is approximately 100 μm, the cellular nucleus is approximately 6 μm in diameter. The DNA located within the cellular nucleus is approximately 2 nm in diameter. According to Monte Carlo simulations by Howell [45], a total of 3 possible conversion electrons can be emitted per decay with ranges from ca. 0.7 nm-54.7 μm. The long ranges are caused by the 135.5 keV gamma-ray from the isomeric state. An average of 26.4 secondary Auger and Coster-Kronig are emitted per decay. The electrons have ranges from ca. 3.29 nm-64.1 μm. In addition, X-ray energy deposition of 12.345 keV adds to the total energy deposition, which is approximately 126.738 keV from conversion electrons and 10.353 keV from the super Coster-Kronig, Coster-Kronig and Auger electrons. In this energy region, the energy loss from the electrons is due to collisions and not bremsstrahlung, which dominates up to a few MeV. Since the ranges of the electrons following internal conversion is less than the cell's diameter, the dose from auger electrons in the cytoplasm or outside of the cells in blood transportation is very small [46].

Chapter 3

Experimental setup

This chapter provides an overview of the experimental set-up which was used to obtain the cross section measurements presented in this work. The stacked target activation method is described in section 3.1. The facility used to perform these measurements, the Lawrence Berkeley National Laboratory's 88-Inch Cyclotron, is described in section 3.2. The characterization of target and monitor foil is described in section 3.3. An introduction to Gamma-ray spectroscopy with high purity Germanium detectors including energy and efficiency calibration is described in section 3.4. The irradiation of the target stack is described in section 3.5, with the tuning of the beam, irradiation and the quantitative measurement of the spatial beam profile. The analysis of the data is described in chapter 4.

3.1 The stacked target activation method

In this thesis work, the stacked target activation method is used to measure cross sections at multiple energies using a single incident charged-particle beam on a stack of thin targets. In this method, the incident beam energy is degraded as it traverses the stack of targets, causing each foil to be activated with a different energy spectrum. The cross sections (for each observed reaction product) are calculated based on the activation of each product in each foil, resulting in multiple cross section measurements at multiple energies. Similar experiments have taken place at the 88-Inch Cyclotron in recent years [33, 47, 48]. This method relies upon well-characterized foils with accurately measured areal density, and the use of monitor foils in each target compartment, where reactions with well-characterized cross sections are used to measure the beam current in each compartment.

The cross section for a particular reaction product can be calculated from

the activation of a target foil. When a target is exposed to a particle beam which induces various nuclear reactions, the rate of production, R, of a specific reaction is dependent on the number of target nuclei, N_T, the current or flux of the particle beam, Φ, and the reaction cross section, σ:

$$R = N_T \Phi \sigma \tag{3.1}$$

This is the "thin target approximation", which assumes that the beam loses no energy in the target. With the cross section in units of area (typically mb), either target density or beam current density (flux) must be used for the units to be correct. This gives rise to two possible approaches, where the former demands a homogeneous target areal density profile and the latter demands a homogeneous (spatial) intensity profile of the beam (the "underfilled approach"). In the underfilled approach, the spatial profile of the target areal density must be constant (no cracks/bumps etc) and provides a uniform energy loss profile as the beam traverses the target. Thus, the activation and energy degradation is consistent as a function of penetration depth. This is important in the stacked target approach, where the energy degradation needs to be uniform over each foil to activate the foils at a known energy. The contrary is the "overfilled approach", where the target mass is used to calculate the number of target nuclei. It is easier to obtain a homogeneous intensity of the beam with a large spatial beam profile.

Assuming a constant production rate, the number of transformed target nuclei is small in comparison to the total number during the irradiation time. The number of product nuclei present at a particular time $N(t)$ follows the differential equation:

$$dN = Rdt - \lambda N dt \tag{3.2}$$

which has the solution (assuming $N(t = 0) = 0$):

$$N(t) = \frac{R}{\lambda}(1 - e^{-\lambda t}) \tag{3.3}$$

where λ is the decay constant of the nucleus. The activity of a product is defined as the disintegration rate of a nucleus:

$$A = \frac{dN}{dt} = \lambda N \tag{3.4}$$

Equation 3.3 can thus be rewritten connecting the production rate and the activity from Equation 3.3 and Equation 3.4:

$$A(t) = R(1 - e^{-\lambda t}) = N_T \Phi \sigma (1 - e^{-\lambda t}) \tag{3.5}$$

which is valid for the thin-target approximation. At the end of beam, the activity is denoted as A_0, and t_{irr} is the irradiation time:

$$A_0 = N_T \Phi \sigma (1 - e^{-\lambda \Delta t_{\text{irr}}}) \tag{3.6}$$

Solving this equation for cross section, the cross section can be found:

$$\sigma = \frac{A_0}{N_T \Phi (1 - e^{-\lambda t_{\text{irr}}})} \tag{3.7}$$

The term $\Phi(1 - e^{-\lambda t_{\text{irr}}})$ assumes a constant beam current over the duration of the irradiation.

Gamma-ray spectroscopy was used to measure produced activities in the target and monitor foils. The well-characterized cross section reactions $^{\text{nat}}$Fe(d,x)^{56}Co, $^{\text{nat}}$Ni(d,x)^{61}Cu^{56,58}Co and $^{\text{nat}}$Cu(d,x)^{62,63,65}Zn were used to calculate the weighted average beam current throughout each compartment of foils, using IAEA–recommended monitor cross section data [49]. The full stack design can be seen in Table 3.1. The targets were approximately 25 mm by 25 mm in size and 25 μm thick. The beam was approximately 1 cm in diameter, so the beam underfilled the target foils. In addition to the target foils, 316 stainless steel foils were placed in the front and the back of the stack. The stainless steel worked as a beam profile monitor, as the activated foils could be used to develop radiochromic films (Gafchromic EBT3). These films are based upon the use of a dose-proportional dye which develops when exposed to ionizing radiation, which can be used to quantify the relative intensity of the spatial beam profile in the front and in the back of the stack. In addition, a proton degrader (6061 aluminum alloy) and a nickel neutron monitor were placed in the back of the stack. The proton degrader was used to stop any secondary protons from deuteron break-up. The nickel monitor foil was used to screen for the presence of secondary neutrons in the stack. No additional degraders were necessary to further degrade the beam energy, due to the number of target and monitor foils in the stack.

3.2 Lawrence Berkeley National Laboratory's 88-Inch Cyclotron

Lawrence Berkeley National Laboratory (LBNL) [50] is a national research laboratory on behalf of the U.S. Department of Energy through its Office of Science,

and is operated by University of California, Berkeley. LBNL was founded by Ernest O. Lawrence, the inventor of the cyclotron, in 1931 [51]. The 88-Inch Cyclotron has a cyclotron number of K=140, the Cyclotron can accelerate both light and heavy ions up to Uranium [52]. There are multiple research programs in both fundamental and applied nuclear science taking place at the facility, including the Bay Area Nuclear Data group (BAND), superheavy element searches, fundamental nuclear structure experiments, chip and space effects testing, novel scintillation characterization, fission yield (FLUFFY) and neutron inelastic scattering measurements (GENESIS).

A cyclotron is a device that accelerates charged particles. It operates by using an alternating (radiofrequency) electric field, and a perpendicular magnetic field, which causes the particle to accelerate in an outward spiral via the Lorentz force. The layout of the facility is depicted in Figure 3.1, and consists of a cyclotron vault and experimental caves, where cave 01/02 is where the irradiation of the target stack took place in the present work. Cave 4C is currently used for gamma-ray spectroscopy, where 6 high purity germanium detectors used in this work were located. Since it has previously been used as an experimental cave, background radiation is present. In total there are six electrically isolated beamlines leading to radiation chambers. From the cyclotron vault, the particle beam can be tuned and focused to the desired radiation chamber with bending magnets and focusing quadruple magnets. Faraday cups can measure the beam current at different steps along the beamline. Due to scattering, space charge effects and loss of particles (which does not have the desired energy), the beam transmission efficiency is less than 1.

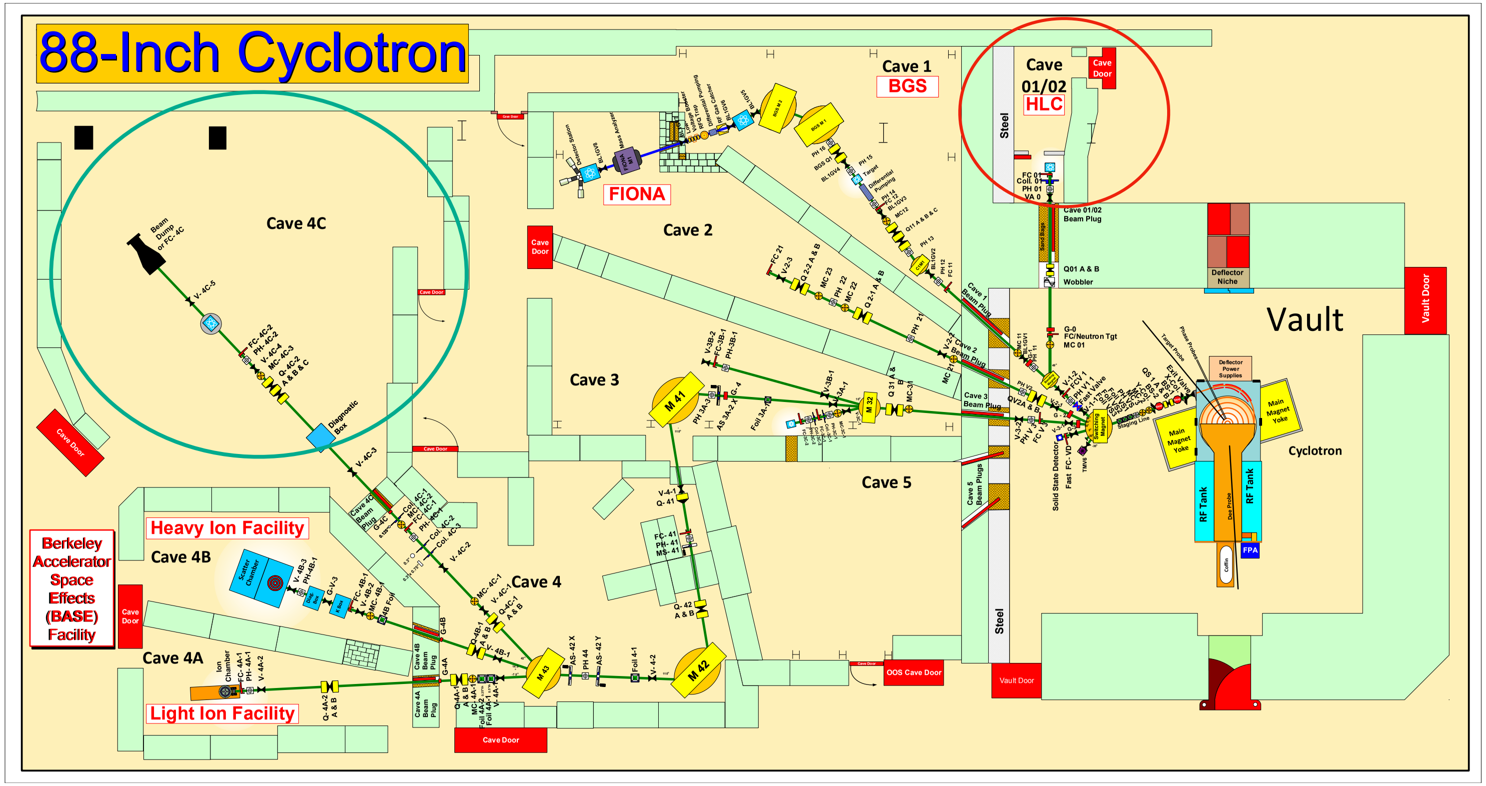

Figure 3.1: An overview of the 88-Inch Cyclotron facility. The facility has several isolated beam lines that can be used for irradiation in the experimental caves. The irradiation of the target stack took place in cave 01/02 (red circle), while some of the detectors used in the gamma-rays spectroscopy was located in cave 4C (green circle) which is no longer used as an experimental cave. Bending magnets are used to steer the beam into the desired beamline, and focusing quadropole magnets are used to focus the beam spot size. Figure is from A. Voyles, personally.

3.3 Characterization of the target and monitor foils

The stack irradiated in this work consisted of ten natural iridium (99.9% purity), ten natural nickel (<99.9% purity), ten natural copper (<99.95% purity) and three natural iron (<99.5% purity) foils[1]. The iridium foils were obtained as pre-cut in 25 by 25 mm squares, and the copper, iron and nickel foils were cut into approximately 25 by 25 mm squares. The length and width of each foil and their thicknesses were measured with a calipers and a digital micrometer[2]. An analytical balance[3] was used to measure the mass of each foil which was prewashed with isopropanol to clear the foils from surface contamination. Each dimension and the average values are listed in Table 3.1. The areal density was calculated for each foil using the average mass of each foil, divided by the average area. The uncertainty for the measured quantities was calculated according to 1σ uncertainties (Equation A.1 in Appendix A). The total uncertainty in areal density was calculated according to Equation A.12.

The areal densities may be converted to number of nuclei per cm^2, which was done by multiplying the areal density with Avogadro's number, and dividing by the molar mass of the target. The measured thicknesses were not used in the analysis, but provide a confirmation that each foil was uniform. The measured values varied from 24.3μm (Ir03) to 34.8 μm (Cu02), which were all within manufacturer specifications.

After the characterization, each foil was mounted on approximately 1.6 mm-thick plastic frames with a hollow aperture approximately 40 mm in diameter with Kapton tape along the edges. From previous experiments, the Kapton tape has been used to seal the foils into airtight pockets for foil containment, but has been shown to provide a systematic uncertainty due to the difficulty of characterizing its charged particle stopping power [33]. Therefore it was not placed over the beam strike area of each foil. The target frames with the mounted foils can be seen in Figure 3.2. The mounted targets were placed in sealed plastic bags until irradiation. For irradiation, the foils were placed in a target holder made from 6060 aluminum alloy with a hollow upstream aperture in the front the beam to pass through. A spring was used to keep the foils stable during the irradiation.

[1] All obtained from Goodfellow Cambridge Limited, Huntington, PE29, 6WR, England.
[2] Mitutoyo Absolute Digimatic, Mitutoyo IP65 Coolant Proof
[3] Mettler Toledo

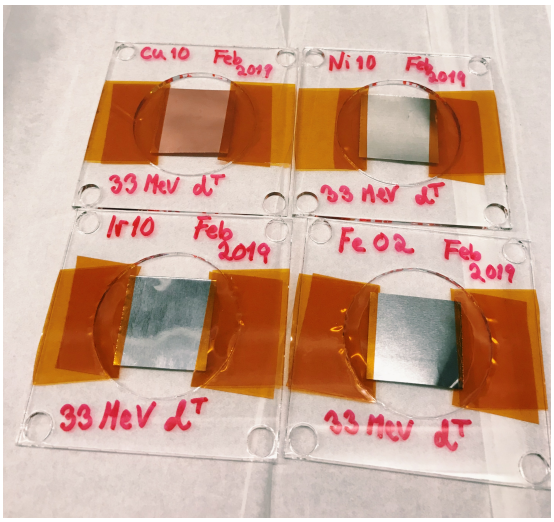

Figure 3.2: The figure shows the four different targets mounted on plastic frames with a hollow center with Kapton tape attached along the edges of the foils.

3.4 Gamma-ray spectroscopy

For quantifying the produced activities via gamma-ray spectroscopy, seven different high purity germanium detectors (HPGe) with coaxial right cylinder geometry were used. Six of the detectors were mechanically cooled p-type Ortec IDM-200V detectors (detectors 1-6) with detector diameter 85 mm, detector length 30 mm, hole depth 15 mm and hole diameter 9 mm. The outside contact layer was doped with lithium, and the hole contact layer with boron. In addition one liquid-nitrogen cooled n-type ORTEC GMX-50220-S detector (detector 7) which had a thin beryllium window for improved X-ray efficiency, with detector diameter 64.9 mm, detector length 57.8 mm, hole diameter 9.4 mm and hole depth 48.6 mm was used. The outside contact layer was doped with boron and the hole contact layer was doped with lithium. The detector volume for detectors 1-6 were approximately 169.996 cm^3 and detector 7 was approximately 190.365 cm^3 (assuming detector hole cylindrical). Detectors 1-6 were mounted in a horizontal point of view, while detector 7 was configured vertically, inside of a lead shielding for low background counts.

The high purity germanium detector is a type of semiconductor, which is a material where the energy required to remove an electron from the valence band (in the outer atomic shell) to the conduction band is small. The atoms in the detector are bound in a crystal structure. The detection mechanism for a semiconductor detector relies upon the creation of electron-hole pairs after energy deposition by an ionizing particle in the crystal. Under the influence

Table 3.1: The table shows the characterization of each target foil, along with calculated areal densities. The stack is organized in the order it was irradiated in, divided into foil compartments. Each length is measured in mm, and mass in grams. *: indicates that the values were measured in a previous experiment.

Foil	Length (mm)	Width (mm)	Thickness (mm)	Mass (g)	Areal density (mg/cm^2)
SS1					100.199±0.091*
Ni01	25.228±0.140	25.293±0.059	0.0285±0.0010	0.1453±0.0000	22.772±0.138
Ir01	24.943±0.017	24.968±0.017	0.0295±0.0013	0.3436±0.0000	55.174±0.053
Cu01	25.553±0.045	24.883±0.030	0.0341±0.0030	0.1420±0.0000	22.338±0.048
Fe01	24.400±0.008	26.068±0.142	0.0278±0.0010	0.1274±0.0000	20.030±0.110
Ni02	25.288±0.017	25.428±0.102	0.0295±0.0010	0.1487±0.0000	23.118±0.096
Ir02	24.923±0.039	25.005±0.100	0.0278±0.0015	0.3465±0.0001	55.601±0.238
Cu02	25.443±0.025	25.550±0.018	0.0348±0.0020	0.1451±0.0000	22.325±0.028
Fe02	25.525±0.039	23.800±0.018	0.0274±0.0040	0.1216±0.0000	20.017±0.034
Ni03	25.295±0.025	25.210±0.070	0.0270±0.0010	0.1425±0.0000	22.338±0.066
Ir03	24.885±0.053	24.983±0.010	0.0243±0.0017	0.3459±0.0000	55.643±0.121
Cu03	25.560±0.041	25.508±0.025	0.0343±0.0030	0.1455±0.0000	22.313±0.043
Fe03	26.113±0.097	25.235±0.107	0.0310±0.0040	0.1315±0.0000	19.948±0.114
Ni04	25.303±0.070	24.888±0.040	0.0273±0.0010	0.1304±0.0000	20.704±0.068
Ir04	24.960±0.039	24.833±0.029	0.0261±0.0029	0.3471±0.0000	56.000±0.109
Cu04	25.153±0.025	25.603±0.017	0.0333±0.0010	0.1435±0.0000	22.284±0.027
Ni05	25.325±0.026	25.495±0.044	0.0263±0.0010	0.1406±0.0000	21.768±0.045
Ir05	24.948±0.025	24.958±0.026	0.0256±0.0024	0.3435±0.0001	55.161±0.081
Cu05	25.213±0.029	25.573±0.013	0.0334±0.0030	0.1447±0.0000	22.443±0.028
Ni06	25.530±0.119	25.195±0.065	0.0285±0.0020	0.1471±0.0000	22.861±0.123
Ir06	24.760±0.029	24.960±0.026	0.0240±0.0012	0.3444±0.0000	55.731±0.088
Cu06	25.343±0.013	25.513±0.010	0.0340±0.0020	0.1448±0.0000	22.396±0.012
Ni07	25.338±0.067	25.278±0.054	0.0268±0.0020	0.1479±0.0000	23.092±0.078
Ir07	24.955±0.013	25.008±0.035	0.0278±0.0022	0.3538±0.0001	56.685±0.085
Cu07	25.625±0.013	25.248±0.010	0.0326±0.0020	0.1444±0.0000	22.320±0.014
Ni08	25.205±0.135	24.950±0.033	0.0256±0.0030	0.1409±0.0000	22.409±0.124
Ir08	24.723±0.055	24.985±0.006	0.0281±0.0022	0.3585±0.0001	58.030±0.130
Cu08	25.370±0.032	24.885±0.017	0.0333±0.0030	0.1414±0.0000	22.401±0.033
Ni09	25.220±0.082	25.378±0.019	0.0257±0.0040	0.1392±0.0000	21.741±0.073
Ir09	24.670±0.008	24.993±0.017	0.0273±0.0010	0.3494±0.0000	56.669±0.043
Cu09	25.390±0.037	26.455±0.026	0.0331±0.0020	0.1506±0.0000	22.425±0.041
Ni10	25.285±0.024	24.405±0.010	0.0271±0.0030	0.1425±0.0000	23.093±0.024
Ir10	24.973±0.013	24.980±0.022	0.0270±0.0016	0.3435±0.0000	55.065±0.055
Cu10	25.470±0.032	25.338±0.043	0.0355±0.00010	0.1440±0.0000	22.314±0.047
SS2					100.865±0.097*
P-degrader					1900.0*
Ni neutron monitor					22.682±0.092

of a bias voltage, both the electron in the conduction band and the hole in the valence band travel to the detector electrodes and are collected as voltage

pulses [27, p. 215-216]. The major advantage with semiconductor detectors is that the average energy to create an electron-hole pair is very low, which results in a superior energy resolution in comparison to other detectors such as gas and scintillation detectors. At low temperatures (77 K), the average energy is 2.96 eV to create an electron-hole pair [27, p. 228]. High energy resolution is important for clearly distinguishing multiple peaks which are close in energy. For 1000 keV, the resolution of a typical HPGe detector is 0.1% (1 keV) which means that it is possible to separate two gamma-ray peaks within several keV [27, p. 117].

The detectors are doped to create an imbalance in the number of holes and electrons in the conduction band in a pure crystal ([27], p. 220), either by creating an excess of holes by adding an acceptor of electrons (p-type) or by adding a donor of electrons so there is an excess of electrons (n-type). In reality, both dopants are present (arranged in a p-n junction), but the dopant with the highest occurrence has the highest probability of interacting with radiation. The n-type material will have more electrons which will move toward the p-type material, and visa versa. Therefore, an imbalance arises due to the p-type having an excess of electrons, and the n-type having an excess of holes near the junction. The region where there is an imbalance is called the depletion zone, and a potential across the junction arises. When electrons and holes are created in the depletion by an interacting gamma-ray, they will be swept back due to the lack of charge carriers in the depletion zone. This will create a voltage pulse (with amplitude proportional to the incident gamma-ray's energy) which is assigned to a channel number as a "count". The depletion zone is quite narrow, but when a bias voltage is applied between the inner and outer radii of the detector cylinder, the depletion zone width increases. With this diffusion of electrons and holes process, the surface layer becomes heavily doped. The consequence is a thick dead layer which is insensitive to radiation interaction in the detector volume [27, p. 233]. Figure 3.3 shows a schematic of an n-type coaxical cylinder detector, where the electrons resulting from an incident ionizing particle will diffuse towards the inner hole.

The duration of the voltage pulse signal takes to construct is important, because other events that occurs meanwhile cannot be registered. This leads to a dead time, which is a time where nothing is recorded [27, p. 120]. The time that a detector registers an event is called the live time, which is the real time minus the dead time. Ideally, a system that does not add dead time to the existing (non-paralyzable) is preferred to reduce the amount of time where the detector is not detecting.

3.4.1 Obtaining a spectrum

The electrical signal (voltage pulse) registered in a detector has an amplitude which is proportional to the amount of gamma-ray energy which was registered

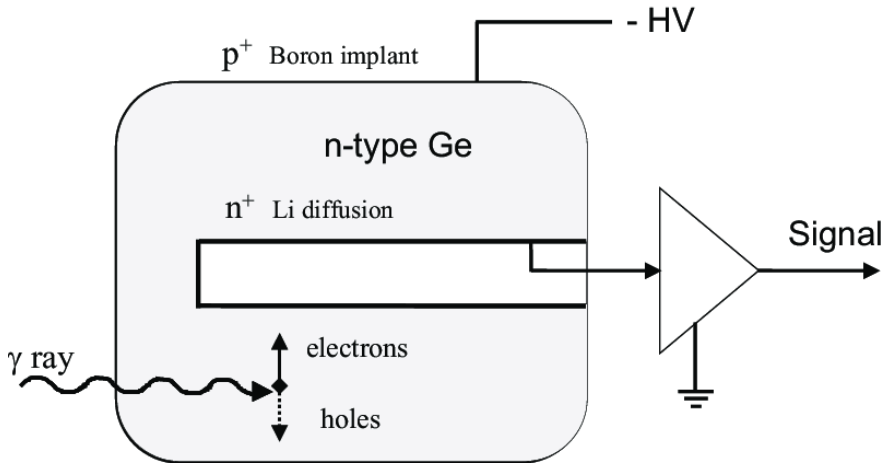

Figure 3.3: The figure shows an n-type germanium detector. Since the material is n-type, a potential where a p-n junction is created around the boron implant (outer surface). The figure is from [53].

in the detector [54, p. 61]. The electrical signal is assigned a channel number, which is proportional to the pulse amplitude. To obtain a spectrum, the number of registered events in each channel is counted, giving rise to the well-known peaks of the samples' decay. In an ideal detector, the peaks would appear as step functions, as the gamma-ray energies are discrete. However in practice, the counts in the channel close to the channel representing the true photopeak appears in a histogram which follows a Gaussian shape [54, p. 186]. This is due to incomplete charge collection, –ie., electrons or holes not collected, which moves counts from the center of the distribution to lower channels, creating a low energy tail of the peak [54, p. 135].

The observed gamma-peaks in the spectra obtained in this work are results of decay processes where the observed gamma-rays are from the decay of the excited daughter nucleus, or gamma-rays from decay of isomeric states. If multiple nuclei feed into the same daughter nucleus via different decay pathways, it is possible to populate the same energy levels giving rise to identical gamma-rays from different decay modes. In these cases, it may be possible to separate the different feeding components through multiple spectra taken over the span of all pathways' lifetime.

In a detector, the main interactions of gamma-rays and X-rays are via the photoelectric effect, Compton scattering and pair production [27, p. 53]. As described in section 2.2, photons are attenuated exponentially as a function of depth of medium and the absorption coefficient of the medium (Equation 2.3). The energy is transferred to atomic electrons in the detector. Therefore, since the gamma-radiation is highly penetrating, and some gamma-rays will also escape

the detector volume, larger detector volumes will increase chances of all energy being deposited in the detector [54, p. 32]. The attenuation coefficient is the sum of all the possible interactions (including Rayleigh and Klein-Nishina scattering).

Photoelectric effect occurs when the photon-energy is completely absorbed by an atomic electron, and dominates at low photon energies. This effect is desired in gamma-ray spectroscopy, as the total energy of the gamma-ray will be registered in one photopeak. The cross section of photoelectric effect is proportional to the $Z^{4 \text{ or } 5}$, and inversely proportional to the gamma-ray energy [27, p. 55]. Therefore, a high Z-material is desired to increase the cross section for the photoelectric effect.

In Compton scattering, the photon transfers a portion of its energy to an electron assumed at rest, and is scattered with an angle $\theta \in (0°, 180°)$. Depending on the angle, the energy of the deflected photon will vary, and give a spectrum of different energies, where higher scattering angle transfers more energy to the recoil electron. Since this process may repeat multiple times, if the final photon escapes the detector, the count will not appear in the photopeak, but instead contribute to a Compton continuum. The cross section of Compton scattering scales with electron density, which is fairly constant for all materials [27, p. 55].

In pair production, the photon is transformed into an electron-positron pair in a nuclear or electric field. Because of this, the energetic threshold is the double electron rest mass (1.022 MeV). The electron will be registered as an event, and the positron will quickly annihilate with an atomic electron, and two gamma-rays of 511 keV are created. If both annihilation photons fully deposit their energy, the peak will appear at the initial gamma-ray energy. Otherwise, this results in a single escape peak at $E_\gamma - 511$ keV if one photon escapes, or, they both escape, a double escape peak at $E_\gamma - 1022$ keV. The cross section for pair production increases with Z^2 [27, p. 57-58].

In addition, the decay gamma-rays may interact with the detector shielding, which is commonly made from a dense material like lead. The interaction leads to emission of characteristic X-rays from the absorbing medium. Also, since the shielding material is dense, most gamma-rays from Compton scattering are back-scattered, and if scattered by more than 120° appears as a broad peak within 200-300 keV. An annihilation peak at 511 keV is often present. The annihilation peak is either a result of annihilation of the positron from a β^+-emitter, or pair production in the shielding, where only one gamma-ray will be detected (since they are emitted in opposite directions) [54, p. 34-35]. Pileup is an effect which appears due to random summing which is due to possibility of two gamma-rays

being detected simultaneously [54, p. 33]. Figure 3.4 shows an example of a gamma-ray spectrum for Iridium foil number 5 (Ir05) ($E_d \approx 21$ MeV) approximately 35 hours after end of beam. The background at low energies is higher due to the multiple Compton continuum which are added together. In addition, the pileup effect can be seen on the high-end side of the spectrum.

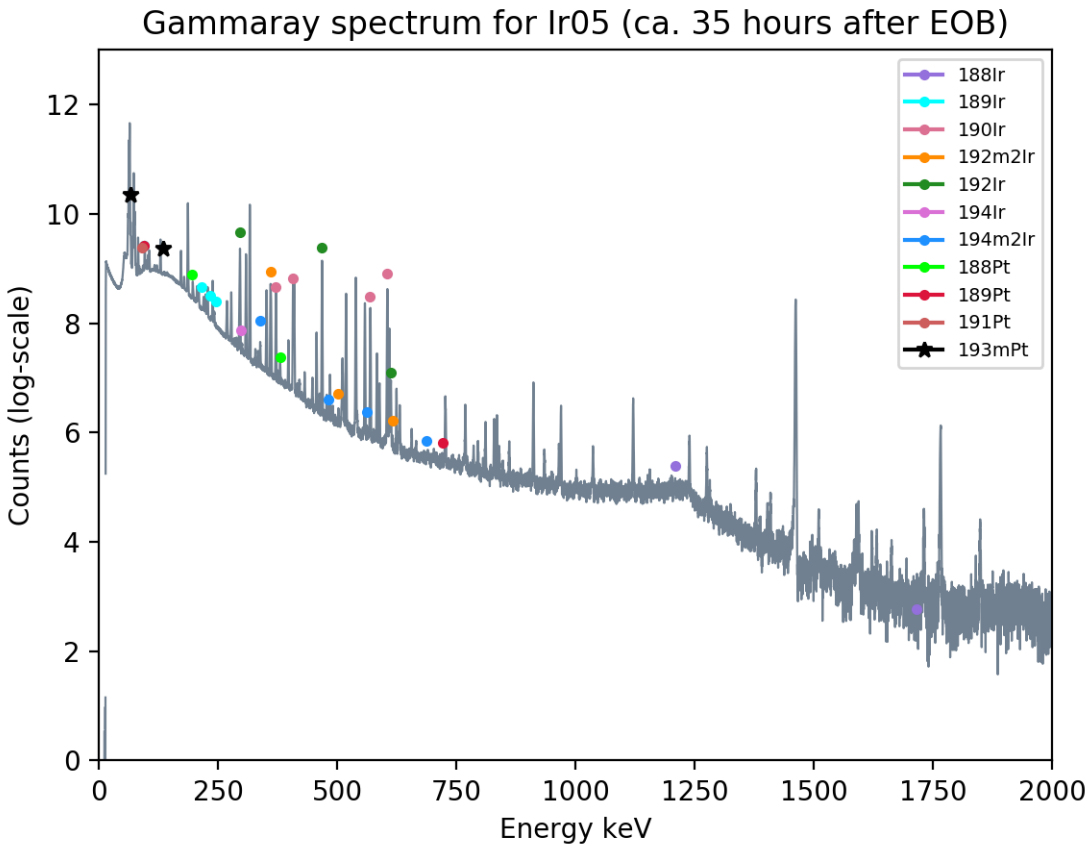

Figure 3.4: Gamma-ray spectrum for Ir05 (corresponding to deuteron energy of approximately 21 MeV) taken approximately 35 hours after end of beam. A selection of observed reaction products are highlighted, though the label does not necessarily represent what is present, but where the peak would have been. The X-ray region can be seen in the low energy side of the spectrum. The Compton region is larger at low energies. Pile-up effect can be seen at high energies.

The statistics of radioactive decay follows Poisson statistics, where the probability of observing N events is a discrete value:

$$P(N) = \frac{\mu^N e^{-\mu}}{N!} \tag{3.8}$$

where μ is the expected decay rate, which is equal to the variance ($\mu = \sigma^2$). This distribution models decay well when the decay rate is small and the number of events are large [27, p. 85]. This distribution is not symmetric, but as the decay rate increases, the peak approximates a Gaussian shape. The statistical uncertainty in a photopeak arises from Poisson statistics, and is large for small number of counts in the peak:

$$\sigma = \sqrt{N_i} \tag{3.9}$$

Therefore, to reduce the statistical uncertainty, a large number of counts are needed. Conventionally, a relative uncertainty of less than 1% is preferred, which corresponds to 10,000 counts in the peak.

In order to record the spectra from the detector, Maestro (Multichannel Analyzer Emulation Software) was used. In this work, the gamma-ray spectra were analyzed in FitzPeaks [55]. The algorithm is briefly explained in Appendix B, along with an example of a Peak Fit Report File obtained from a fitted spectrum from nickel foil number 10 (Ni10).

3.4.2 Determination of activity from fitted peaks

In general, the activity as a function of time takes the exponential form:

$$A(t) = A_0 e^{-\lambda t} \tag{3.10}$$

where A_0 is the activity at a reference time, and λ is the decay constant of a nucleus. If a spectrum is counted at a delay time Δt_d after end of beam with a counting time Δt_c the total number of decayed products are:

$$N_D = \int_{\Delta t_d}^{\Delta t_d + \Delta t_c} A(t) dt \tag{3.11}$$

Using Equation 3.10 for $A(t)$, the solution to the above equation is:

$$N_D = \frac{A_0}{\lambda} e^{-\lambda \Delta t_d} (1 - e^{-\lambda \Delta t_c}) \tag{3.12}$$

which also is equal to:

$$N_D = \frac{A(t)}{\lambda}(1 - e^{-\lambda \Delta t_c}) \tag{3.13}$$

From the spectrum, only the number of observed gamma-rays, N_C, are known. The number of counts is dependent on the efficiency, ϵ, of the detector, the intensity, I_γ, of the gamma-rays and the true number of decayed products, N_D:

$$N_C = N_D \epsilon I_\gamma \tag{3.14}$$

Thus, an expression for $A(t)$ after a delay time t can be obtained:

$$A(\Delta t_c) = \frac{N_C \lambda}{\epsilon I_\gamma (1 - e^{-\lambda \Delta t_c})} \tag{3.15}$$

Which is also equal to:

$$A_0 = \frac{N_C \lambda}{\epsilon I_\gamma (1 - e^{-\lambda \Delta t_c}) e^{-\lambda \Delta t_d}} \tag{3.16}$$

3.4.3 Energy and peak shape calibration

Since the channel number is not proportional to the gamma-ray energy, the detectors needed to be calibrated. The gamma-ray calibration point sources ^{137}Cs ($t_{1/2} = 30.08 \pm 0.09$ years), ^{133}Ba ($t_{1/2} = 10.551 \pm 0.011$ years) and ^{152}Eu ($t_{1/2} = 13.517 \pm 0.009$ years) [56–58] which were used can be seen in Figure 3.5. These are standard calibration sources for HPGe detectors, with precisely known gamma-energies and intensities. The gamma-lines which were used in the calibration are listed in Table 3.2. The detectors were calibrated at each of the fixed distance positions used during the counting of the experimental foils. On most HPGe detectors, including those used in this work, the gamma-ray energy is linearly proportional to channel number:

$$E = a + b \cdot c \tag{3.17}$$

where a is the slope of the line, b is the intercept and c is the channel number at that energy [54, p. 145]. The peak shape and energy calibration was done directly in FitzPeaks, by fitting the calibration spectra for each detector. Energy and peak shape source files for the gamma-lines listed in Table 3.2 were regressing to supplied energy and the built in functions calibrated each detector.

In addition to calibration spectra, long counts of the background for each detector was taken prior to irradiation, which was later used in the analysis, to verify if gamma-lines were background contaminated.

Figure 3.5: The calibration point sources that were used in the efficiency calibration of the detector. (^{22}Na was not used as part of the efficiency calibration due to its presence in the counting room background).

3.4.4 Efficiency calibration

The efficiency of the detector is dependent on the shape and density of the detector [54, p. 144], and is a very important parameter in the calculation of the end of beam activities from Equation 3.16. The calibration was done using the same gammas which are listed in Table 3.2. The reference date for the sources is January 1st 2009, and the ^{137}Cs measured 38.55 kBq, ^{133}Ba measured 39.89 kBq and ^{152}Eu measured 39.29 kBq, which can also be seen in Figure 3.5. Solving Equation 3.16 for efficiency, ϵ, the analytical efficiency as a function of gamma-ray energy and intensity is:

$$\epsilon(E_\gamma) = \frac{N_C \lambda}{A_0 I_\gamma (1 - e^{-\lambda \Delta t_c}) e^{-\lambda \Delta t_d}} \tag{3.18}$$

where λ is the decay constant, N_C is the number of counts in the fitted peaks, and Δt_d is the delay time since the reference date. The analytical efficiency gives the efficiency at energy E_γ, but a continuous function which gives the efficiency at any gamma-energy is desired for interpolation and extrapolation. The work of Gallagher *et al.* which was developed for efficiency calibration for Si(Li) X-raydetectors [59, 60] was used, which takes the probability of penetration through

Table 3.2: The calibration point sources along with gamma lines used in the calibration of the detectors. * indicates that the energy was averaged over two peaks with less than 1 keV in difference, and the intensities were summed. [56–58]

^{137}Cs		^{133}Ba		^{152}Eu	
E_γ (keV)	I_γ (%)	E_γ (keV)	I_γ (%)	E_γ (keV)	I_γ (%)
32.005*	5.63*	53.1622	2.14	121.7817	28.53
36.3405*	1.02*	80.9979	32.9	244.6979	7.55
661.657	85.10	160.6120	0.638	295.9387	0.440
		223.2368	0.453	344.2785	26.5
		276.3989	7.16	367.7891	0.859
		302.8508	18.34	411.1165	2.237
		356.0129	62.05	444.4853*	3.125*
		383.8485	8.94	503.467	0.1524
				586.2648	0.455
				678.623	0.473
				688.670	0.856
				719.353*	0.345*
				778.9045	12.93
				810.451	0.317
				867.380	4.23
				963.712*	14.65*
				1112.076	13.67
				1212.948	1.415
				1299.142	1.633
				1408.013	20.87

the dead layer of the detector and the probability of interaction in the detector volume into account:

$$\epsilon(E_\gamma) = B_0 \cdot \underbrace{\left(e^{-B_1 E_\gamma^{B_2}}\right)}_{\text{dead layer}} \underbrace{\left(1 - e^{-B_3 E_\gamma^{B_4}}\right)}_{\text{interacting with volume}} \tag{3.19}$$

where B_i are optimization parameters. The Scipy Optimize Curvefit function [61] takes in the analytically calculated efficiencies and uncertainties calculated from Equation 3.18, fits the values to the function represented in Equation 3.19, and returns the optimal parameters B_i and the calculated covariance matrix, through χ^2 minimization. This fit is uncertainty weighted, which means that data with low uncertainty will be weighted higher. Since the lowest energy calibration line used in 32.005 keV and the highest one is 1408.013 keV, the fitted efficiencies outisde of this region are extrapolated, and thus have large uncertainties in comparison to the region interpolating between measurement points. According to Matthew *et al.* (2020), "the use of canonical logarithmic polynomial gamma-ray efficiency calibration forms result in significant biases in efficiency for both the interpolated and extrapolated energies" [60], which was the motivation behind using this model for efficiency. Since the optimized parameters are highly correlated, the uncertainty in efficiency was calculated according to Equation A.5 in Appendix A. Figure 3.6 shows two examples of the fitted efficiency curves from this work. The top figure shows the efficiency curve for detector 1 at a counting distance 30 cm from the detector surface, and the bottom figure shows the efficiency curve for detector 7 at a counting distance 15 cm from the detector surface. Both curves follow the points around the peak very well. For the first efficiency curve (top), the effect of counting statistics can be seen, as the uncertainties which are remarkably larger have gamma-ray intensities of less than 1%. This could have been avoided by excluding these low-intensity gamma-lines, but since the fit is uncertainty-weighted, the number of lines remained for a larger amount of data. It is also clear that the absolute efficiency for detector 7 is larger by a factor of approximately 2.7 around the peak, which is mainly due to the counting distance from the detector. On both figures, the uncertainty is higher around the peak, and for detector 7 (bottom), the uncertainty is clearly increasing with energy. Figure 3.7 shows the relative uncertainty for each detector at each distance as a function of gamma-ray energy. For all detectors, the main contributions to uncertainty is where the functional fit is extrapolated and around the efficiency peak where the derivative is large. In addition, the relative uncertainty for gamma-ray energies above 1000 keV increases caused by less datapoints. Figure 3.7 shows the relative uncertainties of detectors 1-6 (top) and detector 7 (bottom) at various distances. It is clear that the uncertainties are high where the functional fit is extrapolated over areas where there is no existing

data. This was below 32.005 keV and above 1408.013 keV (Table 3.2). In addition, the peak is sensitive to changes in energy and is also large. The counting statistics affects the uncertainty, where a longer counting distance demands a longer counting time to obtain the same number of counts (since the solid angle decreases).

3.5 The irradiation

The irradiation of the target stack took place on February 26th 2019, and the activated foils were counted on the high purity germanium detectors for a total of 4 weeks after end of beam. In addition to this experiment, two other experiments took place, an irradiation of strontium with deuterons and a deuteron break-up experiment. The target stack was subject to a 33 MeV incident deuteron beam, which can be seen in Figure 3.8.

Tuning of the beam

Before irradiation, the deuteron beam was tuned to be approximately 1 cm in diameter. In addition, the experiments taking place simultaneously demanded a precise position of the beam spot since the target size was on the same order of the beamspot. The beam spot was first visualized using an approximately 2.5 cm thick borosilicate glass, painted with a mixture of phosphor powder and vacuum grease (so that the paint does not evaporate as the tube was pumped down to vacuum). When ionizing radiation strikes the phosphor, the phosphor is excited and emits light in the de-excitation, called phosphorescence. The glass was placed on the end of the beam tube. With a camera placed in cave 0, from the control room, the beam spot could be visualized, and could be steered to be centered and focused to approximately 1 cm in diameter. The beamspot can be visualized in Figure 3.9 (left), and the borosilicate glass placed on the end of the beam tube can be seen in Figure 3.9 (right). The beam is ideally shaped to a "pencil beam", but because the beam is focused from the cyclotron vault, there will always be a degree of divergence/convergence to the beam. Gafchromic EBT3 films were placed in the front and the back of the target holder to visually check that the spatial beam profile was not significantly diverging or converging over the length of the target holder. The films were exposed for a brief second, and the blue spot on the developed film was evaluated. Iterations of films were exposed until optical tuning of the beam was acceptably centered, homogeneous, and focused into a pencil beam. The films after direct exposure can be seen in Figure 3.10 in the target holder.

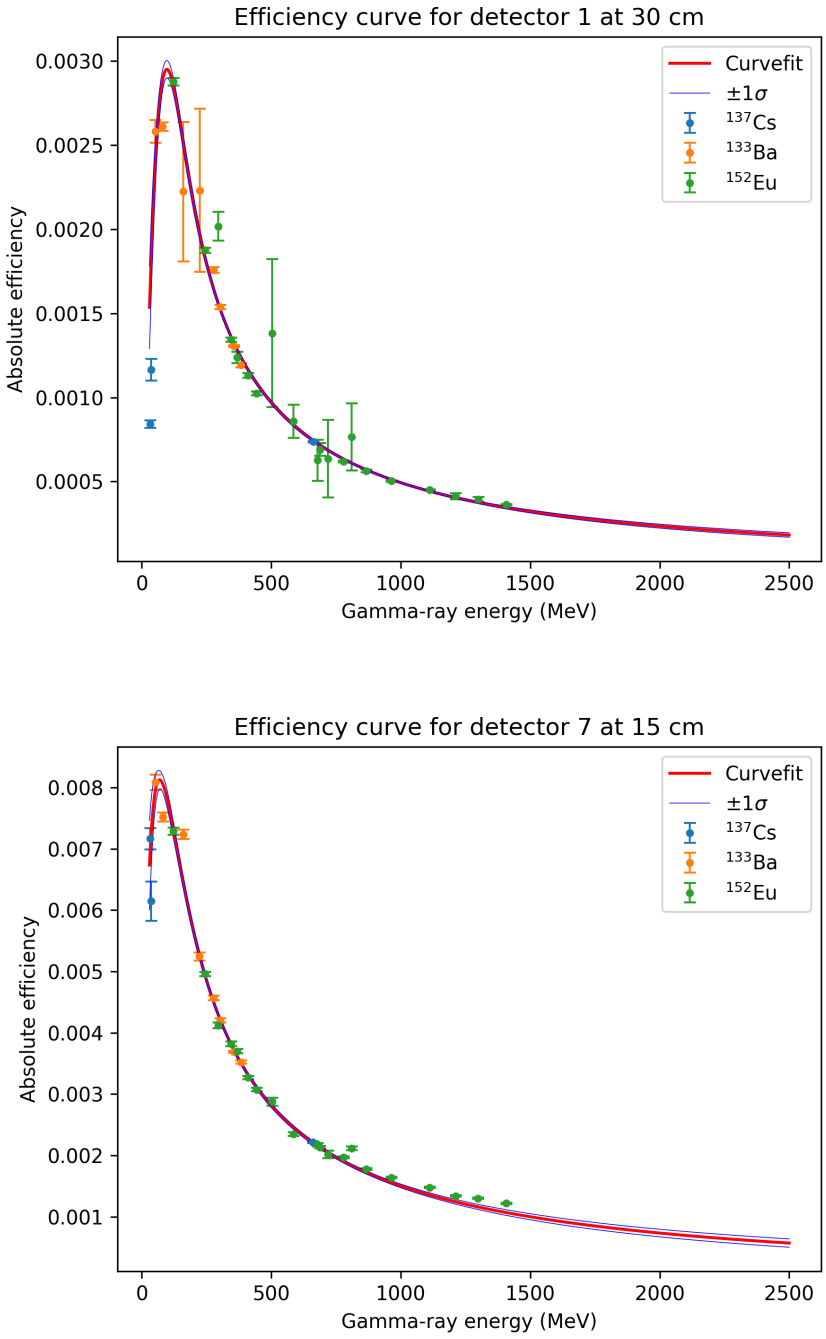

Figure 3.6: Two examples of efficiency curves. The blue lines represent the uncertainty bands which were calculated from Equation A.5. **Top:** The efficiency curve of detector 1 at counting position 30 cm. **Bottom:** The efficiency curve of detector 7 at counting position 15 cm.

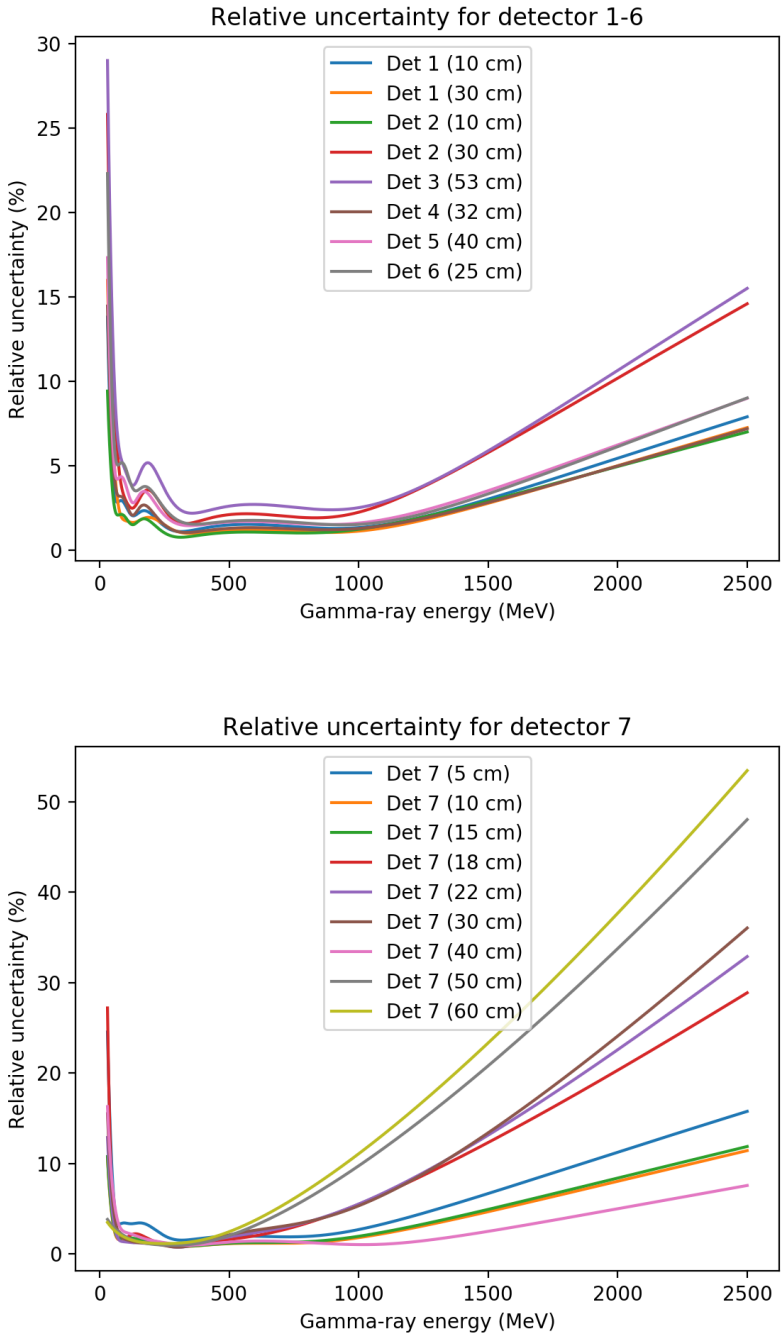

Figure 3.7: The relative uncertainty in efficiency for each detector. **Top:** Relative uncertainty for detectors 1-6. **Bottom:** Relative uncertainty for detector 7

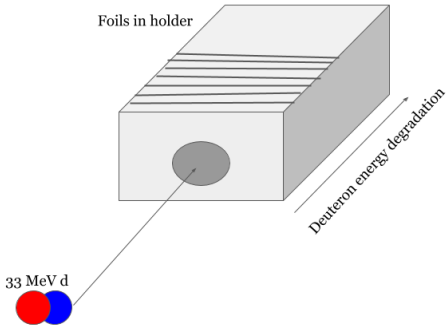

Figure 3.8: The figure shows a sketch of the experiment where a stack of targets are placed in a target holder, and irradiated with 33 MeV deuterons. As the beam energy is degraded through the stack, it is possible to measure multiple cross sections at different energies.

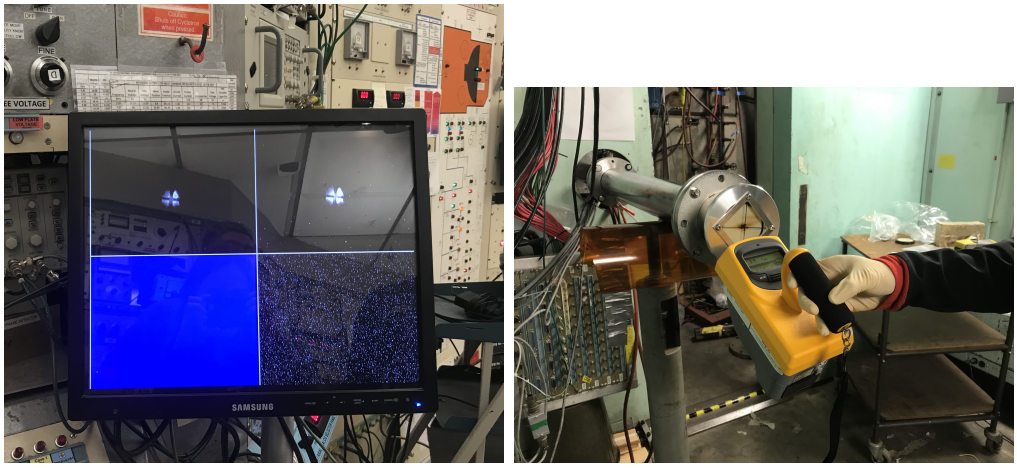

Figure 3.9: The figure shows: **Right:** the beamspot which could be visualized from the control room, and **Left:** the borosilicate glass phosphor target placed on the end of the beam tube. The dose present after the beam was on was always measured before entering or handling beamline components.

Figure 3.11 shows the final directly exposed Gafchromic EBT3 film superimposed to one Ir foil. The activation on the film confirms that the that the beam is centered on the foil.

The beam transmission efficiency was calculated by measuring the the current at the Faraday cup right after the cyclotron vault (BS-02) and right before cave 0 (FC-01), seen in the facility map in Figure 3.1. BS-02 was measured to be 420 nA and FC-01 was measured to be 285 nA. This gave a beam efficiency of

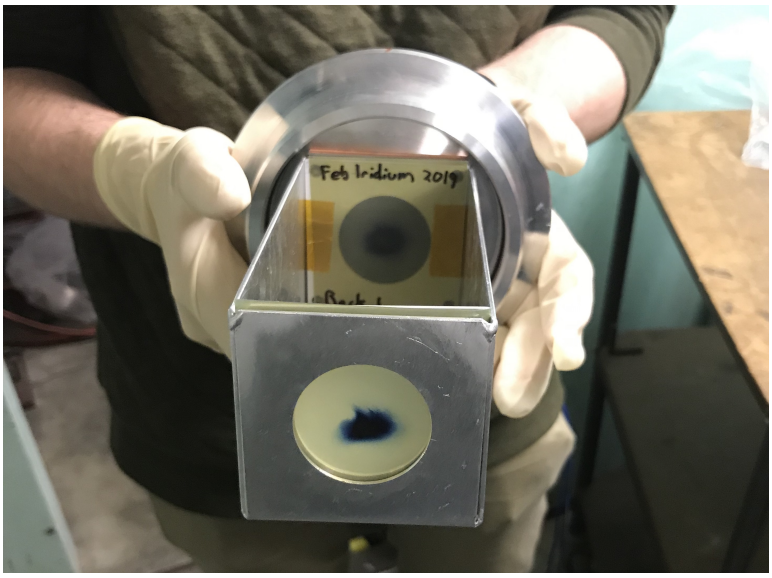

Figure 3.10: The gafchromic films were directly exposed for approximately one second at a beam current of 0.1 nA.

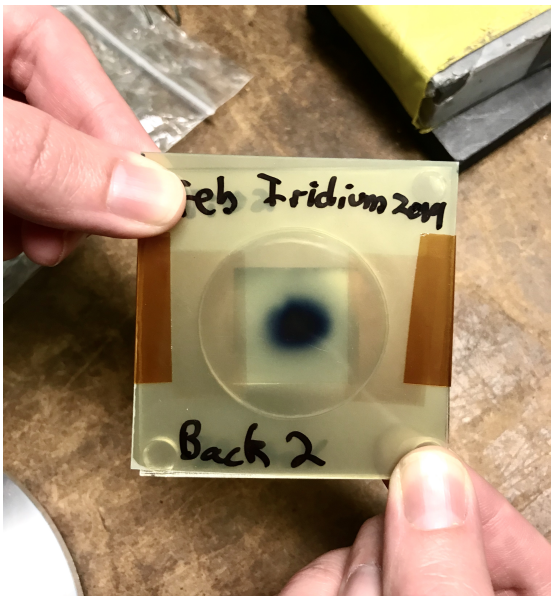

Figure 3.11: The exposed Gafchromic EBT3 film, superimposed over one of the Ir foils during the beam optics tuning before. This film confirms that the beam is centered and fully contained within foil geometry.

transmission 67%.

Irradiation of the target stack

For irradiation, the foils were placed in a target holder which was a 6061 aluminum alloy with a hollow center in the front for the beam line to pass through. A hollow spring was used to keep the foils stable during the irradiation. The target holder can be seen in Figure 3.12 (left). The irradiation lasted for one hour (3600 ± 3 s). When a target is irradiated, the activity of a product nucleus will increase until secular equilibrium is achieved (where the rate of production is equal to the rate of disintegration). Therefore, an irradiation of more than 2-3 half-lives does not further increase the activity of a nucleus. Exposing a thin target for a 100-150 nA beam for 1 hour, using the 88-Inch Cyclotron, has been shown to produce sufficient amount of activity for gamma-ray spectroscopy. The dose from the activated foils does not pose a safety concern, and avoids unnecessary detector dead time. Since the beamline used to mount the target stack was electrically isolated, a connected current integrator measured the incident beam current on the target stack, and verified that the beam current remained stable during the irradiation. Otherwise, the term $\Phi(1 - e^{-\lambda t_{\text{irr}}})$ in Equation 3.6 must be modified. The registered average beam currents registered over the length of the irradiation can be seen in Figure 3.13. After the end of the irradiation, the beam integrator read out $I\Delta t = 2314C$, with full-scale amperes being $2 \cdot 10^{-7}$ A. The average beam current hitting the front of the stack was thus:

$$\frac{2314 \cdot 2 \cdot 10^{-7}}{3600} = 128.5 \text{ nA} \tag{3.20}$$

Before the beam was turned on, the beam tube had to be pumped down to a vacuum, to avoid attenuating and scattering the beam. The target holder was placed in the end of the electrically isolated beam tube. Figure 3.12 shows how the target holder (left) was placed in the end of the beam line (right). About ten minutes after end of beam , cave 0 was opened, and the targets were sealed in plastic bags to prevent contamination. The iridium foils were counted starting approximately 15 minutes after end of beam on detector 7, and the other foils following up shortly after. All the foils were counted for approximately four weeks following end of beam on the various detectors, with short and frequent counts in the beginning to have good statistical data for the short-lived activities, and progressively longer counts as the shorter and medium-lived activities decayed out, to collect good statistics. The foils were counted multiple times to reduce the statistical uncertainty, and in addition make sure that the products with similar gamma-lines but different half-lives were observed independently if possible. Since the detectors were calibrated at various distances, the dead time of the foils right after end of beam could be reduced by increasing the distance from the detector, however, as high as 16-22% dead time was initially present, but reduced to about 5% within a cooling time of approximately 1 day after

end of beam double check, but on quick overview this seemed right. ^{193m}Pt has one single weak gamma-line at 135.5 keV (0.1145475 ± 0.03%). In addition, it is located at the shoulder of ^{192}Ir at 136.39 keV (0.199 ± 0.025 %) [4, 62]. The half-life of ^{192}Ir ($t_{1/2}$ = 73.829 ± 0.011 d) is long, and it was important to make sure that the two peaks were identified independently. Due to the relatively long half-life of ^{193m}Pt ($t_{1/2}$ = 4.33d ± 0.03), and the weak gamma-ray, its single gamma-line was observed within a few days after end of beam, when the counts were longer. In addition the short-lived monitor reactions ^{nat}Cu(d,x)^{62}Zn ($t_{1/2}$=9.193 h), ^{nat}Cu(d,x)^{63}Zn ($t_{1/2}$=38.47 m) and ^{nat}Ni(d,x)^{61}Cu ($t_{1/2}$=3.339 h)[63–65] were observed in each single foil, in addition to the other longer-lived monitor-radionuclides.

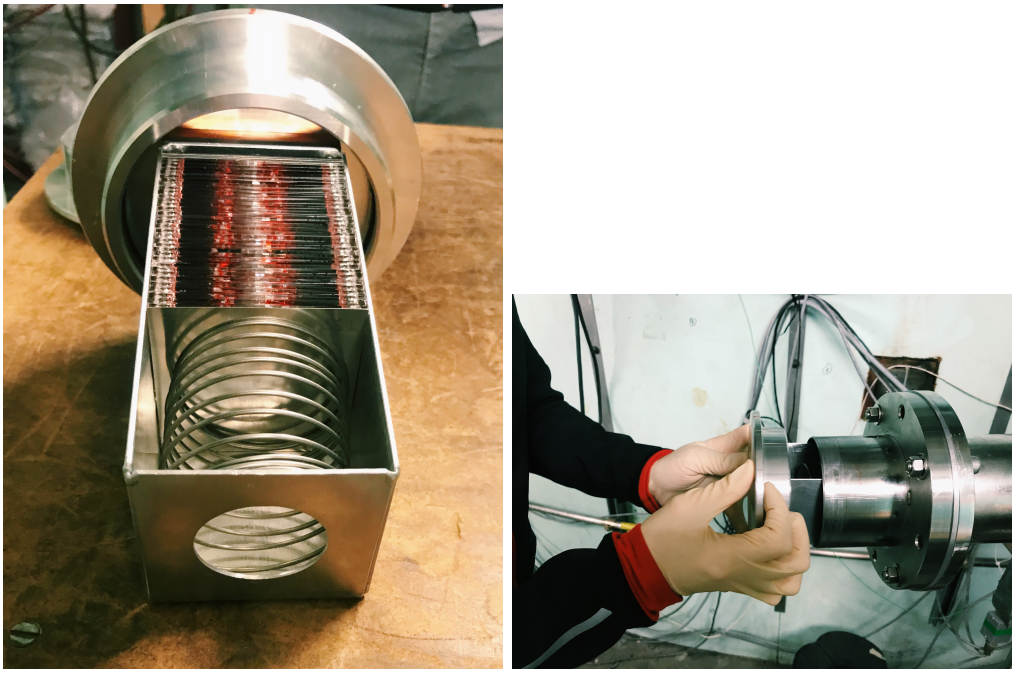

Figure 3.12: The figure shows the target stack was placed in the beamline. **Left:** The targets were placed in a 6061 aluminum alloy target holder with a hollow center for the beam to pass through. The hollow spring kept the targets in a fixed position throughout the irradiation. **Right:** The target holder was placed in the electrically isolated beamline.

Intensity profile of the beam

After irradiation, Gafchromic EBT3 film was attached to the activated stainless steel SS1 and SS2 foils, to obtain a quantitative spatial intensity profile of the beam in the front and the back of the stack. The radius of the activity

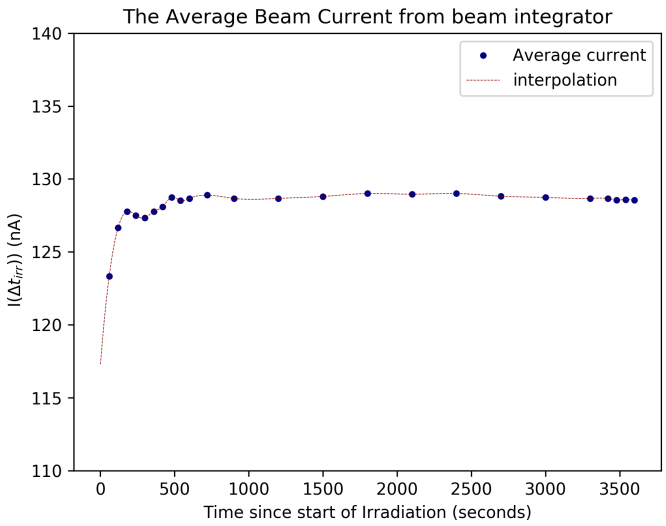

Figure 3.13: The average current registered from the beam integrator. This was used to check that the current remained stable during the irradiation.

from stainless steel on Gafchromic film was measured using the imaging process program ImageJ-1.52k, which is developed by the National Institutes of Health and the Laboratory for Optical and Computational Instrumentation [66]. The Gafchromic films were scanned alongside a ruler for scale comparison. The intensity over the developed film was obtained by inverting the scanned image, and drawing a line segment (where the number of pixels per cm was scaled using the ruler) along the beam spot that created a position dependent intensity array.

Since the spatial intensity profile of the beam was non-uniform (more intense in the center), the intensity profile can be fitted to a Gaussian, which is shown example-wise in Figure 3.14, which is the horizontal beam profile in the front and the back of the stack. In the assumption that the beam was underfilled, it was important to build confidence that the beamspot was smaller than the target foils. This was done by measuring the full width half maximum (FWHM) of the fitted Gaussian profile. The FWHM over SS1 was 1.2017 cm horizontally (σ^2 =0.2604 cm^2) and 1.1420 cm vertically (σ^2 =0.2352 cm^2). The FWHM over SS2 was 0.6706 cm horizontally (σ^2 =0.0811 cm^2) and 0.5783 cm vertically (σ^2 =0.0603 cm^2). The exposure curve of the developed film is approximately logarithmic scaled. This will reduce the exposure outer fringes of the beam spot, potentially underestimating the measured FWHMs. In comparison, a qualitative measurement by eye suggests a vertical width of 1.2 cm in SS1 and horizontal width 1.3 cm of SS1 and a vertical width of 0.3 cm and a horizontal width of 0.3 cm for SS2 (which lacks value because it was difficult to evaluate due to the weak activity).The beam spot does appear as slightly broader than 1

cm for both measurements. This is because the Gafchromic film is primarely developed by the isotropic emission of beta particles and other high LET-decay radiation from stainless steel foils, increasing the apparent width. The beam broadens throughout the stack because of scattering. Unfortunately, the full effect of scattering was not possible to see, as the beam seems to be stopped in SS2. This implies that a much larger fraction of the deuteron energy in this location was below threshold for activation.

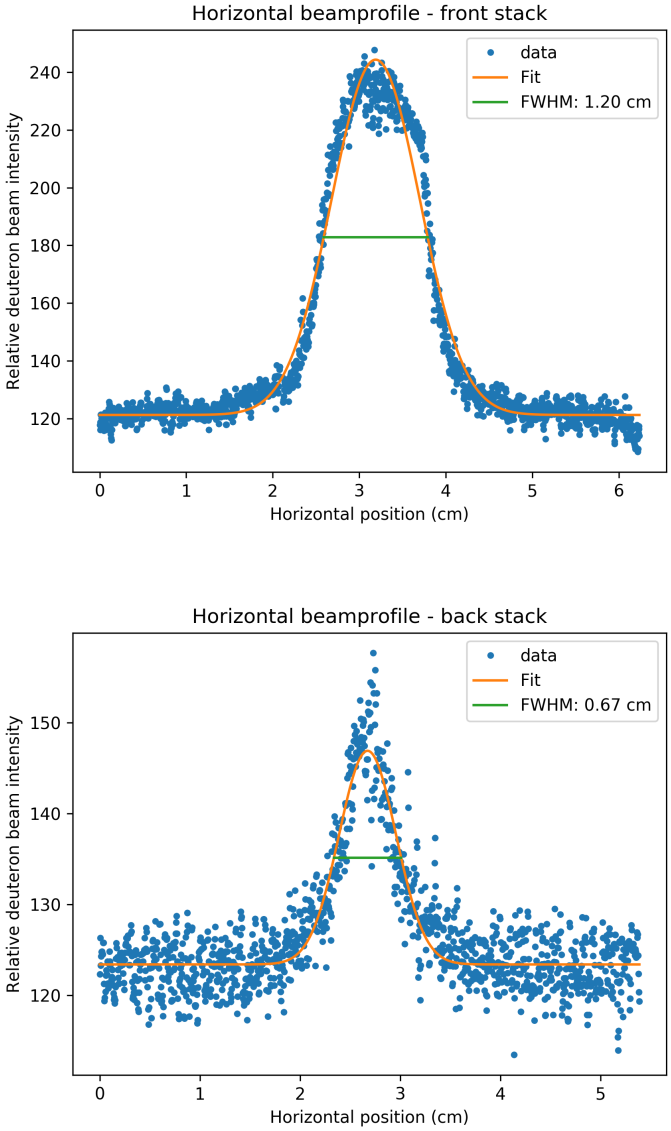

Figure 3.14: Figure shows the intensity profile of the deuteron beam in the front and in the back of the stack, measured using the scanned Gafchromic EBT3 film exposed to the stainless steel profile monitors. **Top:** SS1. **Bottom:** SS2.

Chapter 4

Analysis

This chapter will provide the analysis of the data recorded from the gamma-ray spectroscopy from the HPGes. The analysis of the gamma-ray spectra is described in section 4.1. The calculation of end-of-beam (EOB) activities are described in section 4.2. The monitor reactions are described in section 4.3. Section 4.4 include the calculations of the weighted average beam current throughout each compartment using the monitor reactions, and the energy assignments of the foils, where a variance minimization varying the beam current energy and target foil densities to find the correct energy assignment. Section 4.5 finally describes how the cross sections were calculated. The final cross section results are represented in the next chapter.

4.1 Analysis of the gamma-ray spectra

Using the energy and peak shape calibrations described in subsection 3.4.3, all peaks in the collected spectra were fitted using FitzPeaks [55], and a report file was obtained for each spectrum with the information regarding the fitted peaks, along with additional information such as target foil, detector, the time of the spectrum and delay time since end of beam. An example of one such peak fit report file is shown in Figure B.1. From the report file, the parameters which were used in the analysis was the peak energy for identification, the peak area (N_C) and uncertainty in peak area for activity calculations. Gammas per second (the countrate) was used as a critical tool to evaluate background contamination in a peak, by comparing the countrate of a peak to the background spectra.

Figure 4.1 shows selected energies regions gamma-ray spectra for foils Ir01-Ir10. ^{193m}Pt is observed in the X-ray region (top) and the gamma-region (bottom) taken sequentially, approximately one week after the end of beam. The net-number of counts decreases for each foil since the Compton background is reduced as less products are activated following deuteron beam energy degrada-

tion. The figure is informative, as it shows how the various foils are activated. From Figure 4.1 (top), the X-ray at 66.8 keV X-ray is strongly fed, in particular in iridium foils 4-10. In the bottom figure, it is clear that the 135.5 keV gamma-line from ^{193m}Pt is located on the shoulder of the gamma-line 136.39 keV from ^{192}Ir [4, 62].

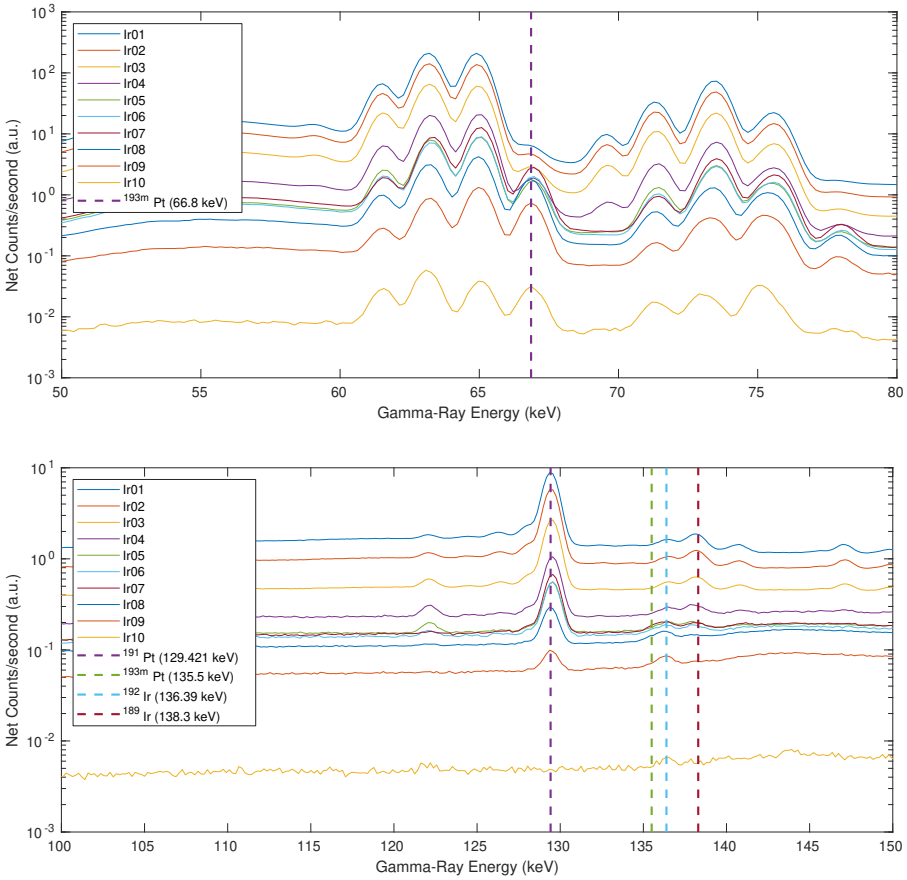

Figure 4.1: Selected regions of the gamma-ray spectra for foils Ir01-Ir10 taken approximately 1 week after the end of beam. **Top:** The X-ray region, highlighting the ^{193m}Pt 66.8 keV line. **Bottom:** The gamma-ray energy region from 100-150 keV, where the single gamma-line of ^{193m}Pt is located.

The report files for all the foils of the same target type (i.e., all Ir foils) was looped over to obtain a list of all of the observed gamma-ray energies. The report files were first sorted on the observed gamma-ray energies. If the absolute difference between gamma-ray energies was less than a tolerance for peak uniqueness (set to 0.75 keV), the energies were averaged. Figure 4.2 shows a selection of the gamma-ray energies as a function of the peak index (assigned from the sorted list of energies) ranging from 0-500 keV for unique iridium energies. Each observed

gamma-ray is represented by a red cross. The plot takes a "staircase" form as the observed gamma-ray energies form distinct horizontal "bands" for the multiple observations of each unique gamma-ray, averaged within a tolerance of 0.75 keV. For each unique gamma, the product nuclei were identified based on radiation searches from the LUND/LBNL Nuclear Data Search [67].

If a gamma-ray peak was contaminated by decay radiation from another product nucleus, the half-lives were compared. If they were significantly different, spectra taken very early or late after end of beam was used where the amount of product feeding in was zero. After a period of ten half-lives the product was assumed to have decayed out. If a radionuclide is correctly identified, the most intense gamma-lines in decreasing order must also be observed in the same spectrum, within detection limits. If the gamma-ray peaks identified were contaminated by background radiation or by other nuclei, other gamma-lines free of contamination were used if possible. Background subtraction was avoided if possible, and was only performed on two occasions, due to the presence of observed activation products in one counting room's natural background. The method for background subtraction is explained in subsection 4.1.1.

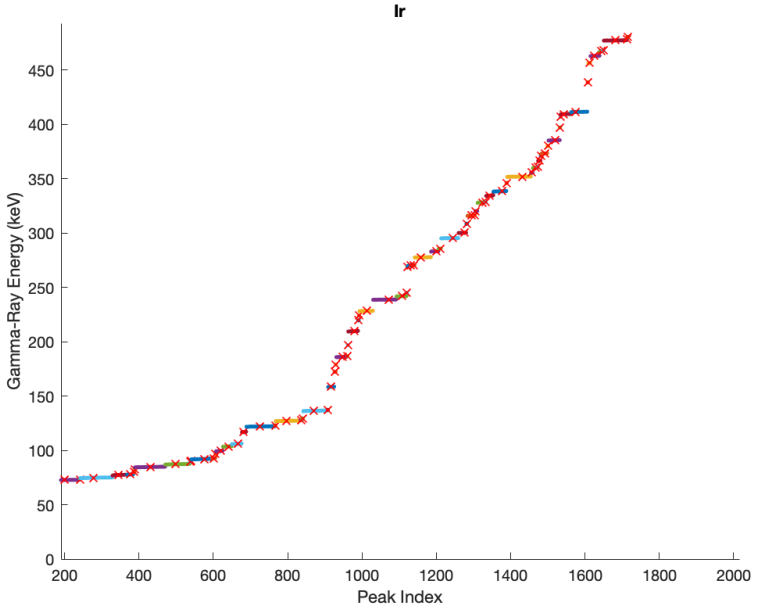

Figure 4.2: "Staircase" plot showing the multiple gamma-ray energies observed from all iridium foils, for a selected energy window between 0 and 500 keV. Each "staircase" represents the multiple observations of the same gamma-ray across multiple spectra. Within a tolerance of 0.75 keV, the average energy for each unique gamma-ray appears as a red "x". The average energies were used for for isotope identification.

Once the gamma-lines were identified, the accepted decay data, including half-life, intensity and uncertainty in intensity, was obtained from the NNDC database and the ENSDF datafiles (Nudat-2.8) [43]. The values are listed in Tables C.2, C.3, C.4 and C.5 of Appendix C for iridium, iron, nickel and copper, respectively, along with reaction routes and reaction Q-values (provided from the NNDC database [68]) for the exit channels with protons, neutrons and alpha-particles.

4.1.1 Background subtraction

In a few cases, background subtraction was necessary due to the presence of some activation products in the background. Background radiation was only problematic for cobalt activation products counted on the detectors located in cave 4C, due to the presence of long-lived nuclei of cobalt. The general rule of thumb was only to use background subtraction when all gamma-lines of the nucleus was contaminated with a count-rate of the same order, due to the increase in peak area uncertainty caused by this process.

For a single gamma-ray, the average count-rate is defined as the number of counts divided by the live time of the spectrum, in units of counts/second:

$$C = \frac{N_{\mathrm{C}}}{\Delta t_{\mathrm{live}}} \tag{4.1}$$

When the live time is much shorter than the half-life of the radionuclide in question, the number of true count rate is the difference between the observed countrate C_{obs} and the background countrate C_{bg}:

$$C_{\mathrm{true}} = C_{\mathrm{obs}} - C_{\mathrm{bg}} \tag{4.2}$$

From Equation 4.1, the number of true counts is the count-rate multiplied by the live time, which gives:

$$N_{\mathrm{true}} = N_{\mathrm{obs}} - (\Delta t_{\mathrm{live}} C_{\mathrm{bg}}) \tag{4.3}$$

4.2 Calculation of activities at end of beam

The activities at end of beam were calculated by extrapolating backwards in time using accepted half-lives and the activities at the spectrum time points after the end of beam. The activities measured in each spectrum as a function of time

since end of beam (Δt_{d}) were calculated using Equation 3.15 along with a self-attenuation correction:

$$A(\Delta t_{\mathrm{d}}) = \frac{N_{\mathrm{C}}\lambda}{\epsilon I_{\gamma}(1 - e^{-\lambda \Delta t_{\mathrm{d}}})e^{-\mu\rho\Delta r/2}} \tag{4.4}$$

where μ is the photon attenuation coefficient from the XCOM photon cross section database [69], and $\rho\Delta r$ is the areal density of the foil. The XCOM data provided a list of photon energies up to 20 MeV and the mass attenuation coefficient which has units cm^2/g. The attenuation coefficient data used spline interpolation to be evaluated at any gamma-ray energy. The impact from the attenuation is in particular evident up to about 200 keV, but after it is nearly negligible with values on the order of 10^{-2}–10^{-3}. The gamma-ray self-attenuation (in this work, on average less than 0.2 %) correction is based on the assumption that all activity that is made is located midway in the foil thicknesses. In reality however, the activity profile will follow the same shape as the excitation function over the foil, since activity and cross section are proportional. The excitation function is not known ahead of time, and the excitation function does not change significantly within one of these targets, since the foil thicknesses are so thin. So instead, this simplification is done, assuming that, on average, the attenuation is through half of the foil thickness.

The activities for a specific product as function of time since end of beam was calculated from Equation 4.4, using the nuclear data tabulated (listed in Tables C.2, C.3, C.4 and C.5 for iridium, iron, nickel and copper, respectively). Looping over the peak fit reports for each foil, the number of counts along with the uncertainty in number of counts were extracted from the report file. The efficiency and the photon attenuation was extracted as a function of the gamma-ray energy, along with the areal density of the foil where the gamma-line was observed. Each calculated activity and uncertainty in activity as a function of time since end-of-beam observed in a foil was fitted to a decay curve. The uncertainty in activity was calculated through the uncorrelated error propagation, according to Equation A.8 (using the square root to get the standard deviation).

In multiple cases, a measured activity in a foil was off by multiple factors of 10, which were either due to do false peak assignment or contamination in a particular channel. For cases where no explanation for a discrepant activity could be found, the gamma-line was completely excluded from the analysis.

The activity curves are based on Bateman equations [70]. The decay curve of a single radioactive nucleus takes an exponential form:

$$A(t_d) = A_0 e^{-\lambda t_d} \tag{4.5}$$

where t_d is the delay time (the time since end of beam), A_0 is the activity at end of beam. For multiple nuclei in a decay chain, the Bateman equation is used describing the activity in nucleus n of the decay chain:

$$A_n = \lambda_n \sum_{i=1}^{n} \Big[\Big(A_{i,0} \prod_{j=i}^{n-1} \lambda_j \Big) \cdot \Big(\sum_{j=i}^{n} \frac{e^{-\lambda_j t}}{\prod_{i \neq j}^{n} (\lambda_i - \lambda_j)} \Big) \Big] \tag{4.6}$$

where A_n is the activity of nuclei n in the decay chain, with the corresponding decay constant λ_n. The equation sums over all nuclei in the decay chain. In this work, decay chains of single and two-step (n=1,2) were sufficient. For two-step decay, Equation 4.6 simplifies to:

$$A_d(t) = \lambda_n \Big[A_{p,0} \lambda_1 \frac{(e^{-\lambda_1} + e^{-\lambda_d})}{\lambda_p - \lambda_d} + A_{d,0} e^{-\lambda_d t} \Big] \tag{4.7}$$

where p is the parent nucleus, and d is the daughter nucleus. The parent activity is calculated from single step decay.

The extrapolation was done using the Scipy Optimize Curvefit function [61], where the activities and the uncertainties in activities calculated from Equation 4.4 were fitted via χ^2-minimization to the decay-curve, with $A_{\mathrm{p},0}$ and/or $A_{\mathrm{d},0}$ serving as optimizing parameter(s). The function returns the optimal parameters along with the covariance matrix of the optimal parameters. For the cases where there was two-step feeding, but the parent nucleus did not emit observable gamma-rays, two-step decay with both the end of beam activities of the daughter and the parent served as optimizing parameters was used. For the two former cases, there was only one optimizing parameter, and the uncertainty was simply the standard deviation obtained from the square root of the covariance matrix. For the latter, the two optimizing parameters were correlated, and Equation A.5 had to be used to calculate the uncertainty. Figure 4.3 shows three examples of three different activity curves; one-step decay for $^{193\mathrm{m}}$Pt ($t_{1/2}$=4.33 days), two-step decay for ^{58}Co ($t_{1/2}$=70.86 days) with feeding from the isomer $^{58\mathrm{m}}$Co ($t_{1/2}$=9.10 hours), which had to be fitted using $A_{\mathrm{p},0}$ and $A_{\mathrm{d},0}$, and two-step decay of ^{56}Co ($t_{1/2}$=77.236 d) with feeding from ^{56}Ni ($t_{1/2}$=6.075 d) using the activity of ^{56}Ni and the optimized A_0 of ^{56}Co [4, 71, 72]. The uncertainty bands are large for ^{58}Co, as the two-step decay with no observed parent propagates into a higher uncertainty in the $A_{\mathrm{p},0}$ parameter.

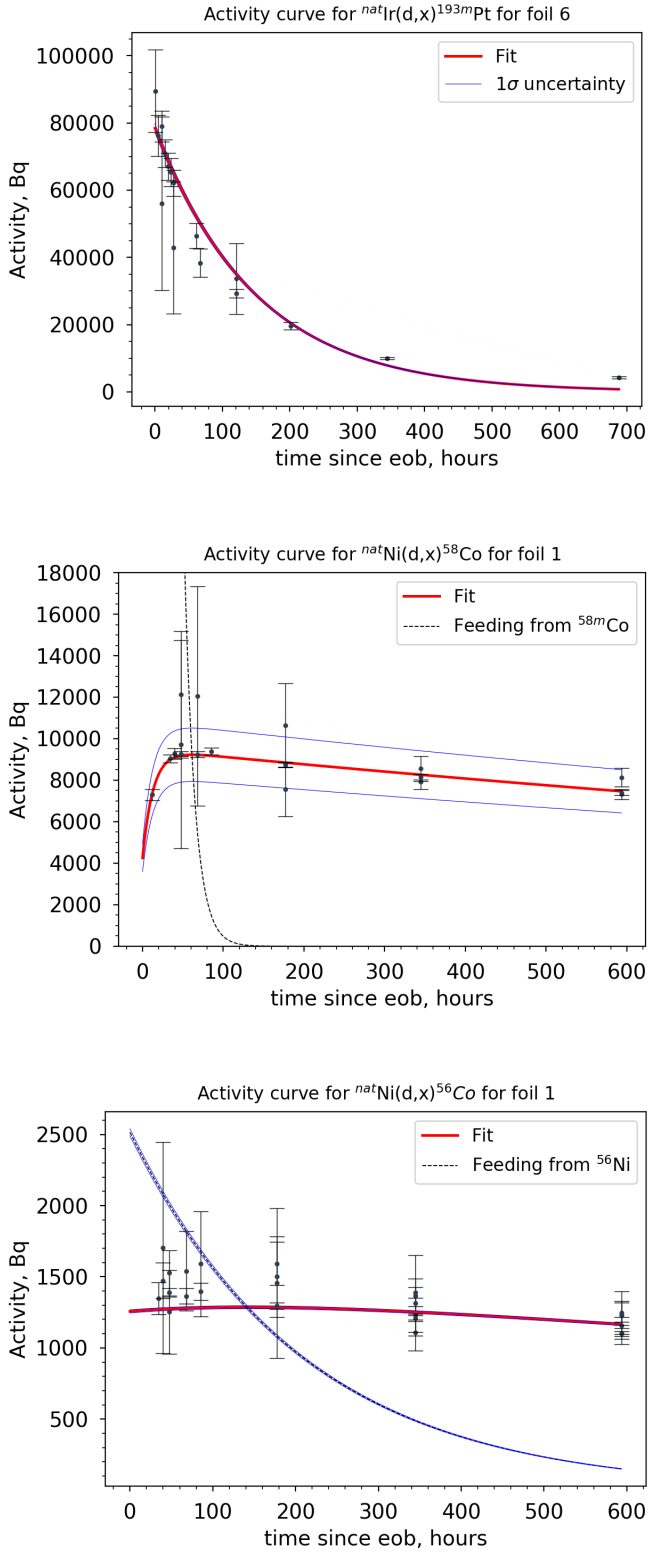

Figure 4.3: Examples of three activity curves. **Top:** Onestep decay for ^{193m}Pt ($t_{1/2}$=4.33 days), extrapolated with Equation 4.5. **Center:** Two-step decay for ^{58}Co ($t_{1/2}$=70.86 d) with feeding from the isomer ($t_{1/2=9.10}$ h, IT:100%). The curve was extrapolated using Equation 4.7 with both daughter and parent as optimizing parameters. **Bottom:** Two-step decay for ^{56}Co ($t_{1/2}$=77.236 d) with feeding from ^{56}Ni ($t_{1/2}$=6.075 d, ϵ:100%). Fitting to Equation 4.7 with the previously calculated A_0 for ^{56}Ni.

4.3 Monitor reactions

The requirement of monitor reaction-data used to calculate beam current or flux for beam-monitor reactions is well-characterized cross sections. The monitor cross sections were provided by the IAEA Coordinated Research Project on "Nuclear Data for Charged-particle Monitor Reactions and Medical Isotope Production" [49]. The recommended curves are interpolations over the recommended data, fit to an analytical approximation based on the ratio of two polynomials (Padé approximation), with uncertainties obtained using the co-variance matrix [49, p. 344]. The importance of well-known cross section to calculate the beam current cannot be emphasized enough. The monitor reactions make it possible to indirectly measure the beam current throughout the target stack, which yields precise measurements of the true beam current in each compartment. Therefore, it is very important to build confidence in the true excitation function, by measuring more experimental data.

In addition to measuring the beam current in each stack compartment, the monitor reaction data has two additional important aspects. The cross section around the compound peak changes rapidly, and is thus very sensitive to changes in energy. This is helpful for calculating foil energy assignments via transport simulations, which in this analysis was done using the NPAT Ziegler simulation [73], described in more detail in the next section. This is thus very important for thin target measurements, where precise assignments of energy bins are crucial [18].

An ideal monitor reaction needs to have strong and independent, high-intensity gamma-lines which are not contaminated by a typical background line, and easily identified after irradiation. The half-life should be sufficiently long for detection, and for these types of experiments where the activities are back-propagated in time, there is a clear advantage in multiple observations with good statistics. In addition, it is a clear advantage if the radionuclide not is subject to feeding from a parent nucleus co-produced by activation of the target. The decay products also plays an important role, because if the daughter is subject to decay feeding from more than one radionuclide, the chances of multiple shared lines are high. Secondary neutrons can cause large uncertainties in an experiment, and choosing monitor reactions which cannot be produced via (n,x) reactions is convenient.

An additional nickel monitor foil was placed in the back of the target stack (Table 3.1), behind a 1900-mm thick aluminum degrader to completely stop any deuterons or secondary protons from activating the foil. The aim was to look for the presence of secondary neutrons following deuteron breakup. From the monitor reactions, the only two reactions which also could be produced from

neutrons were ^{nat}Ni(n,x)^{56}Ni and ^{nat}Ni(d,x)^{58}Co from nickel. Mp induced activity was measured in the neutron monitor, so secondary neutrons assumed to play a negligible role.

4.3.1 End of beam activity calculations for the monitor reactions

The gamma-lines and intensities used to obtain end of beam activities are listed in Table C.1, along with half-life and deuteron energywindow where the reactions occur. The products from ^{nat}Fe(d,x)^{56}Co ($t_{1/2}$=77.236 d), ^{nat}Ni(d,x)^{61}Cu ($t_{1/2}$=3.339 h) and ^{nat}Cu(d,x)^{62,63,65}Zn ($t_{1/2}$=9.193 h, 38.47 m, 243.93 d) [63–65, 72, 74] were not subject to feeding from any other activation products and the end of beam activities were therefore calculated using single-step decay fits over the calculated activities as functions of time since end of beam. ^{nat}Ni(d,x)^{56}Co ($t_{1/2}$=77.236 d) [64] was subject to feeding from ^{56}Ni in the three first foils – all remaining nickel foils were below the energetic threshold of 25.5467 MeV for ^{nat}Ni(d,x)^{56}Ni. Therefore, the activities from the first three foils were calculated using a two-step decay fit, and the remaining foils were fitted to a single-decay fit. For ^{nat}Ni(d,x)^{58}Co ($t_{1/2}$=70.86 d) [71], feeding from the isomer ^{58m}Co was present, but the isomer does not have observable gamma-lines. The end of beam activities were calculated using a two-step decay fit. Since the monitor cross sections for ^{56,58}CoCo were cumulative, the independent cross sections ^{56}Ni and ^{56}Co, and $^{58m+g}$Co were added, and the uncertainty was calculated according to Equation A.13. Because of the low activation from ^{56}Ni, the propagated uncertainties in the three first foils of ^{56}Co was large, ranged from 3.9%-14.3%. The remaining uncertainties in the activities were less than 1.4%. For ^{58}Co, the total cumulative uncertainties ranged from 9.0%-32.5% (the independent cross section measurements of ^{56,58m,58g}Co are represented in subsection 5.3.2 in the next chapter). All monitor foils were activated in each compartment, except from ^{62}Zn which was present in the first six foils (with threshold at approximately 15 MeV), and ^{63}Zn which was present in the first nine foils (with threshold at approximately 8 MeV). All the gamma-lines used were independent, except for 846.770 keV (99.9399%), which was contaminated from ^{56}Mn, present in the first 25 hours after irradiation for ^{nat}Fe(d,x)^{56}Co.

4.4 Deuteron beam current and energy assignment

The beam-integrator (described in section 3.5) measured an average current of 128.5 nA in front of the stack. For accurate cross section measurements, the nominal beam current in each foil was calculated via the monitor reaction activities dis-

cussed above. The IAEA-recommended monitor reactions ^{nat}Ni(d,x)^{61}Cu,^{56,58}Co, ^{nat}Cu(d,x)^{62,63,65}Zn and ^{nat}Fe(d,x)^{56}Co [49] were used to obtain a weighted average beam current in each foil, solving Equation 3.7 for beam current Φ (deuterons/second):

$$\Phi(E_d) = \frac{A_0}{N_T \sigma(E_d)_{\text{mon}}(1 - e^{-\lambda \Delta t_{\text{irr}}})} \tag{4.8}$$

where E_{d} is the deuteron energy, A_0 is the end of beam activity for the monitor products calculated from the spectra for each monitor reaction, N_{T} is the number of target nuclei calculated from the areal density, N_{T} (nuclei/cm^2), $\sigma(E_{\text{d}})_{\text{mon}}$ is the monitor data from the IAEA database. Due to the thin foils used, it is reasonable to assume that the deuteron beam current should not be degraded within the same compartment – that is, for an Ir target foil and its adjacent monitor foils (Ni/Fe/Cu), in between any beam degraders (not used in this work). Within this method, referred to as variance minimization, it is possible to use multiple monitor reactions to determine the average beam current in each compartment. This increases the confidence in assigning the true beam current. This is provided that the simulated energy distributions are accurate. As stated by Graves *et al.* [28], this method of using multiple monitor reactions has the potential to reduce the uncertainties in the deuteron energy window towards the end of the stack.

Equation 4.8 builds upon the thin target assumption, which implies that the energy degradation within a foil is zero. However, due to the stochastic nature of particle transport, there is an energy distribution which was calculated using NPAT's (Nuclear Physics Analysis Tool) Ziegler class [73]. The Ziegler code simulates the deuteron transport in a Monte-Carlo based calculation, based upon the Anderson & Ziegler stopping power formalism [75]. The code was ran with $1 \cdot 10^6$ iterations with 100 discrete transport steps in each foil. The uncertainty in the stopping power energy was set to 0.5 MeV. Anderson & Ziegler is an empirical stopping power model, and takes the nuclear stopping-power (inelastic and elastic collisions), the electronic stopping power and the effective charge of the ions into account [76, p. 96]. This formalism offers a more realistic treatment of ion stopping powers than Bethe-Bloch (Equation 2.2), which only takes the electronic stopping power into account. Since both elastic and inelastic collisions are stochastic events, the range is represented as a distribution [76, p. 126]. The code provides the full deuteron energy and flux distribution in each foil, $d\phi/dE$, which can be visualized for the iridium foils in Figure 4.4. As the deuteron energy is degraded through the stack, the mean value is shifted towards the low-energy side of the distribution along with an increasing broadening of the flux distribution. Because the stopping power is inversely proportional to the charged particle energy (from Bethe-Bloch), the low-energy side of the flux is

more degraded than the high-energy side. This creates an increasing pronounced low-energy tail, and a shift of the mean energy (centroid) to lower energies. The increasing width of the distribution increases the uncertainty for foils further back in the stack. The flux-weighted average energy for each foil was calculated, which accounts for the slowing down of deuterons and gives the effective energy centroid in each foil [48], using the energy distributions $d\phi/dE$ provided by the Ziegler code:

$$\langle E \rangle = \frac{\int E \frac{d\phi}{dE} dE}{\int \frac{d\phi}{dE} dE} \tag{4.9}$$

The (asymmetric) uncertainty in beam energy is calculated from the intersection of the low-energy and high-energy tails, with the FWHM for the flux distribution in each foil (Figure 4.4).

Likewise, the energy-dependent monitor IAEA cross-sections need to be flux-averaged over each foil. This was done using the Scipy interpolation (splrep and splev) function with smoothing condition set o zero, and the order of derivative set to zero [61]. The energy array over each foil provided by the Ziegler simulation was spline interpolated with the IAEA-recommended cross section data. Thus, the monitor cross section term, $\sigma(E_\mathrm{d})_\mathrm{mon}$, in Equation 4.8 is modified to:

$$\langle \sigma(E_\mathrm{d}) \rangle = \frac{\int \sigma_\mathrm{mon}(E_\mathrm{d}) \frac{d\phi}{dE} dE}{\int \frac{d\phi}{dE} dE} \tag{4.10}$$

which modifies Equation 4.8 to:

$$\Phi(E_\mathrm{d}) = \frac{A_0}{N_\mathrm{T}(1 - e^{-\lambda \Delta t_\mathrm{irr}})} \cdot \frac{1}{\frac{\int \sigma_\mathrm{mon}(E_\mathrm{d}) \frac{d\phi}{dE} dE}{\int \frac{d\phi}{dE} dE}} \tag{4.11}$$

Equation 4.11 reduce back to Equation 4.8, with the flux-averaged monitor cross section representing an effective cross section for each foil. The integrals were numerically evaluated using the trapezoidal sum provided by the function trapz from the numpy package [77]. The function approximates an integral over a definite region divided into N intervals. The total integral is the sum of the area of each trapezoid.

Similarly, for the uncertainty in the monitor cross sections, the relative uncertainty of the interpolated monitor cross sections were flux-averaged:

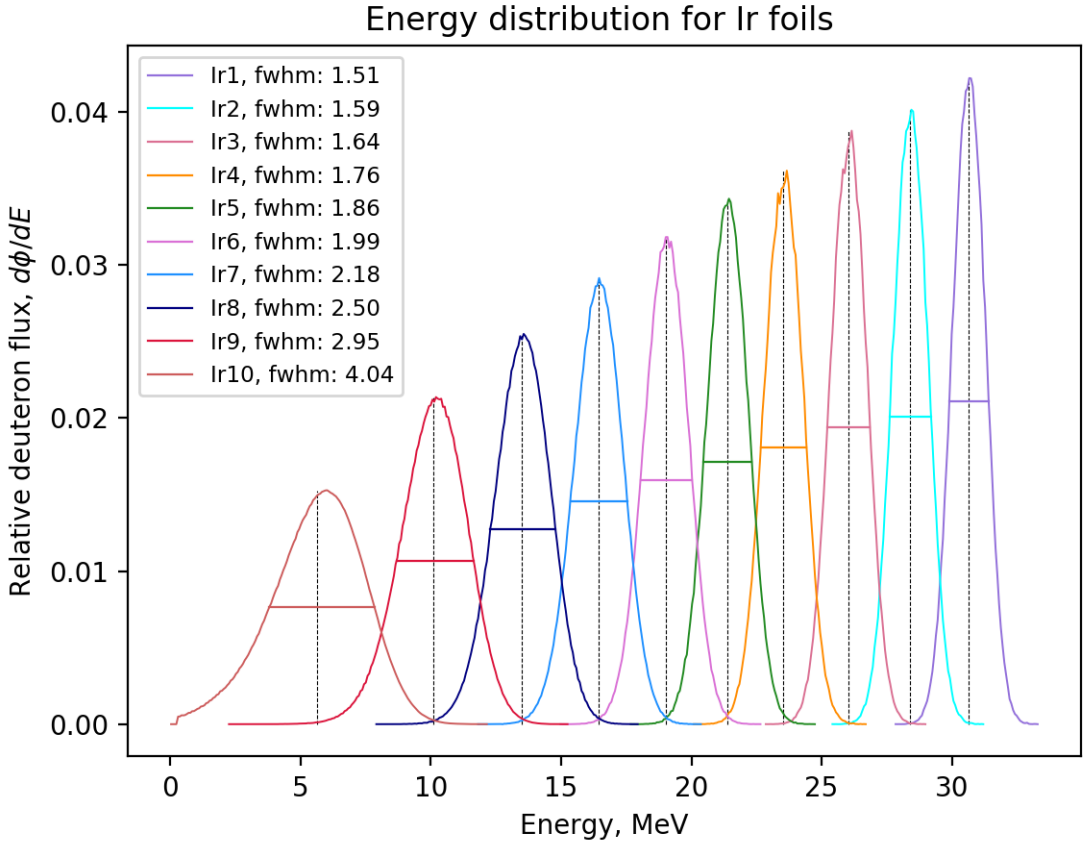

Figure 4.4: Iridium energy flux distribution for each of the 10 foils. As the energy degrades, the distribution becomes progressively more skewed, and the full width half max (FWHM) becomes progressively larger. The vertical line in each peak represents the mean flux-weighted average energy (Equation 4.9) This illustrates how the right uncertainty (δ^+), is greater than the left uncertainty (δ^-) in each distribution.

$$\langle \delta\sigma(E) \rangle = \frac{\int \frac{\delta\sigma_{\text{mon}}}{\sigma_{\text{mon}}} \frac{d\phi}{dE} dE}{\int \frac{d\phi}{dE} dE} \tag{4.12}$$

The beam current for each monitor reaction in each foil was calculated using Equation 4.11. The uncertainties for each current was calculated as the sum of partial derivatives (the square root of Equation A.8). The weighted average beam current were calculated using Equation A.16, and the uncertainty was calculated according to Equation A.17, using the weighted average based on the correlation between the input parameters in Equation 4.11 (which were heavily correlated).

The concept of weighted average is explained in more detail in Appendix A. Figure 4.5 (top) shows the calculated beam current for each reaction in each foil. However, the spread of the beam currents from the monitor reactions is large. The measured values of the beam current, especially in the back of the stack can be due to incorrect energy assignments in the Ziegler transport calculations. This is caused by uncertainties in incident beam energy distributions, poorly characterized stopping power calculations and additional systematic uncertainties, all of which increase progressively further back in the stack [48]. A way to work around this was to perform a "variance minimization" to find the correct energy assignments which reproduce the IAEA monitor cross sections, described in the next section.

4.4.1 Variance minimization

In theory, the current of a charged-particle should be attenuated at an approximately constant rate until the Bragg-peak, since the total reaction cross section is approximately constant across a wide range of energy. Variance minimization relies upon this, and was performed by systematically varying the incident deuteron beam energy and the effective areal density of the foils by a factor of up to $\pm 20\%$, and calculating the reduced χ^2 (Equation A.3) for all monitor reaction current in compartments 3, 6 and 9. Applying changes in the areal density and the beam energy does not imply that the nominal values were wrong, but are small corrections for improperly characterized deuteron stopping powers and systematic uncertainties in beam characterization to best reproduce the IAEA monitor cross section data [47]. This method was also performed in other similar experiments, [28, 33, 47, 48], but instead of varying the density of each target foil, the density of the energy degraders (not used in this work) was varied.

The reduced χ^2 was evaluated for Compartment 3 ($E_d \approx 26$ MeV), compartment 6 ($E_d \approx 19$ MeV) and compartment 9 ($E_d \approx 10$ MeV). In compartment 3, all the seven monitor products were above threshold, so the evaluation was based upon more measurements. However, since the degree of scattering early in the stack was low, the calculated χ^2_ν does not evaluate the effect of energy assignments further back in the stack. In compartment 6, the six possible reactions from nickel and copper were above threshold, and gave a good estimate of how the beam current was attenuating through the stack. In compartment 9, all reactions except $^{\text{nat}}$Cu(d,x)^{62}Zn and $^{\text{nat}}$Fe(d,x)^{56}Co were present. In this compartment, the full effect of energy assignments, along with the beginning of decrease in the beam current as the particles slow down can be seen. The cross section drops rapidly approaching the energetic threshold, thus the calculated beam current increases asymptotically (Equation 4.8) to compensate for this change. For $^{\text{nat}}$Cu(d,x)^{62}Zn (threshold at approximately 15 MeV), the threshold is in the energy range by foil

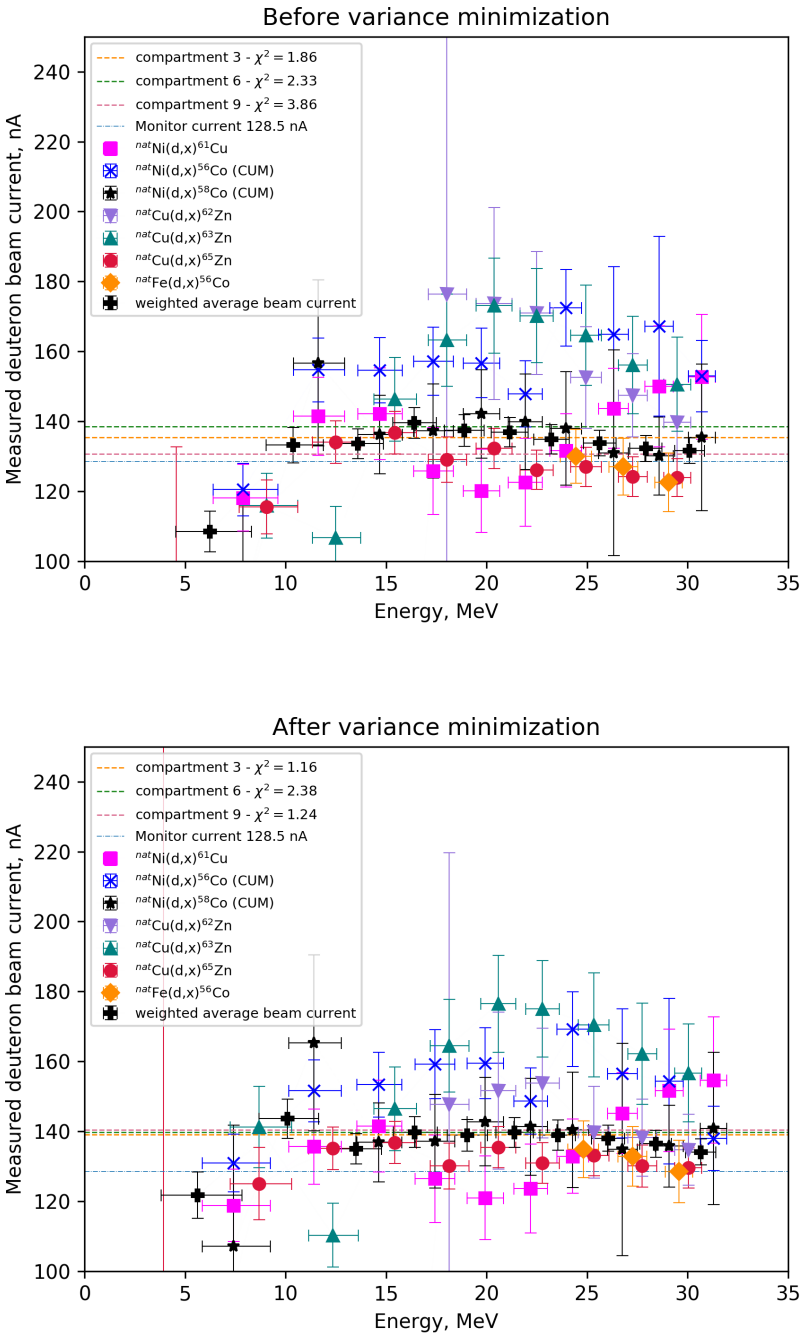

Figure 4.5: Beam current before and after variance minimization. The final energy assignments were calculated using a 2% increase in beam current and 4.25% increase in stopping power.

Cu07, and as a result, the uncertainty is very large in comparison to the other beam currents, which can be seen in Figure 4.5. The beam current is therefore very sensitive to changes here, and the uncertainty is large.

With the assumption that the beam current loss is zero over one compartment, a linear fit-model (using the Scipy Optimize Curvefit function [61]) with a slope equal to zero was used to calculate the best-fit beam current in compartment 3, 6 and 9, along with the reduced χ^2. Figure 4.7 shows the calculated reduced χ^2 for each iteration of the variance minimization as a function of the flux-weighted averaged beam energy entering compartment 6. There were several candidates which gave improvements of the beam current (Figure 4.5, top). The candidates had low values for reduced χ^2 over the selected compartments in particular for 6 and 9, and had positive change in areal density and beam current, ranging from 1–2.5% in incident beam current and 1.25–7.5% in areal density. This implies that the energy from the cyclotron tune was slightly larger than 33 MeV, or that the deuteron stopping power calculations was underestimated, since the beam energy and the areal density have compensating effects on the transport calculation. Of these candidates, a 2% increase in incident beam energy (33.7 MeV) and a 4.25% increase in effective areal density had the most consistent beam current within the evaluated compartments, and was therefore used for cross section calculations. Figure 4.6 shows the uncertainty weighted linear fit over compartment 6 using the scaling parameters of 2% increase in incident beam energy and 4.25% increase in effective areal density. The linear fits using the scaling parameters predicted a beam current of 139.08 ± 3.89 nA (χ^2_ν=1.16) in compartment 3, 139.73 ± 4.39 nA (χ^2_ν=2.38) in compartment 6 and 140.43 ± 5.03 nA (χ^2_ν=1.24). These values are higher than the expected current from the beam integrator, which was most likely due to incomplete charge collection or that the beam was stopped in the stack (based upon experiences from previous experiments using the 88-Inch Cyclotron).

Figure 4.5 shows the beam current before (top) and after (bottom) variance minimization. The weighted average beam currents before and after the variance minimization are also listed in Table 4.1. The variance minimization led to an overall more consistent weighted average beam current than the calculation using the original measured quantities, where $^{\text{nat}}$Ni(d,x)^{56}Co and $^{\text{nat}}$Cu(d,x)^{62}Zn were improved the most. $^{\text{nat}}$Cu(d,x)^{63}Zn consistently yielded too large values for the beam current in comparison to the other reactions above approximately 15 MeV. The changes in the beam current for the remaining reactions were minor before and after the variance minimization, confirming that the overall impact applying the variance minimization method on the transport calculation was minimal. With the exception of compartment 9, where the beam current is higher than before the variance minimization, the beam currents are more consistent across

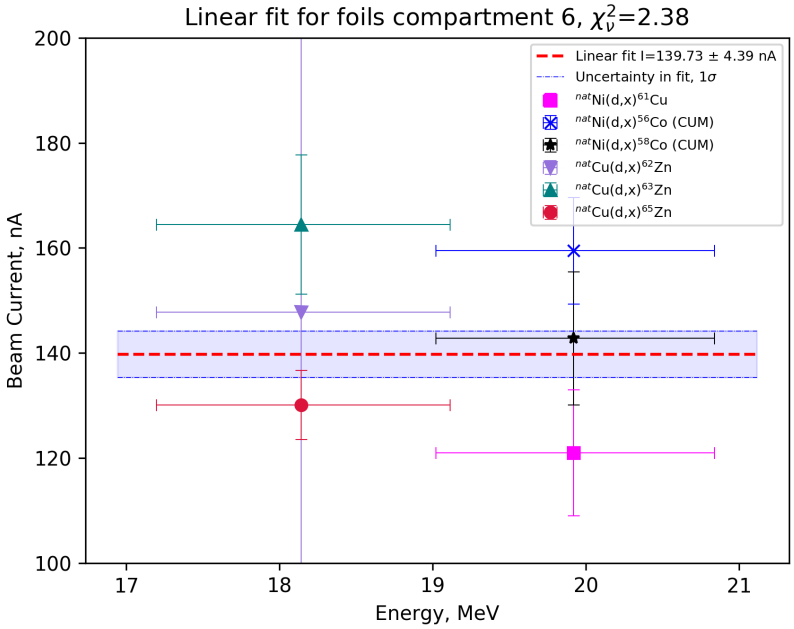

Figure 4.6: The calculated (uncertainty weighted) beam current over compartment 6 (Ni06/Cu06), with the change in parameters (2% increase in beam energy and 4.25% increase in foil effective areal densities).

the stack (Table 4.1). The beam currents calculated for each compartment (stippled lines in Figure 4.5) showed better agreement, and while the reduced χ^2 was about the same in compartment 6, it improved in both compartment 3 and visibly in compartment 9. In general, the points were more aligned with the new scaling parameters. Figure 4.8 shows the relative uncertainty in beam current in each compartment using the flux weighted average beam energies of iridium, along with the relative uncertainty in each reaction. It shows that the uncertainty increases as a function of decreasing energy, which makes sense due to the increasing uncertainty in the energy assignments towards the back of the stack. Yet a relative uncertainty of less than 5.5% in the average beam currents is found for all compartments, comparable to previous measurements using the variance minimization approach [28, 33, 47, 48]. It is also clear that large uncertainties are weighted less than small uncertainties.

To visualize how the energy assignments performed for the monitor reactions, the monitor cross sections were calculated using the weighted average beam current calculated in each monitor foil (– i.e. not the beam current for each individual reaction). Figure 4.9, Figure 4.10 and Figure 4.11 shows the excitation functions as function of deuteron energe for $^{\text{nat}}$Fe(d,x) (first figure), $^{\text{nat}}$Ni(d,x)

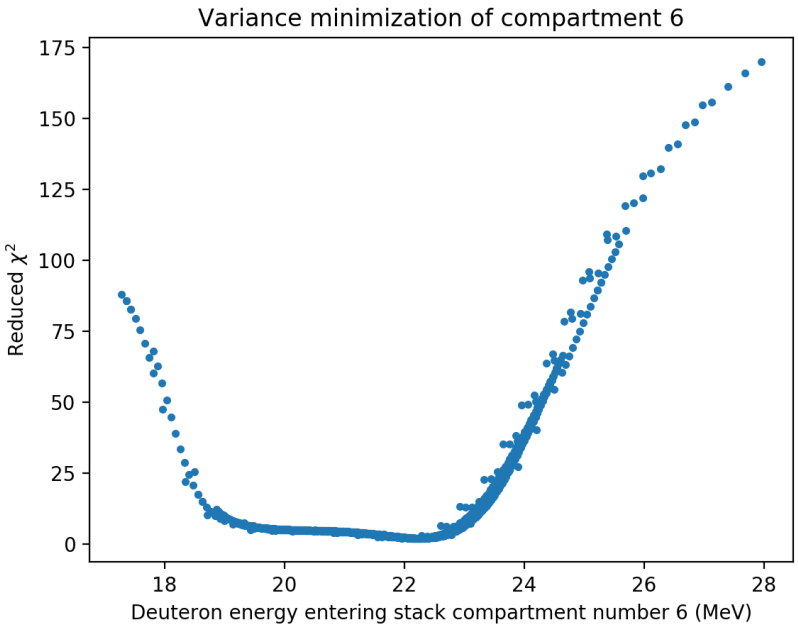

Figure 4.7: The figure shows the calculated reduced χ^2 as a function of the deuteron energy entering the stack (essentially the nickel flux weighted averaged beam energies).

Table 4.1: The weighted average beam current before and after variance minimization in each compartment. The beam current on the 88-Inch Cyclotron beam integrator was 128.5 nA.

Compartment	Before (nA)	After (nA)
01	131.56 ± 3.64	134.08 ± 3.70
02	132.23 ± 3.74	136.42 ± 3.83
03	133.81 ± 3.64	138.02 ± 3.75
04	134.89 ± 4.21	138.88 ± 4.31
05	136.85 ± 4.21	139.67 ± 4.29
06	137.40 ± 4.53	138.85 ± 4.58
07	139.55 ± 4.37	139.77 ± 4.37
08	133.60 ± 4.27	134.96 ± 4.32
09	133.16 ± 5.04	143.59 ± 5.67
10	108.49 ± 5.80	121.75 ± 6.65

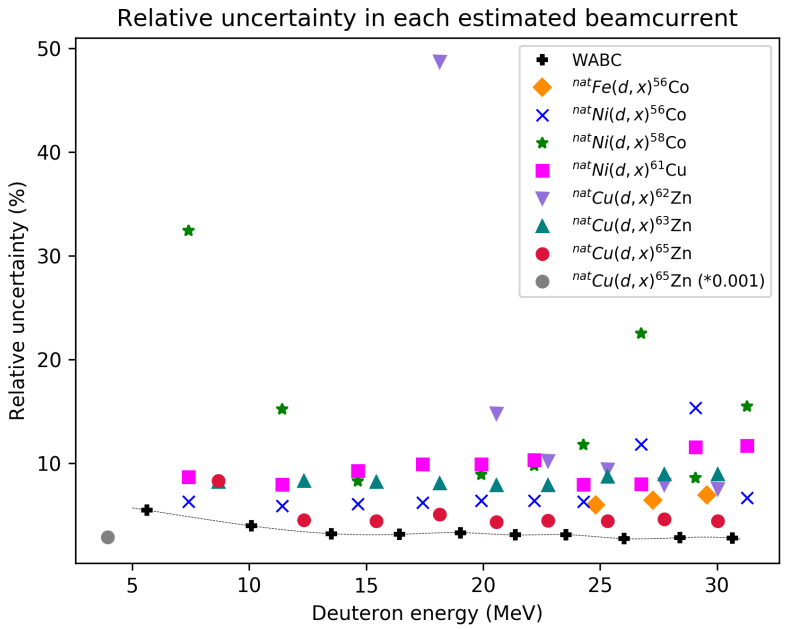

Figure 4.8: The relative uncertainty in the weighted average beam current (WABC) as a function of deuteron energy in each compartment. It is clear that the relative uncertainty is increasing as the reactions reach threshold (^{nat}Cu(d,x)^{62,65}Zn, ^{nat}Ni(d,x)^{58}Co), and in particular for ^{65}Zn (which is scaled down for Cu10 by 10^{-3} to make it fit on these axes). The uncertainty in the weighted average beam current is clearly weighted by the low uncertainty points.

(second figure) and ^{nat}Cu(d,x) (last figure)[1]. All the measured cross sections, within uncertainties, agree with the recommended data, except for ^{nat}Cu(d,x)^{63}Zn (Figure 4.11, center). For ^{nat}Cu(d,x)^{63}Zn, the measured cross section does not agree with the recommended data on the pre-equilibrium tail. A source for this particular error was not found in the experimental data, using independent, non-contaminated gamma-lines. The amount of experimental data is weak in the region, and the recommended data is heavily influenced by the measured data from Tacaks *et al.* [79]. The measured cross sections in this work agree with the existing experimental data from Ochiai *et al.* [80] in particular for the pre-equilibrium region. There is clearly need for more experimental data on the pre-equilibrium tail, and a re-evaluation of this monitor reaction channel is needed following additional measurements. The consistent high beam current at high energies caused by this reaction (Figure 4.5) can also be explained by this. A lower cross section value would increase the value of beam current proportionally. This applies for the inconsistent values in beam current in the beginning of the stack also, in particular for ^{61}Cu and ^{56}Co can be explained by the excitation functions (both cross sections figured in Figure 4.10, top and center, respectively). ^{61}Cu "oscillates" over the recommended IAEA-cross sections, which can also be seen on Figure 4.5, as the value oscillates over the weighted average beam current. ^{56}Co is consistently higher than the weighted average beam current (in Figure 4.5), which is explained by the cross section consistently being higher than the recommended cross sections. The general conclusion regarding the energy assignments is that there is good agreement within uncertainties in the compound peaks. It is clear that where there is a rapid change in the excitation function, the energy assignments seem to be slightly off, which is expected, due to cross sections being very sensitive to small changes in energy. The measured points in the pre-equilibrium tail region are in good agreement with the recommended data, with the exception being ^{nat}Cu(d,x)^{63}Zn.

4.5 Cross sections

With the measured end-of-beam activities, A_0 (Bq), for the observed product nuclei, the weighted average beam current calculated from the monitor reactions, Φ (deuteron/second), and the number of target nuclei, N_T (nuclei/cm^2) in each foil, the cross sections as a function of the weighted average beam energy, $\sigma(\langle E_d \rangle)$ were finally calculated, using Equation 3.7:

[1]The calculated cross sections from the monitor reactions are compared to the experimental data found in the EXFOR database [78], which is not necessarily what was used to calculate the recommended data. The datasets which were used can be find in the reference: [49]

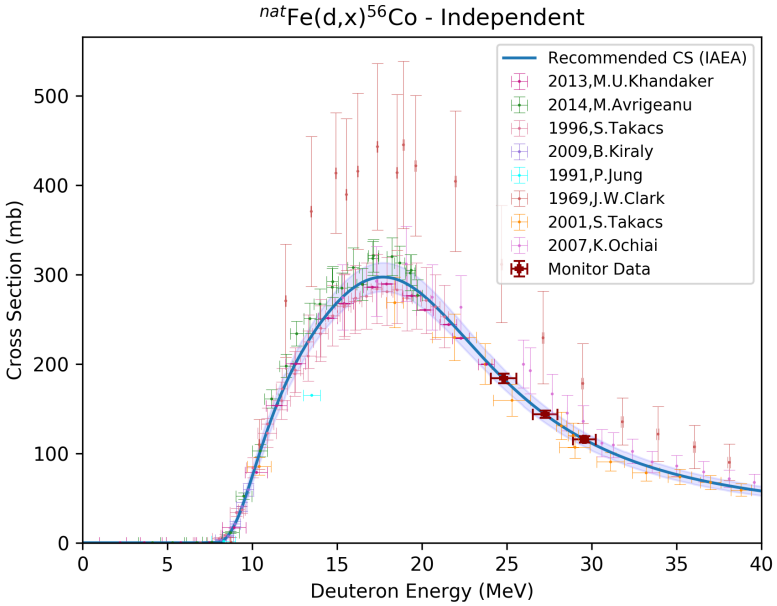

Figure 4.9: The figure shows the calculation of monitor cross sections for ^{nat}Fe(d,x)^{56}Co using the beam current calculated from this reaction. Experimental data from: [80–86]

$$\sigma(E) = \frac{A_0}{\Phi(E) N_T (1 - e^{-\lambda t_{\mathrm{irr}}})} \tag{4.13}$$

The cross section results are represented in the next chapter. Nuclei subject to decay feeding are reported as cumulative, as well as the first observed element in a decay chain, due to the possible feeding from short-lived activities. The remaining activities which were not subject to feeding were reported as independent. Whenever it was possible to extract parent feeding from daughter activity, using the two-step decay equation (Equation 4.7), both the cumulative and independent cross sections were reported. In addition, if a parent nucleus with an independently measured cross section, σ_{p}, fed into the daughter nucleus, the total cumulative cross section measured from the daughter nucleus σ_{c} was:

$$\sigma_{\mathrm{c}} = \sigma_{\mathrm{p}} * BR + \sigma_{\mathrm{d}} \tag{4.14}$$

where σ_{d} is the independent cross section for the daughter nucleus. BR is the branching ratio, which accounted for the feeding percentage from the parent nucleus. The independent daughter cross section can thus be calculated by sub-

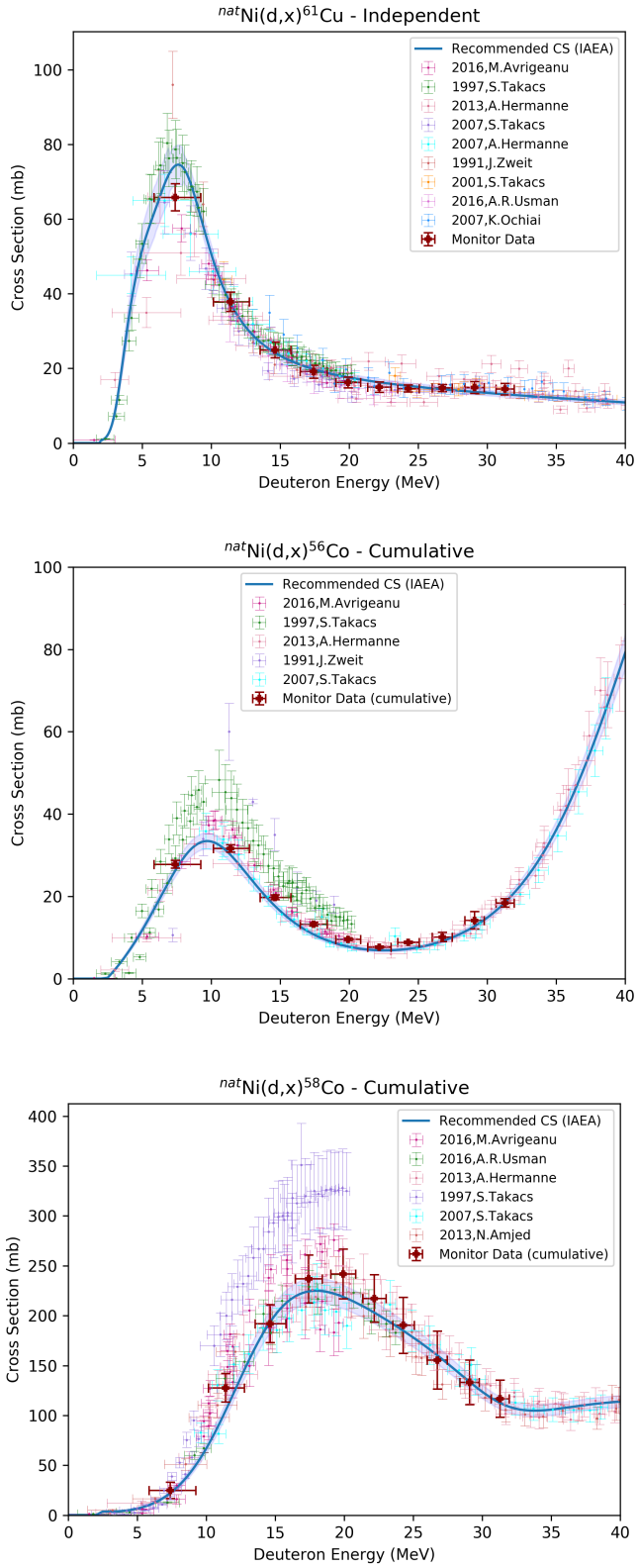

Figure 4.10: The figure shows the calculation of monitor cross sections for ^{nat}Ni(d,x)^{56,58}Co,^{61}Cu using the weighted average beam current calculated from the nickel foil. The values are compared with the recommended monitor data for the reaction, along with experimental data found in the EXFOR database. Experimental data from: [13, 80, 83, 86–92]

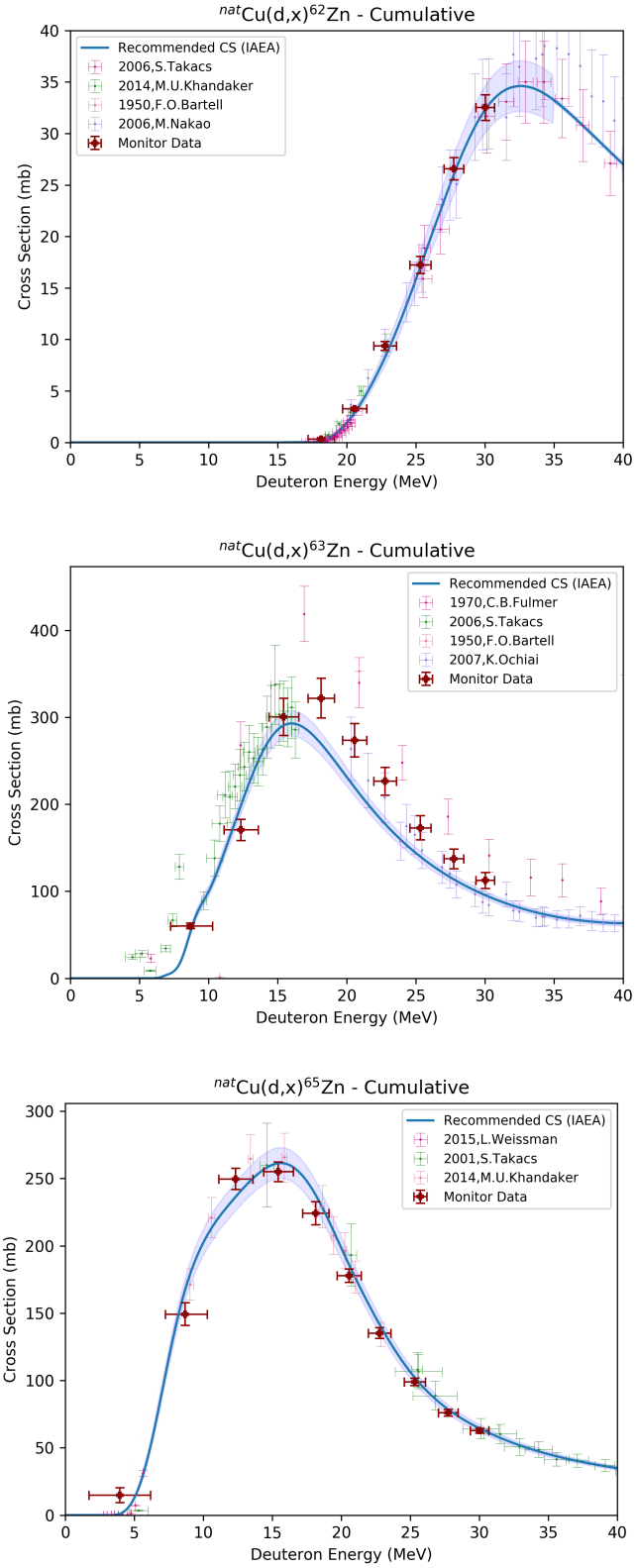

Figure 4.11: The figure shows the calculation of monitor cross section ^{nat}Cu(d,x)^{62,63,65}Zn. using the calculated weighted average beam current calculated from these reactions. The values are compared with the recommended monitor data for the reaction, along with experimental data found in the EXFOR database. Experimental data from: [79, 80, 93–97]

tracting the total cumulative cross section and the cross section from the parent cross section. Likewise, if two independent cross sections of daughter and parent were observed, the cumulative cross section is reported by adding together, weighted by BR.

The measured data is compared to previous experimental data from the EXFOR-database [78], along with the nuclear reactor modelling codes TALYS-1.9, TENDL-2019, ALICE-2017, CoH-3.5.3 and EMPIRE-3.2.3 [13–17]. The four former codes were ran with the same input models used in [33], using default parameters. The exception was for CoH-3.5.3 where the run for deuterons on ^{193}Ir had to be changed since the sum of the individual processes (compound, direct and pre-equilibrium) was larger than the total cross section which is an unphysical behavior. The parameter *tweakSD*, which adjusts the effective single-particle state density for the exit channels of alpha-particles, protons and neutrons, was set to 0.25, which is a 25% change of its default value. For each code, the energy-region from 0 up to 40 MeV was modelled.

Chapter 5

Results and Discussion

In this work, the main motivation was to measure the production cross sections for ^{nat}Ir(d,x)-reactions, with a special emphasis on the reaction producing ^{193m}Pt. In order to use this radionuclide in targeted radionuclide therapy, the production route must be well-established. We want to determine the deuteron energy window which optimizes the production while minimizes platinum-contaminants. The production cross sections for ^{nat}Ir(d,x) are presented in section 5.1. A discussion of the optimal energy window is given in **??**. A short description of the measured cross sections of products produced in the monitor foils are described in section 5.3. A description of each observed product from the monitor foil along with the excitation functions for the radionuclides from the monitor foils are listed in Appendix E.

The results from the cross section measurements obtained in this work are tabulated in Tables D.1, D.4, D.3 and D.4 for iridium, iron, nickel and copper, respectively. To reproduce cross sections for ^{nat}Ir(d,x)^{188,189,190,190,190,192,194,194m2}Ir, ^{188,189,191,193m}Pt, ^{nat}Fe(d,x)^{48}V, ^{51}Cr, ^{52,54,56}Mn, ^{59}Fe, ^{55,57,58}Co, ^{nat}Ni(d,x)^{52,54}Mn, ^{59}Fe, ^{55,57,58m,58g,60}Co, ^{56,57,65}Ni, ^{60,64}Cu and ^{nat}Cu(d,x)^{59}Fe, ^{60}Co, ^{61,64}Cu with correct energy assignments and beam current we had to apply a variance minimization to the deuteron transport calculation, increasing the incident beam energy with 2% compared to the cyclotron tuning which was 33 MeV, and a 4.25% change in the measured effective areal densities in the foils.. In general, the expected products were observed with a few exceptions; for instance ^{nat}Ir(d,x)^{191}Os. In the cases where the expected products were not observed, lack of strong and/or independent gamma-lines and too short counting times were the main reasons. For the ^{nat}Ir(d,x) reaction, the only reaction channels which were observed were via emission of up to one single proton and one or more neutrons, even though emission of alpha-particles is energetically possible. The Coulomb barrier constraint is larger for heavier target nuclei (Equation 2.12), and the cross sections are believed to be so low (mb, based on TENDL2019) that the products produced via ^{nat}Ir(d,xα) were not observable with gamma-ray spectroscopy.

In the results, the major source of uncertainties in the results are the end of beam activities, which were directly affected by the counting statistics, and the uncertainty in efficiency . The relative efficiency uncertainty varied from 0.8–48.0%, but as can be seen in Figure 3.7, the relative uncertainty for some of the detectors became large due to uncertainties in extrapolating beyond the gamma-lines emitted from the calibration sources. The areal density relative uncertainty (Table 3.1) was consistently low, ranging from 0.1–0.4% for the iridium foils, 0.2–0.6% for the iron foils, 0.1–0.6% for the nickel foils and 0.1–0.2% for the copper foils. The relative uncertainty in beam current (Figure 4.8) varied from 2.7–5.5%. Both areal density and beam current had constant value for all foils. The uncertainty in irradiation time (3600 ± 3 s) was also a constant value. The uncertainty in the constant, λ, was set to 0.1%.

The measured reaction cross sections were compared to calculations using TENDL-2019, TALYS-1.9, ALICE-2017, CoH-3.5.3 and EMPIRE-3.2.3. The general tendency was either shape or the magnitude was well predicted. The predictive power for strongly fed reaction routes was in general significantly better.

5.1 Cross section of ^{nat}Ir(d,x)-reactions

Natural iridium contains two stable nuclides; ^{191}Ir (37.3%) and ^{193}Ir (62.7%). The independent cross sections are reported for ^{188,189,191,193m}Pt and ^{188,194m2}Ir, along with the cumulative cross sections for $^{188,189,190,190m1+g,192,194}$Ir (described below). The measured cross sections in this work are compared to existing experimental data from Tárkányi *et al.* [11, 12] who have performed two similar experiments with deuteron energy in the ranges 1.7–38.0 MeV and 17.09–49.50 MeV, respectively.

The production of ^{191,193}Os ($t_{1/2}$=15.4 d (ground-state), 30.11 h, respectively) [4, 98] was expected on the deuteron energies covered in this work. They have low energetic threshold (obtained from [68]) for the reactions ^{191}Ir(d,2p)^{191}Os (Q_{value}=-1.8 MeV) or ^{193}Ir(d,α)^{191}Os (12.6 MeV) and ^{193}Ir(d,2p)^{193}Os (Q_{value}=-2.6 MeV). ^{191}Os has one strong gamma-line (129.431 keV, 26.50%) which is also populated in the decay of ^{191}Pt ($t_{1/2}$=2.802 d) (both nuclides decay to stable ^{191}Ir, thus populating the same state)[98]. This radionuclide was observed by Tárkányi *et al.* [12]. One suggestion for why ^{191}Os was not observed in this work was because the iridium-foils were not counted sufficiently long to observe this weakly fed channel. The measured cross sections by Tárkányi *et al.* are ranging without a clear trend from zero to 1.85 mb for deuterons up to 34.52 MeV. ^{193}Os was not observed. The common explanation is that the gamma-lines of both the

nucleus are weakly fed, combined with the fact that the reaction cross section is weak in this deuteron energy region. Radionuclides of rhenium and tungsten were also expected to be produced in a sufficient amount for observation via the (d,xαp) or (d,x2α) reaction channels, which were energetically possible, but those cross sections are expected to be even lower due to the extra emission of another charged particle.

^{nat}Ir(d,x)^{188}Pt (independent)

^{188}Pt ($t_{1/2}$=10.2 d) decays to ^{188}Ir (ϵ=100%) [99]. The end of beam activity was obtained using the relatively intense gamma-lines listed in Table D.1, using a single-decay fit (Equation 4.5). The lines were not contaminated by background radiation or by decay channels. This nuclide was produced via ^{191}Ir(d,5n) (Q_{value}=-26.1 MeV). Therefore, this product was only observed in foils 1, 2 and 3. The relative uncertainty in the end of beam activity was 13.6%, 28.2% and 26.6% in foil number 1, 2 and 3, respectively, which contributes to a larger net-uncertainty in the final cross section. The large uncertainty is caused by the low production of the radionuclide in the foils (near threshold for the reaction), and consequently, the cross sections suffer from poor statistics. The excitation function can be seen in Figure 5.1, and the measured cross sections are tabulated in Table D.1. There is no existing experimental data in the deuteron region from 26-30 MeV. The reaction models and the existing data agree that there is a rapid increase in the excitation function following the threshold. CoH-3.5.3 and TENDL-2019 is in particular in good agreement with the experimental data. TALYS-1.9 underestimate the magnitude of the compound peak, while EMPIRE-3.2.3 suggests that the rise of the excitation function is lower in comparison to the other reaction models. Compared to TALYS-1.9, EMPIRE-3.2.3 suggests a maximum shifted to higher energies.

^{nat}Ir(d,x)^{189}Pt (independent)

^{189}Pt ($t_{1/2}$=10.87 h) decays to ^{189}Ir (ϵ=100%) [100]. The end of beam activities were obtained using the relatively intense gamma-lines (higher than 1%) listed in Table C.2, which were not contaminated by background or by other decay channels. The activities were fitted to a single-decay curve (Equation 4.5). In this deuteron energy window, the only possible production route is via ^{191}Ir(d,4n) with Q_{value}=-19.3 MeV. Therefore, this product was only observed in the six first foils. The relative uncertainty in end of beam activities were below 4% for the four first foils, and increasing to 6.1% in foil 5 and to 25.7% in foil 6 (around the

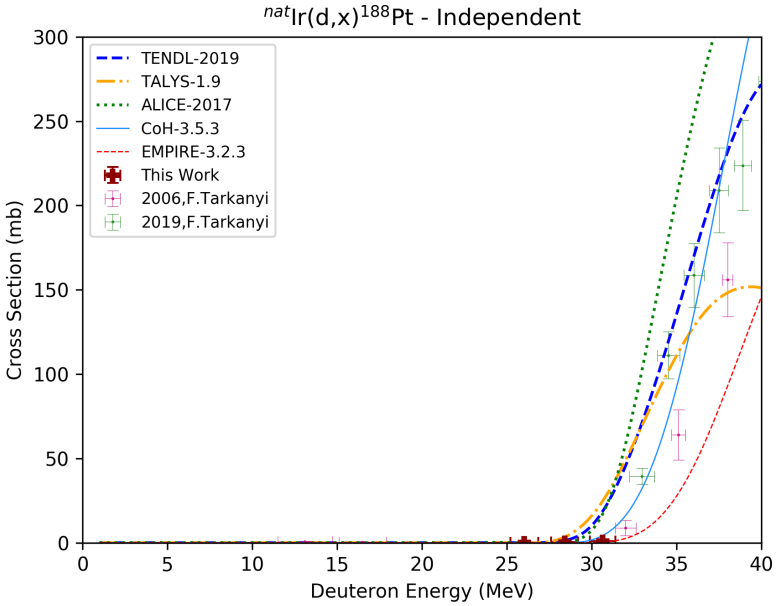

Figure 5.1: The excitation function for independent formation of ^{nat}Ir(d,x)188Pt. The cross sections from reaction threshold can be seen, and production is via ^{191}Ir(d,5n).

reaction threshold, where the activation was low). Figure 5.2 shows the excitation function for the reaction. Table D.1 lists the measured cross sections, and it is clear that this reaction is strongly fed from 26 MeV. The measured cross sections in this work is in good agreement with the existing experimental data from Tárkányi *et al.* [11, 12] up to beam energy 23.54 MeV. For higher deuteron energies, the values measured in this work are higher. The reaction models disagree on the maximum of the compound peak, where CoH-3.5.3 reproduces the magnitude of the experimental data, and EMPIRE-3.2.3 reproduces the shape best. TALYS-1.9 underestimates both the maximum of the peak and the magnitude.

^{nat}Ir(d,x)^{191}Pt (independent)

^{191}Pt ($t_{1/2}$=2.802 d) decays to ^{191}Ir (ϵ=100%) [98]. The activity curve was obtained using the high-intensity gamma-lines listed in Table D.1, fitted to a single-decay curve. This nuclide can be produced from ^{191}Ir(d,2n) (Q_{value}=-4.0 MeV) and via ^{193}Ir(d,4n) (Q_{value}=-18.0 Mev). Excluding the measured cross section in foil number 10, the relative uncertainty in end of beam activity is steadily

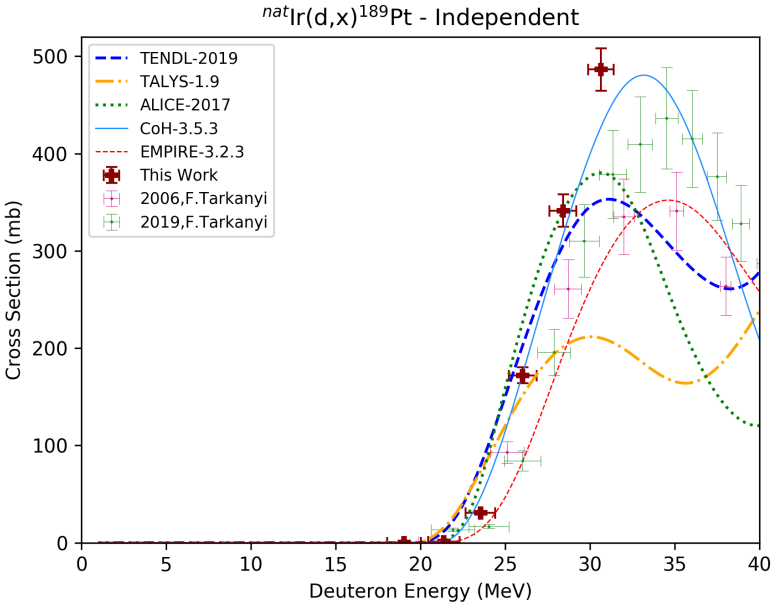

Figure 5.2: The excitation function for the independent production via ^{nat}Ir(d,x)^{189}Pt. The compound peak is caused by the reaction channel ^{191}Ir(d,4n) peaking at approximately 34 MeV. The ^{193}Ir(d,6n) reaction channel opens at higher deuteron energies.

below 0.3%, increasing slightly in the threshold region. This measurement is precise and reliable. The excitation function can be seen in Figure 5.3. The low energetic peak near 14 MeV is caused by the ^{191}Ir(d,2n) reaction, and the other is caused by the ^{193}Ir(d,4n) reaction, which is larger in magnitude. From Table D.1, the reactions leading to this product are strongly fed. The cross section measurements obtained in this work agree with the magnitude and shape of the existing experimental data, and are the most precise measurement to date. A well characterized ^{191}Pt excitation function is important for production as this radionuclide is the dominant radiocontaminant for ^{193m}Pt. None of the reaction models reproduce the total excitation function mapped out by the experimental data in a good way. The the low energy compound peak, TALYS-1.9 reproduce the shape and magnitude best. For the high energy compound peak, EMPIRE-3.2.3 reproduce the shape of the experimental data best. CoH-3.5.3, for a ^{193}Ir target, does not appear to reproduce a realistic model of the excitation function.

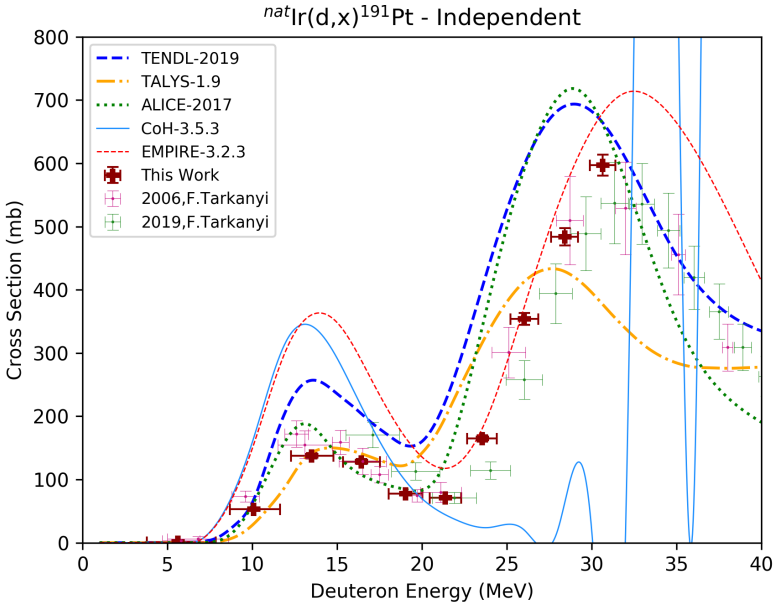

Figure 5.3: The excitation function for the independent production ^{nat}Ir(d,x)^{191}Pt. The low energy compound peak is caused by the ^{191}Ir(d,2n)^{191}Pt peaking at approximately 14 MeV. The high energy compound peak is caused by the reaction channel ^{193}Ir(d,4n)^{191}Pt, peaking at approximately 30 MeV.

^{nat}Ir(d,x)^{193m}Pt (independent)

The main interest in this work was the production of ^{193m}Pt, which decays by isomeric transition to the long-lived ground state of ^{193}Ir with a 4.33 days long half-life [4]. The decay of the ground state was not observed, due to the its long half-life ($t_{1/2}$=50 y), and lack of any decay gammas. The measured activities were fit to a single-decay curve, using the X-ray and the weak gamma-line listed in Table C.2. The high probability of internal conversion is the reason that this gamma-line is weak (135.5, 0.11%), and thus difficult to measure with low statistical uncertainty. Therefore, the 66.831 keV (7.21%) X-ray was also included, which improved the activity curves considerably. This X-ray is also present in ^{192}Ir ($t_{1/2}$=73.892 d) [62]. Since the cross sections of ^{192}Ir are comparable in magnitude in the same deuteron energy window (see Table D.1), only early observations of this X-ray was used. In the work by Tárkányi *et al.* [11], the X-ray was not used, and the measurement was obtained by subtracting the contribution from ^{192}Ir with the similar gamma-line (136.34 keV, 0.183%). Since the two lines were separable in this work, this was not done. The observed ^{193m}Pt activities are from the ^{193}Ir(d,2n) reaction (Q_{value}=-3.1 MeV). ^{193m}Pt was observed in each foil. The relative uncertainty in foil 1 (E_d = 30.0 MeV) is large, with the main contribution from the end of beam activity which was 12.9 %. For the remaining foils, the relative uncertainty is below 4%. The uncertainties in comparison to Tárkányi *et al.* (2006) are smaller (by a factor of approximately 6 at $E_d \approx 19$ MeV). The single compound peak along with the pre-equilibrium tail can be seen in Figure 5.4, suggesting an energy-window in the 11 to 18 MeV region where the cross section is highest. From Table D.1, it is clear that the reaction competes with ^{191}Pt, along with ^{192,194}Ir.

The cross sections measured in this work are in good agreement with the existing experimental data. Tárkányi *et al.* (2006) [11] measured the highest cross section value at 12.6 MeV (between 10.09 and 13.51 MeV in this work) of the compound peak which was 233.0 mb. It would have been nice to verify this with an additional data point between 10 and 13 MeV, to see where the maximum of the compound peak is, considering how sharply it turns over. Calculations using the different reaction models give results varying up to a factor of 5 and give a maximum at a higher deuteron energy than the experimental data. CoH-3.5.3 is not physically realistic, and is again a result of the complications of the reaction-modelling from ^{193}Ir. EMPIRE-3.2.3 and ALICE-2017 does the best job predicting the peak location, but are off in magnitude.

^{nat}Ir(d,x)^{188}Ir (independent and cumulative)

The cumulative and independent cross sections are reported for $^{188m1+g}$Ir (isomer: $t_{1/2}$=4.2 ms, ground state: $t_{1/2}$=41.5 h). The branching ratio of the isomer decaying into the ground-state is unknown. The radionuclide is in addition

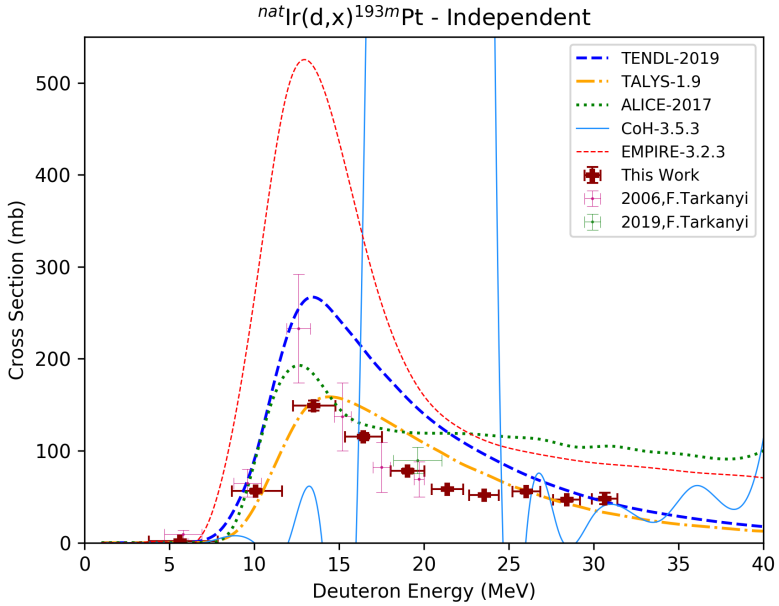

Figure 5.4: The excitation function for the independent production of ^{nat}Ir(d,x)^{193m}Pt. This nuclide is produced via ^{193}Ir(d,2n)^{193m}Pt, and the compound peak and pre-equilibrium tail is visible, peaking at approximately 12 MeV.

subject to beta-feeding from ^{188}Pt ($t_{1/2}$=10.16 d, ϵ=100%) with reaction Q-value -26.1 MeV [99]. In addition to indirect production from ^{188}Pt, ^{188}Ir can also be produced via ^{191}Ir(d,4np) (Q_{value}=-24.8 MeV). The activities were measured using the intense gamma-lines listed in Table C.2, which were not subject to contamination from background or other decay channels. The measured activities were fitted to a single-decay curve. This radionuclide was produced in foils 1, 2 and 3. The relative uncertainties in end of beam activity were 6.5%, 13.7% and 22.2% in foils 1-3. The cumulative cross section with feeding from ^{188}Pt and the subtracted cross section of $^{188m1+g}$ is reported, and the excitation functions can be seen in Figure 5.5. There is no existing experimental data in the deuteron beam region up to 30 MeV, but comparing the measured cross sections in this work, the threshold from the reaction models suggests that the values for both excitation functions are reasonable. However, in the top figure, the rapid increase in the excitation function from the reaction models does not agree with the existing data by Tárkányi *et al.* (2006) [11] (measured between 35 and 40 MeV). In the top figure, all reaction models agree acceptably internally, except for ALICE-2017 which is clearly not predicting an increase in the excitation function. In the bottom figure, it can be seen that the main contribution in the cumulative cross section including the beta-feeding component from ^{188}Pt. This is also supported

in Table D.1. At 30 MeV, the measured subtracted cross section is a factor of 3.5 times smaller than the directly measured cross section. For the subtracted cross sections, TENDL-2019 and TALYS-1.9 agree in this deuteron region, while EMPIRE-3.2.3 overestimates and CoH-3.5.3 underestimates the increase in the excitation function. ALICE-2017 does not give a reasonable prediction.

^{nat}Ir(d,x)^{189}Ir (cumulative)

^{189}Ir ($t_{1/2}$=13.2 d) decays to stable ^{189}Os (ϵ=100%). This radionudlice is subject to beta-feeding feeding from ^{189}Pt (10.87 h, ϵ=100%) with a reaction Q-value -19.3 MeV. [100]. In addition to indirect production, ^{189}Ir can be produced directly via ^{191}Ir(d,4np) (Q_{value}=-16.6 MeV) and via ^{193}Ir(d,5np) (Q_{value}=-30.6 MeV). Activity from ^{189}Ir was measured in foils 1-4. The activity was measured using one relatively strong gamma-line (6.0%) and one weaker line listed in Table C.2, which were not contaminated by background or other decay channels. The measured activities clearly showed the typical two-step curve (example-wise shown in Figure 4.3 for ^{56,58}Co), but fitting the measured activities to a two-step decay curve led to a very negative end of beam activity, which is not physical. Therefore, only activities calculated from spectra where ^{188}Pt had decayed completely (assuming that the product had decayed completely after ten half-lives) were used to obtain the end of beam activity. The measured activities were thus fitted to a single-decay curve. The relative uncertainties was between 6.5 and 7% for foils 1-3, and 30.7% in foil 4 which is around threshold for the reaction. Figure 5.6 shows the excitation function for the reactions leading to this product nucleus, compared to existing experimental data and reaction modelling codes. The experimental data published by Tárkányi *et al.* (2006) [11] is in good agreement with this work. However, the experimental data published by Tárkányi *et al.* (2019) [12] suggests that the compound peak is shifted about 10 MeV up. The group have not commented on anything which was done differently, but the reaction modelling codes suggests that this work and the work done by Tárkányi *et al.* (2006) is in better compliance with the true result.

From Table D.1, it can be seen that the cumulative cross section for ^{189}Ir is lower than the independent cross section of ^{189}Pt. This results in negative independent measurement of ^{189}Ir (since the branching ratio between ^{189}Pt and ^{189}Ir is 100%). This has not been commented in the literature, and can imply that the absolute intensity normalization of the decay-gammas can be wrong. Therefore, only the cumulative measurement is reported in this work.

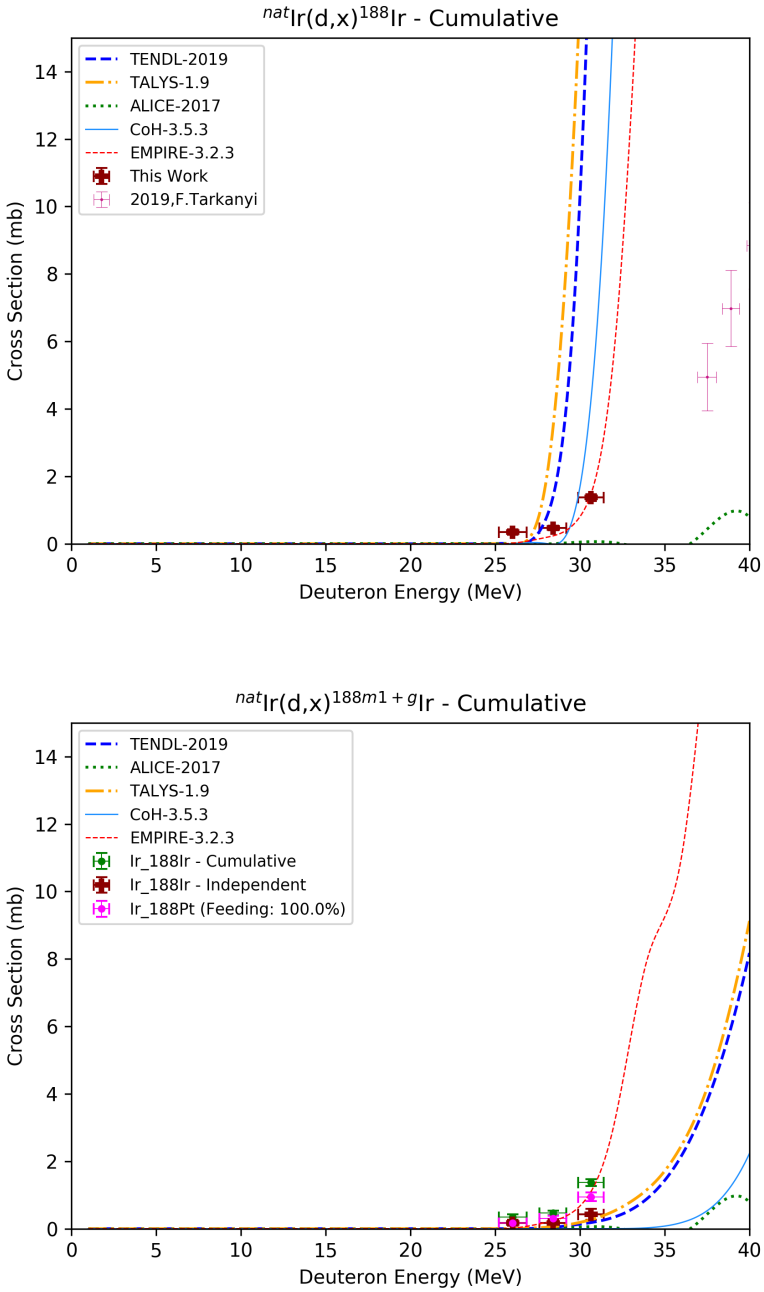

Figure 5.5: The excitation function for the cumulative production ^{nat}Ir(d,x)^{188}Ir. In the deuteron energy window used in this experiment, the direct production is from the ^{191}Ir(d, 4np)^{188}Ir. In addition, indirect production via beta-feeding from ^{188}Pt is present. **Top:** Total cumulative cross section, including beta-feeding from ^{188}Pt. **Bottom:** The cumulative cross section of formation of the ground state and isomer. The independent cross section from ^{188}Pt was subtracted from the total cumulative cross section.

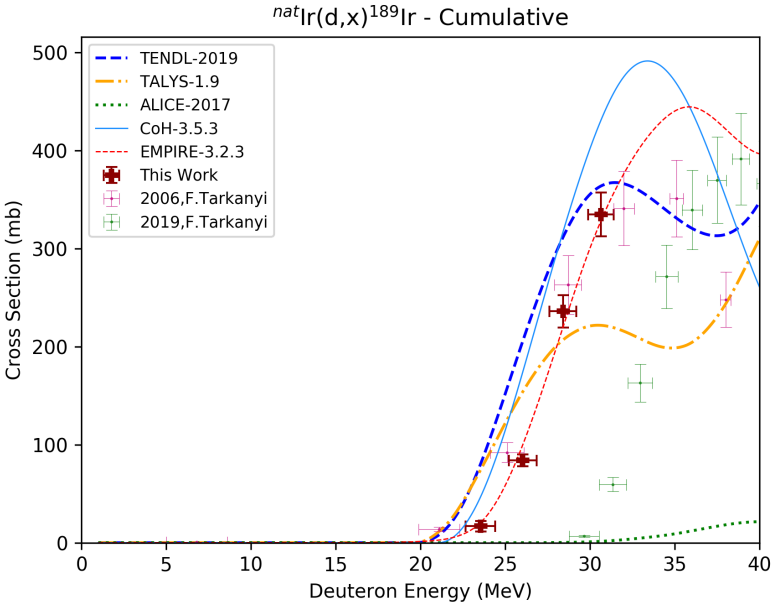

Figure 5.6: The excitation function for the cumulative production ^{nat}Ir(d,x)^{189}Ir. The ^{191}Ir(d,4np) is visible in the first compound peak. The second compound peak from ^{193}Ir(d,6np) opens for higher energies which will contribute to a second compound peak. In addition, indirect production via beta-feeding from ^{189}Pt is present. The existing experimental data from Tárkányi *et al.* (2019 [12]) disagree with the data in this work, the data from Tárkányi *et al.* (2006 [11]) and the reaction models.

^{nat}Ir(d,x)^{190}Ir (cumulative) and ^{nat}Ir(d,x)^{190m2}Ir (independent)

The cumulative measurement of $^{190m2+m1+g}$Ir, along with the cumulative measurement of $^{190m1+g}$Ir ^{190}Ir (m2: $t_{1/2}$ = 3.087 h, IT=8.6%, m1: $t_{1/2}$ = 1.120 h, IT=100%, groundstate: $t_{1/2}$ = 11.78 d) are reported. The ground state decays to stable ^{190}Os [62]. This radionuclide can be produced directly via ^{191}Ir(d,2np) (Q_{value}=-10.3 MeV) and via ^{193}Ir(d,4np) (Q_{value}=-24.2). ^{190}Ir was produced in foils 1-8. ^{190m1}Ir does not have observable gamma-lines. Therefore, the ground state and the isomer are reported together. The activities of the ^{190}Ir was calculated using the relatively intense, non-contaminated and independent gamma-lines listed in Table C.2, and fitted to a single-decay curve. Since the half-life of the ground-state is much longer than the isomers, the spectra taken from approximately 30 hours after end of beam (which is approximately 10 half-lives for ^{190m2}Ir) was used. The relative uncertainty was low, where all the end of beam activities had uncertainties ranging from 1.9% to 2.7% in foils 1-7 and 4% in foil 8, which was around threshold. Figure 5.7 (top) shows the excitation function of ^{190}Ir (including feeding from both isomers), where the measured cross sections from this work is in good agreement with the existing experimental data from Tárkányi *et al.* (2006) [11]. The possible production routes contribute to a to a rapid increase in cross section and a broad compound peak. Tárkányi *et al.* (2006) have reported measured cross sections in the 6-10 MeV deuteron region. The possibility of triton emission is present, which is weakly fed (with reaction Q_{value}=1.8 MeV from ^{191}Ir). The reaction models all predicts the same shape, but ALICE-2017 and CoH-3.5.3 predicts a higher reaction threshold and a lower magnitude of the curve. None of the reaction models fit the shape of the experimental data well. Figure 5.7 (bottom) shows the excitation function for $^{190m1+g}$Ir, where the feeding from ^{190m2}Ir is subtracted. It is clear that the contribution from ^{190m2}Ir in the total cumulative cross section for ^{190}Ir, which is also supported by the measured values in Table D.1. One of the reasons has to do with the branching ratio of 8.6% from ^{190m2}Ir to the groundstate.

^{190m2}Ir decays by internal conversion to the ground state (8.6%) or by ϵ (91.4%) to stable ^{190}Os [101]. This isomer is not subject to feeding, and can be produced directly via ^{191}Ir(d,2np) (Q_{value}=-19.6 MeV) or via ^{193}Ir(d,4np) (Q_{value}=-25.0 MeV). This radionuclide was observed in foils 1-7. The decay curve was calculated using a single-step decay fit with two strong gamma-lines listed in Table C.2. Since these lines are present in the decay of the ground-state as well, only spectra which were taken within the ten first hours after end of beam was used. The gamma-lines were not contaminated by background radiation. The relative uncertainty in end of beam activities were 1.4% in foils 1-5, slightly increasing in foils 6-7 to 8.0%. In this reaction, production via triton emission seem to be present, since there is one measured point below the Q-value of 19.6 MeV, but as we can see the cross section listed in Table D.1 is extremely low. The excitation function can be seen in Figure 5.8. Both reactions contribute to

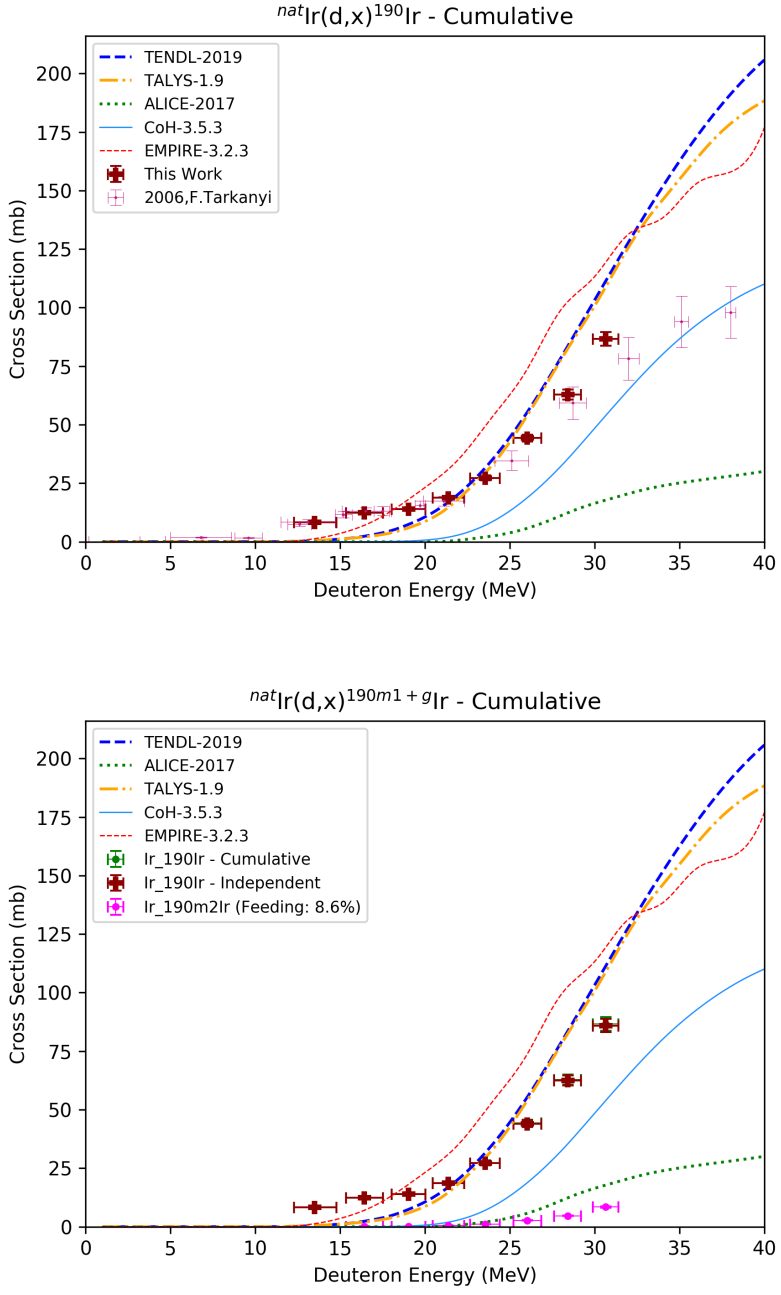

Figure 5.7: The excitation function for the cumulative production of ^{nat}Ir(d,x)^{190}Ir. The reactions ^{191}Ir(d,2np) and ^{193}Ir(d,4np) both contribute to a broad compound peak. **Top:** Total cumulative cross section, including isomer-feeding from ^{190m2}Ir. Both ^{191}Ir(d,) **Bottom:** The cumulative cross section of $^{190m1+g}$, where the independent cross section of ^{190m2}Ir multiplied with the branching ratio is subtracted.

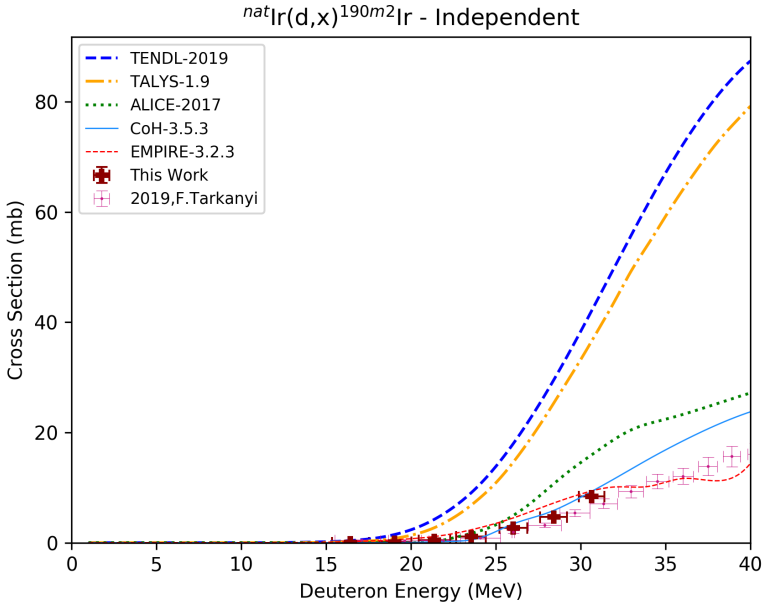

Figure 5.8: The excitation function for the independent formation of $^{\text{nat}}$Ir(d,x)$^{190\text{m}2}$Ir. Production from both ^{191}Ir(d,2np) and ^{193}Ir(d,4np) contributes to a broad compound peak.

a broad compound peak. The measured data in this work is in good agreement with the existing experimental data by Tárkányi *et al.* (2019) [12]. TENDL-2019 and TALYS-1.9 overpredicts the magnitude of the excitation function. ALICE-2017, EMPIRE-3.2.3 and CoH-3.5.3 reproduce the experimental well.

$^{\text{nat}}$Ir(d,x)^{192}Ir (cumulative)

The cumulative measurement of $^{192m2+m1+g}$Ir (m2: $t_{1/2}$=241 y, IT= 100%, m1: $t_{1/2}$=1.45 m, IT= 99.98%, groundstate: $t_{1/2}$=73.892 d) is represented in this work. The ground state decays to stable ^{192}Pt by β^--decay (95.24%) or to stable ^{192}Os by ϵ-decay (4.76%) [62]. This product is not subject to beta-feeding, and can be produced via ^{191}Ir(d,p)^{192}Ir (Q_{value}=4.0 MeV) and ^{193}Ir(d,2np)^{192}Ir (Q_{value}=-10.0 MeV). This product was observed in all iridium foils. The activity curve was calculated using a single-step decay. The gamma-rays are independent and not subject to background contamination, listed in Table C.2. The uncertainty in the end of beam activity was below 0.5% for all the measurements, except for the two last foils where the uncertainty increased to 0.5% and 1.3% in foils 9-10, respectively. The excitation function is represented in Figure 5.9.

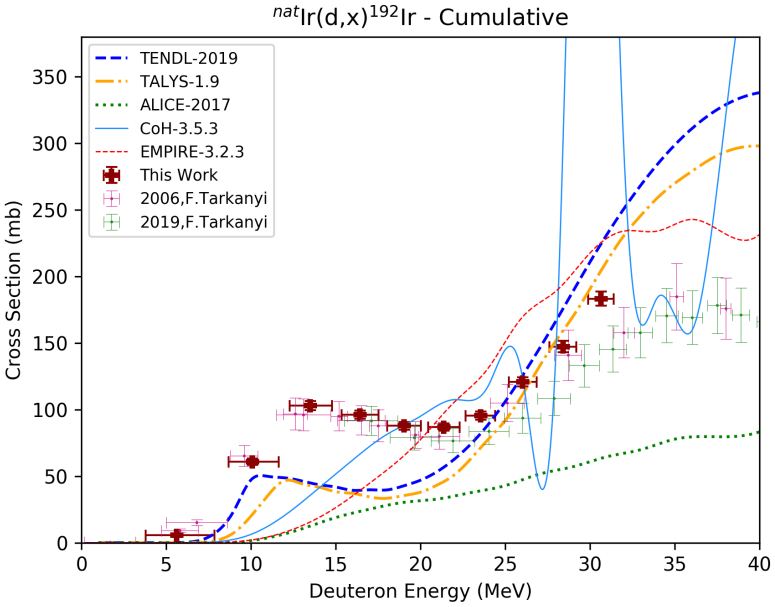

Figure 5.9: The excitation function for cumulative reaction ^{nat}Ir(d,x)^{192}Ir. Production from ^{191}Ir(d,p)^{192}Ir can be seen in the low energy compound peak peaking at approximately 14 MeV. The high energy compound peak is caused by the reaction ^{191}Ir(d,p)^{192}Ir peaking at approximately 35 MeV.

Both compound nuclear peaks resulting from the ^{191}Ir(d,p) and ^{193}Ir(d,2np) reactions can clearly be seen. Comparing the measured cross sections to existing experimental data, the measured cross sections in this work is in agreement up to ca. 21 MeV, with a larger increase at the highest measured cross sections. Regarding the reaction modelling codes, all perform poorly; CoH-3.5.3, EMPIRE-3.2.3 nor ALICE-2017 even predict the first compound peak, and are wrong in magnitude for the second compound peak, where ALICE-2017 underestimates the magnitude, EMPIRE-3.2.3 overestimates the magnitude, and as expected from CoH-3.5.3, the models behaves in a non-physical manner from ^{193}Ir as target. TENDL-2019 and TALYS-1.9 predicts both compound peaks, but underestimates the magnitude of the low-energy compound peak, and does not agree with the data on the position. However, shape and magnitude wise, TENDL-2019 and TALYS-1.9 agree with the high-energy compound peak (for the three highest measured values obtained in this work).

^{nat}Ir(d,x)$^{194m1+g}$ (cumulative)

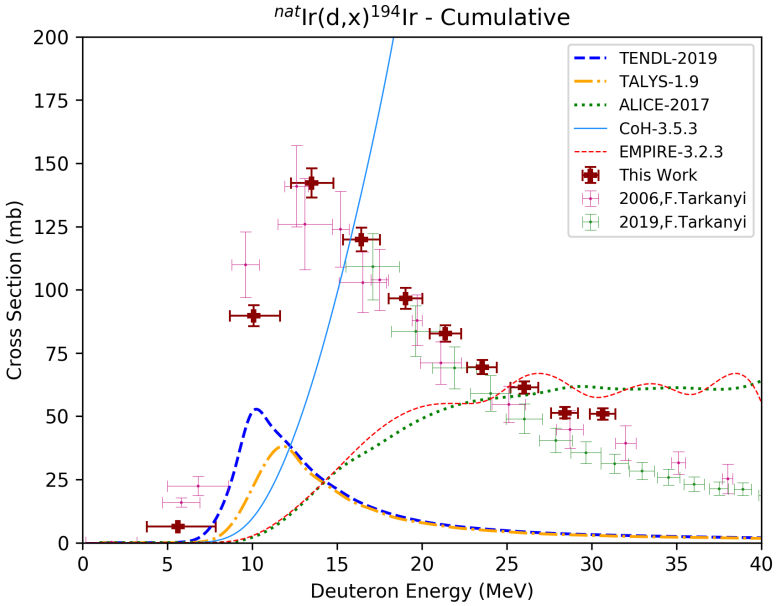

Figure 5.10: The excitation function for cumulative reaction $^{\text{nat}}$Ir(d,x)^{194}Ir. This product is only produced via ^{193}Ir(d,p)^{194}Ir, where the excitation function peaks at approximately 15 MeV.

The cumulative cross section $^{194\text{m1+g}}$Ir (isomer: 31.85 ms, IT=100%, ground-state: $t_{1/2}$=19.28 h) is reported. This radionuclide has one additional isomer which decays by β^- to stable ^{194}Pt (100%), and is described in the next paragraph [102]. ^{194}Ir decays by β^- to ^{194}Pt [102]. This product can be produced via ^{193}Ir(d,p) (Q_{value}=3.8 MeV). The activities were calculated using one relatively intense gamma-line and two weak (below 1%), listed in Table C.2. The measured activities were fitted to a single decay curve. Since the (d,p) reaction is well fed, it is clear the statistical uncertainties were low, being between 2.3% and 3.9%. The gamma-lines are not contaminated by background radiation or other decay channels. Figure 5.10 shows the excitation function. The existing experimental data from Tárkányi *et al.* (2006, 2019) [11, 12] are in good agreement with this measured cross sections in this work. The experimentally suggests that the compound peak is located at ca. 12 MeV, following the pre-equilibrium tail. The reaction models performs poorly, where the magnitude is off for each single code. It is clear that TALYS-1.9 and TENDL-2019 approximates the compound peak differently, where those performs good shape-wise, than ALICE-2017 and EMPIRE-3.2.3 where no compound peak at all is predicted. CoH-3.5.3 behaves unphysical because of the difficulties with modelling the reactions from ^{193}Ir. Table D.1 shows that the reaction competes with the ^{193}Ir(d,2n)$^{193\text{m}}$Pt reaction in the low energy region.

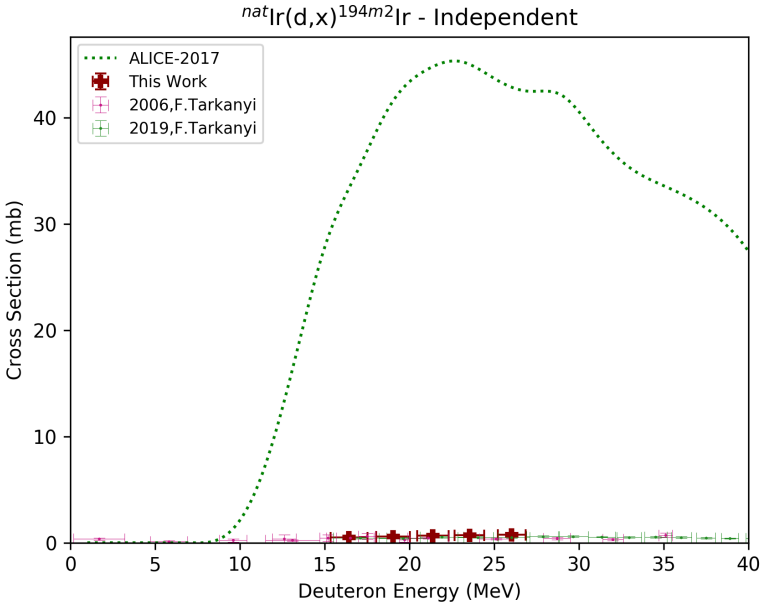

Figure 5.11: The excitation function of ^{nat}Ir(d,x)^{194m2}Ir. This radionuclide is produced via ^{193}Ir(d,p)^{194m2}Ir. ALICE-2017 clearly overestimates the production cross section, with a factor of 56 at the peaking of the model.

^{nat}Ir(d,x)^{194m2}Ir (independent)

The production of the independent cross section of ^{194m2}Ir ($t_{1/2}$=171 d) is reported. ^{194m2}Ir decays to stable ^{194}Pt (β^-=100%). The isomer was measured independently, since it is not subject to feeding [102]. Since the energy-level is unknown (per may 2020), the reaction Q-value is also unknown. This radionuclide was observed in foils 3-7. The gammalines used to calculate end of beam activities are listed in Table C.2, and were not contaminated by background or other reaction channels. The relative uncertainty in end of beam activities ranged from 7.7-22.4%, due to low activation and poor statistics. From Table D.1, the measured cross sections are low, and it clear that the the isomer-to-groundstate branching ratio for ^{194m2}Ir/$^{194m1+g}$Ir is small. The excitation function can be seen in Figure 5.11. The measured data in this work is in well agreement with the existing experimental data by Tárkányi *et al.* (2006, 2019) [11, 12]. The only reaction model for this reaction is ALICE-2017, which clearly overestimates the expected compound peak.

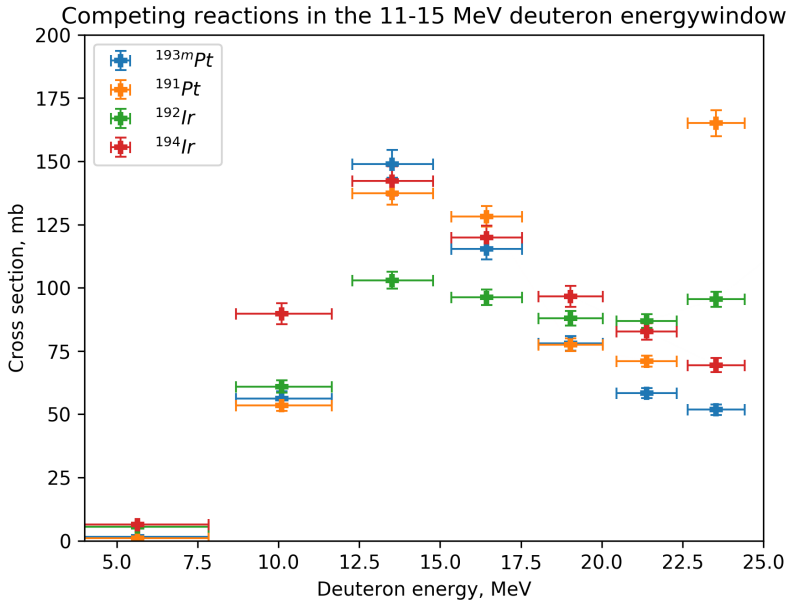

Figure 5.12: The competing processes which were measured in the deuteron window where the production of ^{193m}Pt is large, in this work: ^{191}Pt, ^{193m}Pt, ^{192}Ir ^{194}Ir.

5.2 The deuteron energy window of ^{193m}Pt

Figure 5.4 represents the excitation function for ^{193m}Pt. From this figure, the energy window yielding the highest cross sections is between 11-18 MeV. In the energy window from 11-18 Mev, the competing (measured) reactions are from ^{191}Ir(d,2n)^{191}Pt, ^{191}Ir(d,p)^{192}Ir and ^{193}Ir(d,p)^{194}Ir, shown in Figure 5.12. The energy window is based upon that the yield will be higher irradiating over a broader deuteron energy range. At the same time, contamination from other reaction channels leading to platinum are not desired. Unfortunately, the ^{191}Pt curve overlaps with ^{193m}Pt, but from the ^{191}Ir(d,2n) reaction. If an enriched target of ^{193}Ir is used, the radiopurity and specific activity of ^{193m}Pt can be improved, and the production of ^{191}Pt and ^{192}Ir can be remarkably reduced. In addition, production from stable ^{192}Pt will be reduced. Production of the stable/long-lived platinum contaminants ^{193,194}Pt (respectively) will also be produced. The main concern is the production of the ground state of ^{193}Pt, which was not possible to measure using this method due to its lack of gamma-rays. The stable/long-lived platinum contaminants will reduce the specific activity of the final product. Both ^{192}Ir and ^{194}Ir decays to stable ^{192}Pt and ^{194}Pt, so to reduce further increase of stable platinum contaminants, separation should take place shortly after end of beam (this accounts for ^{194}Ir in particular, with a half-life of 19.28 h).

5.3 Reaction cross sections from the monitor foils

The importance of increasing the state of deuteron nuclear reaction data is important, in particular for the monitor reactions. Currently, the number of datasets used in the proton induced monitor reactions from the recommended IAEA database [49] are much larger. For instance the reaction ^{nat}Cu(p,x)^{63}Zn is calculated based on a factor of 3.7 times more experimental datasets than ^{nat}Cu(d,x)^{63}Zn. More experimental data will improve the monitor cross sections, yielding more precise beam currents and finally better cross section results. The ^{nat}Cu(d,x)^{63}Zn reaction was a good example of this in this work. If the beam current relied solely upon this monitor reaction, all the measured cross sections using the wrong beam current would have resulted systematically wrong.

From ^{nat}Fe, there is currently only one monitor reaction; ^{nat}Fe(d,x)^{56}Co. Based on the characteristics of a good monitor reaction described in section 4.3, both ^{57,58}Co seem to be good candidates; independent and strong gamma-lines, sufficient half-life for ideally multiple measurements over time (which is a clear benefit in these types of experiments, where the end of beam activity is based upon multiple measurements of the same products over time), not contaminated by typical background radiation, highly fed reactions and not subject to feeding. In addition, cobalt from ^{nat}Fecannot be produced via secondary neutrons following deuteron breakup. ^{nat}Ni(d,x)^{54}Mn,^{57}Co and ^{nat}Cu(d,x)^{64}Cu are strongly fed channels with independent and strong gamma-lines. These proposed monitor reactions from ^{nat}Niand ^{nat}Cucan however be produced from secondary neutrons and/or subject to decay-feeding.

The excitation functions and a description of each reaction observed in the monitor foils are represented in Appendix E.

5.3.1 ^{nat}Fe(d,x)

Natural iron contains four stable nuclides, ^{54}Fe (5.845%), ^{56}Fe (1.754%), ^{57}Fe (2.119%) and ^{58}Fe (0.282%). The measured cross sections are represented in Table D.2. Since there were only three iron foils in the target stack located within the three first compartments, high-energy measurements between 24.8 and 29.6 MeV are reported. Due to the high deuteron beam energy, many of the reported cross sections are on the pre-equilibrium tail where the amount of nuclear data is less. In this deuteron energy region, it is clear that the two competing processes with the highest cross sections are cobalt-radionuclide (except ^{58}Co) (d,xn) reactions and manganese-radionuclide (d,xn2p) reactions. ^{53}Fe was not observed.
This thesis reports the first experimental measurement of ^{nat}Fe(d,x)^{48}V, ^{51}Cr

(both cumulative).

5.3.2 ^{nat}Ni(d,x)

In natural nickel, there are five stable nuclides (^{58}Ni (68.007%), ^{60}Ni (26.223%), ^{61}Ni (1.1399%), ^{62}Ni (3.6346%) and ^{64}Ni (0.9255%)). The results are therefore a variety of reactions which can take place. The measured cross sections are represented in Table D.3. It is clear that decay channels leading to products of cobalt (d,2pxn reactions) are favoured.

This thesis reports the first measurement of ^{nat}Ni(d,x)^{56,57,58g,58m}Co (independent) using the subtraction method (Equation 4.14), in addition to ^{53}Fe (cumulative).

5.3.3 ^{nat}Cu(d,x)

From natural copper, there are two stable nuclides (^{63}Cu (69.15%) and ^{65}Cu (30.85%)). The measured cross sections are listed in Table D.4. The products with highest cross sections are the monitor reactions ^{62,63,65}Zn and ^{64}Cu. From this target, there are not a large variety of possible products, mainly because of the many stable Ni-nuclides (produced via (d,nxα)) and Fe-nuclides (produced via (d, nx2α)). In addition only one radionuclide of cobalt was observed (which can be produced via (d,xnpα)), and neither of the radionuclides from manganese was observed (which can be produced via (d,xnp2α)). No single measurement of ^{61}Co or ^{65}Ni was observed independently.

Chapter 6

Summary and outlook

The thesis experiment took place in February 2019 at the Lawrence Berkeley National Laboratory's 88-Inch Cyclotron. The stacked target activation method was used to measure cross sections at multiple energies using an incident 33 MeV deuteron beam on a stack of thin iridium targets and monitor foils. This experiment is primarily part of a larger campaign to yield precise cross section measurements for potential medical radionuclide production. A set of cross section measurements for ^{nat}Ir(d,x) reactions are reported. In addition to deuteron induced products on iridium, the additional products from the monitor foils are reported, yielding a total of 42 reported cross section measurements (excluding the monitor reactions). A special emphasis was directed to the production of ^{193}Ir(d,2n)^{193m}Pt, and the energy window which maximises the production of ^{193m}Pt, and minimizes the production of stable ^{192,193,194}Pt which lack the therapeutic value of ^{193m}Pt, and will contribute to platinum-toxicity, as well as reduce the specific activity of ^{193m}Pt.

From the measurement of the compound peak of the ^{193}Ir(d,2n)^{193m}Pt reaction, along with experimental data and reaction model, the energy window which optimizes the production is from 11-18 MeV. One of the main observations was that ^{191}Ir(d,2n)^{191}Pt is the major contaminant in this energy region, but the use of an enriched ^{193}Ir target would reduce that reaction channel significantly. In the same deuteron energy window, ^{nat}Ir(d,x)^{192,194}Ir also competes. They both decay to stable platinum nuclides, so the Ir/Pt separation should take place before they contribute as additional contaminants. (in particular ^{194}Ir has a short half-life of 19.28 hours).

Regarding the measured cross section of ^{nat}Ir(d,x)^{189}Ir, with beta-feeding from ^{189}Pt, the cumulative cross section of both was smaller than the independent cross section of ^{189}Pt. Since ^{189}Pt feeds into ^{189}Ir, the measured cumulative cross section should have been higher. This puzzling result was also seen in previous experimental data. Those results cannot be correct and we have not yet man-

aged to identify a source of this error. So this should be further investigated.

There were no complications during the irradiation of the target stack. However, in order to observe additional long-lived activities, longer counts would have been necessary. This applied for ^{191}Os in particular, but also other long-lived products where the counting statistics were poor.

The variance minimization with 2% increase in the beam energy and 4.25% increase in the target densities was performed to improve the energy assignments of the foils in the stack. For the monitor reactions, ^{nat}Fe(d,x)^{56}Co, ^{nat}Ni(d,x)^{56,58,61}Cu and ^{nat}Cu(d,x)^{62,63,65}Zn, proved to reproduce the recommended monitor reaction data within uncertainties, except ^{nat}Cu(d,x)^{63}Zn which did not agree with the recommended cross sections from the IAEA database on the high energy pre-equilibrium tail of the excitation function. A deuteron beam energy reduction of 4–7% would have been necessary to agree within uncertainties. The previous experimental data, however, agreed with the data reported here. Therefore, data from this thesis will contribute to an improvement of the monitor cross section for this reaction, resulting in updated recommended values in the IAEA database. This particular reaction proves the importance of more data, in particular for monitor reactions, where the analysis relies upon a well characterized cross section.

The cross section measurements were compared to the nuclear reaction models TALYS-1.9, TENDL-2019, ALICE-2017, CoH-3.5.3 and EMPIRE-3.2.3, where the default parameters were used, with the exception of reaction modelling from ^{193}Ir-target using CoH-3.5.3, where the parameter *tweakSD* was set to 0.25 to adjust the effective single particle state density. This was a large change to the single particle state-density, and not physically realistic. The current version of CoH is not optimized for this reaction, and in general in the A=190 region. Regarding the nuclear reaction codes, there were disagreements between the location, shape and magnitude of the compound peak and pre-equilibrium tail is present in the deuteron energy window.

6.1 Outlook

The research on using ^{193m}Pt in therapy is in the early stages for clinical applications. This thesis work has contributed to better determine the deuteron energy-window which gives the highest purity without other Platinum contaminants. Further research will focus on thick target irradiation to produce quantities for research on the chemical separation and labelling chemical labelling to cisplatin. The reaction route ^{nat}Ir(d,x)^{193m}Pt measured a maximum of 233 mb at 12.6 MeV by Tárkányi *et al.* (2006) [11]. In comparison to the other potential

route ^{192}Os(α,3n)^{193m}Pt, the maximum measured cross section is approximately 7 times smaller. A calculation of the thick target yield using an enriched ^{193}Ir target would be of interest to see whether it is worth to go through to difficult production using osmium as target, or if this route can produce sufficient yield for clinical purposes. In addition, an analysis on the Auger spectrum is planned in the near future to accurately know the impacts on the dosimetry for ^{193m}Pt.

It is important to use the occasion to clarify that targeted radionuclide therapy is not a potential replacement of other methods. The diversity of methods and even the combination of multiple methods give opportunities for new and better diagnosis tools and treatment that improves chances of early diagnosis and survival. For instance, PET/CT or PET/MRI yields high resolution images with benefits from the metabolic imaging from PET [1]. In this thesis, the combination of the chemotherapeutic drug cisplatin labelled with the auger emitter ^{193m}Pt is believed to streamline the production and avoid platinum toxicity, which is one of the major issues with non-radioactive cisplatin [3, p. 493].

Appendix A

Error propagation

The uncertainty approach in this work is summarized in this appendix.

Uncertainty in statistics refers to the standard deviation of the data, which gives a quantitave value of of the spread in the data from the mean value:

$$\sigma = \sqrt{\frac{1}{N}\sum_{i=1}^{N}(x_i - \overline{x})^2} \tag{A.1}$$

where N is the number of measurements, x_i is a measurement and $\overline{x}$ is the average over all measurements. The standard deviation is the square root of the variance, σ^2.

In regression, χ^2 is a measure of the goodness of fit, which is weighted by the uncertainties on each measurement point:

$$\chi^2 = \sum_{i}^{n}\left(\frac{y_i - \overline{y}}{\sigma_i}\right)^2 \tag{A.2}$$

where $\overline{y}$ is the mean value of y and σ_i is the error in y_i. The reduced χ^2 is defined as the χ^2 per degree of freedom [103, p. 182, 183]:

$$\chi^2_\nu = \frac{\chi^2}{\nu} \tag{A.3}$$

where ν is the degrees of freedom equal to the number of observations minus the number of fitted parameters. A value close to 1, within uncertainties, the observations are in accordance with the fit. Large values or low values can indicate that the fit is inconsistent with the data, or that the uncertainties have been

overestimated, respectively.

A function f with input x, a set of parameters $\boldsymbol{\beta} = \beta_1, \beta_2, ..., \beta_n$ and output y can be written on the following form:

$$y = f(x, \boldsymbol{\beta}) \tag{A.4}$$

The uncertainty in y is dependent on the input x, as well as the correlations in the model parameters, β. The matrix expression for error propagation is [1]:

$$\sigma_y^2 = \mathbf{J} \cdot \mathbf{V} \cdot \mathbf{J}^T \tag{A.5}$$

where σ_y^2 is the variance in y, $\mathbf{J}$ is the Jacobian matrix:

$$\mathbf{J} = \begin{bmatrix} \frac{\partial f}{\partial \beta_1} & \frac{\partial f}{\partial \beta_2} & \cdots & \frac{\partial f}{\partial \beta_n} \end{bmatrix} \tag{A.6}$$

and $\mathbf{V}$ is the covariance matrix:

$$\mathbf{V} = \begin{bmatrix} \sigma_0^2 & \sigma_{0,1} & \cdots & \sigma_{0,n} \\ \sigma_{1,0} & \sigma_1^2 & \cdots & \sigma_{1,n} \\ \vdots & \vdots & \ddots & \vdots \\ \sigma_{n,0} & \sigma_{n,1} & \cdots & \sigma_n^2 \end{bmatrix} \tag{A.7}$$

where $\sigma_{i,j} = \mathrm{Cov}[\beta_i, \beta_j]$, the covariance between parameters β_i and β_j. In the cases where the input parameters are uncorrelated, all non-diagonal elements in the variance-covariance matrix is equal to zero, and the expression for the variance simplifies to:

$$\sigma_y^2 = \sum_{i=1}^{n} \left(\frac{\partial f}{\partial \beta_i} \right)^2 \sigma_{\beta_i}^2 \tag{A.8}$$

In cases where the analytical partial derivatives of f are laborious to calculate, the numerical derivative may be used instead:

$$\frac{\partial f}{\partial \beta_i} \simeq \frac{f(x, \beta_i + \frac{\Delta \beta_i}{2}) - f(x, \beta_i - \frac{\Delta \beta_i}{2})}{\Delta \beta_i} \tag{A.9}$$

This approximation will converge to the analytical approach when $\Delta \beta_i$ is a small number, using $10^{-8} \cdot \beta_i$ in this work.

[1] A full derivation of the expression can be found in [104]

As an example, for a function $f = xy$, the variance can be expressed from Equation A.5, where

$$\mathbf{J} = \begin{bmatrix} y & x \end{bmatrix}$$

and

$$\mathbf{V} = \begin{bmatrix} \sigma_x^2 & \sigma_{x,y} \\ \sigma_{y,x} & \sigma_{y^2} \end{bmatrix}$$

$$\sigma_f^2 = x^2\sigma_y^2 + y^2\sigma_x^2 + 2xy\sigma_{x,y} \tag{A.10}$$

If we multiply each term so that we can factor out f^2 $(= x^2y^2)$, the variance in f can be expressed as:

$$\sigma_f^2 = f^2\Big(\frac{\sigma_x^2}{x^2} + \frac{\sigma_y^2}{y^2} + \frac{2\sigma_{x,y}}{xy}\Big) \tag{A.11}$$

if the variables x and y are uncorrelated, the variance is further simplified, and more terms can be included easily. The simplified standard deviation of a function $f(\boldsymbol{\beta}) = \beta_1 \cdot \beta_2 \cdots \beta_n$ with uncorrelated variables is thus:

$$\sigma_f = |f|\sqrt{\Big(\frac{\sigma_{\beta_1}}{\beta_1}\Big)^2 + \Big(\frac{\sigma_{\beta_2}}{\beta_2}\Big)^2 + \cdots \Big(\frac{\sigma_{\beta_n}}{\beta_n}\Big)^2} \tag{A.12}$$

For a function $f(\boldsymbol{\beta}) = \beta_1 + \beta_2 + ... + \beta_n$, if all β_i are uncorrelated, the uncertainty is simply:

$$\sigma_f = \sqrt{\sigma_{\beta_1}^2 + \sigma_{\beta_2}^2 + ... + \sigma_{\beta_n}^2} \tag{A.13}$$

For calculation of the beam current, the weighted average beam current was applied. The weighted average of a series of uncorrelated measurements $x_i = x_1, x_2, ..., x_n$ is defined as [103, p. 37]:

$$\langle f \rangle = \frac{\sum_i w_i x_i}{\sum_i w_i} \tag{A.14}$$

where the weight w_i is the the inverse uncertainty squared:

$$w_i = \sigma_{x_i}^{-2} \tag{A.15}$$

For correlated measurements, the weighted average of a set of measurements is defined as:

$$\langle f \rangle = \frac{\sum_{i,j} x_j \left(\mathbf{V}_{ij}^{-1}\right)}{\sum_{i,j} \left(\mathbf{V}_{ij}^{-1}\right)} \tag{A.16}$$

where $i, j \in \boldsymbol{\beta}$, the parameters of $y = f(x, \boldsymbol{\beta})$. For the case of the weighted average beam current measurements, x_j represents the beam currents in a single compartment, and $\boldsymbol{\beta} \in A_0, \rho\Delta r, \lambda, \Delta t_{\text{irr}}, \langle\sigma(E)\rangle$. Accordingly, the propagated uncertainty must be calculated according to:

$$\sigma_{\langle f \rangle} = \sqrt{\frac{1}{\sum_{i,j} \left(\mathbf{V}_{ij}^{-1}\right)}} \tag{A.17}$$

For experimental measurements, the covariance between two correlated parameters β_i and β_j is given by the sandwich estimator:

$$\text{Cov}[\beta_i, \beta_j] = \sum_{i,j} \frac{\partial f}{\partial \beta_i} \cdot \sigma_{\beta_i} \cdot \text{Corr}[\beta_i, \beta_j] \cdot \sigma_{\beta_j} \cdot \frac{\partial f}{\partial \beta_j} \tag{A.18}$$

where $\text{Corr}[\beta_i, \beta_j]$ is the correlation coefficient between parameters β_i and β_j.

Appendix B

Gamma-ray analysis in FitzPeaks

The mathematical algorithm which Fitzpeaks [55] which uses the SAMPO algorithm for peak fitting [105]. In this algorithm, the peaks are assumed Gaussian, joined with an exponential tail on both sides of the peak, so that the function and first derivative are continuous. The SAMPO algorithm uses first and second order derivativations to determine peak locations, where the first derivative changes the sign at the centroid of the peak, and the second difference changes sign for each of the boundaries of each peak [54, p. 186]. This make the algorithm robust for detecting small peaks on low background[105]. To obtain the number of counts in a peak, the SAMPO code performs a linear least squares fit on all of the peaks, where the peak area, width and position are determined [54, p. 192] by minimizing χ^2. Fitzpeaks does the peak fitting on a parabolic background in each fit region [54, p. 192]. Uncertainty of the background is also included in the peak report. For each spectra, a report file is obtained, with information regarding counting time, live time, peak energy, centre channel, FWHM of the peak, significance, goodness of fit, peak area, relative uncertainty in peak area, and detection rate, as seen in Figure B.1.

be used for evaluation purposes

20-Mar-2019 17:26

P E A K F I T R E P O R T

Spectrum file Analysed: BH02262019_Ni10_15cm_room131.Chn
Sample Title : Ni10

Spectrum saved on 26-Feb-2019 at 13:18 Collected on 26-Feb-2019 at 13:11
Sample Taken on 26-Feb-2019 at 13:11 Decayed 0 Days, 0 mins.

Detector file number used: 7
Energy Calibration Performed on 8-Mar-2019 at 12:07
Peak Shape Calibration Performed on 8-Mar-2019 at 12:08

Datetime: 26-Feb-2019 13:11
Live: 353.00
Mass: 1028
Shelf: 15
Detector: 7

Reported Activity values were rounded
FitzPeaks Version: 3.71 23rd January 2014

Peak Energy	Centre Channel	FW@HM (KeV)	Signif	Goodness of Fit	Peak Area	% Uncert.	Gammas per sec.	% Uncert.	2 Sigma Background
67.4	358.7	0.96	41.8	0.58	17910	1.8	5.0738e+01	1.8	3990
72.8	387.3	1.01	15.3	1.57	4376	6.2	1.2396e+01	6.2	3640
74.9	398.9	1.01	24.8	1.57	7806	3.6	2.2113e+01	3.6	3640
84.8	451.4	0.96	9.4	1.52	2712	11.5	7.6814e+00	11.5	3268
87.4	465.4	0.96	4.3	1.52	751	38.4	2.1282e+00	38.4	3268
283.2	1507.9	1.24	55.5	1.30	29747	1.4	8.4269e+01	1.4	4359
366.6	1952.3	1.29	3.6	1.26	303	53.4	8.5792e-01	53.4	2504
373.3	1987.9	1.32	18.5	0.72	3979	4.6	1.1273e+01	4.6	2300
511.2	2722.7	2.78	61.1	11.62	270343	0.7	7.6584e+02	0.7	3416
529.5	2819.9	1.48	6.2	0.82	525	16.1	1.4866e+00	16.1	508
588.9	3136.3	1.47	12.4	1.05	1382	6.4	3.9143e+00	6.4	335
656.3	3495.4	1.68	35.7	0.92	11703	1.8	3.3154e+01	1.8	319
811.0	4319.4	1.81	8.9	0.79	891	7.7	2.5242e+00	7.7	163
817.1	4351.7	1.82	5.3	0.79	324	15.9	9.1730e-01	15.9	163
841.5	4481.7	1.85	5.0	0.93	206	24.2	5.8267e-01	24.2	174
847.1	4511.9	1.85	10.6	0.93	1090	7.1	3.0871e+00	7.1	174
902.6	4807.6	1.95	3.5	0.88	98	42.6	2.7665e-01	42.6	145
909.0	4841.3	1.95	10.3	0.88	924	7.7	2.6162e+00	7.7	145
1038.0	5528.5	2.08	5.0	1.05	140	28.9	3.9697e-01	28.9	71
1099.9	5858.0	2.15	3.9	0.71	193	17.7	5.4793e-01	17.7	43
1116.1	5944.4	2.17	5.4	1.39	290	14.8	8.2193e-01	14.8	39
1133.1	6034.9	2.19	3.4	1.00	63	40.4	1.7864e-01	40.4	30
1185.6	6314.8	2.23	17.8	0.83	2778	3.5	7.8691e+00	3.5	24
1238.6	6597.2	2.32	7.9	0.89	551	8.7	1.5601e+00	8.7	25
1461.5	7784.2	2.58	3.5	0.62	56	38.0	1.5950e-01	38.0	10
1482.0	7893.5	2.60	5.7	0.65	279	12.7	7.9145e-01	12.7	11
1771.9	9437.7	2.94	3.5	0.49	89	27.7	2.5327e-01	27.7	10
2035.4	10841.3	3.25	3.3	0.61	44	51.6	1.2360e-01	51.6	5
2599.0	13843.1	3.91	4.0	0.36	82	33.3	2.3095e-01	33.3	1

Figure B.1: An example of a Peak Fit Report file of nickel foil number 10 (Ni10), obtained from FitzPeaks. The file contains the date and time which the spectrum was taken. These files list the live time (where the dead time is the real time minus the live time), the mass (a numerical code XXYY, representing the foil number XX and the foil's atomic number YY; here representing Ni10), shelf (representing the counting position from detector surface, in cm), and detector which is the ID number of the detector which was used. Peak energy was used for identification, peak area and uncertainty in peak area were used to calculate end of irradiation activities. Gammas per second was used as the count rate used in cases of background subtraction (subsection 4.1.1)

Appendix C

Tabulated nuclear and reaction data

This appendix contains tables with product nuclei, accepted decay data [43] used in calculating activities and reaction Q-values [68] for the product nuclei. In Table C.1, the decay data for the monitor reactions are listed, along with the deuteron energy range that they are useful in. For Tables C.2, C.3, C.4 and C.5 (iridium, iron, nickel and copper, respectively), the product nuclei, half-life, decay mode, and the gamma-lines and intensities used in the analysis from the Nudat-2.8 database [43]. In addition, reaction routes via emission of protons, neutrons and alpha-particles and the corresponding reaction Q-value which were taken from the NNDC Q-value Calculator [68]. For reaction routes, only those which are energetically accessible in this work are listed. This thesis work will be published. After publication, all material used to calculate the cross sections represented in this thesis will be made available.

Table C.1: The table shows an overview of the gamma-lines used to calculate monitor reaction activities in each foil at the end of beam. Nuclear data from: [64, 71, 72]

Monitor reaction	Half-life	E_γ (keV)	I(%)	Useful beam-energies (MeV)[49]
^{nat}Fe(d,x)^{56}Co	77.236 d	263.434	0.0220	10-50
		486.55	0.0540	
		733.514	0.191	
		787.743	0.311	
		846.770	99.9399	
		852.732	0.049	
		896.510	0.073	
		977.372	1.421	
		996.948	0.111	
		1037.843	14.05	
		1140.368	0.132	
		1159.944	0.094	
		1175.101	2.252	
		1198.888	0.049	
		1238.288	66.46	
		1335.40	0.1224	
		1360.212	4.283	
		1771.357	15.41	
		1963.741	0.707	
		2015.215	3.016	
		2034.791	7.77	
		2212.944	0.388	
		2276.131	0.118	
		2598.500	16.97	
^{nat}Ni(d,x)^{56}Co (cum)	77.236 d	787.743	0.3111	5-50
		846.770	99.9399	
		977.372	1.421	
		1175.101	2.252	
		1963.741	0.707	
		2015.215	3.016	
		2034.791	7.77	
^{nat}Ni(d,x)^{58}Co (cum)	70.86 d	810.7593	99.450	5-50
		863.951	0.686	
		1674.725	0.517	

$^{nat}Ni(d,x)^{61}Cu$	3.339 h	282.956	12.2	3-50
		373.050	2.1	
		529.169	0.38	
		588.605	1.17	
		625.605	0.040	
		656.008	10.8	
		816.692	0.31	
		841.211	0.21	
		902.294	0.083	
		1032.162	0.043	
		1073.465	0.033	
		1132.351	0.090	
		1185.234	3.7	
		1446.492	0.045	
$^{nat}Cu(d,x)^{62}Zn)$	9.193 h	40.85	25.5	15-50
		243.36	2.52	
		246.95	1.90	
		260.43	1.35	
		304.88	0.29	
		394.03	2.24	
		548.35	15.3	
		596.56	26.0	
		637.41	0.25	
$^{nat}Cu(d,x)^{63}Zn$	38.47 m	449.93	0.236	8-50
		669.62	8.2	
		962.06	6.5	
$^{nat}Cu(d,x)^{65}Zn$	243.93 d	1115.539	50.04	5-50

Table C.2: Products observed for reactions on Iridium foils. Iridium has two stable isotopes: ^{191}Ir (37.3%) and ^{193}Ir (62.7%). Nuclear data from: [4, 62, 98–102]

Nuclide level (keV)	Half-life	Decay mode	Reaction route	Q value (keV)	E_γ (keV)	I_γ (%)
^{188}Ir	41.5 h	$\epsilon = 100\%$	^{191}Ir(d,4np)	-24802.0	1209.80	6.9
(0.0)					1715.67	6.2
					2059.65	7.0
^{189}Ir	13.2 d	$\epsilon = 100\%$	^{191}Ir(d,4np)	-16626.0	233.5	0.30
(0.0)			^{193}Ir(d,5np)	-30596.0	245.1	6.0
^{190}Ir	11.78 d	$\epsilon = 100\%$	^{191}Ir(d,2np)	-10251.1	294.75	6.6
(0.0)			^{193}Ir(d,4np)	-24221.2	380.03	2.03
					1036.05	2.42
^{190m2}Ir	3.087 h	IT= 8.6%	^{191}Ir(d,2np)	-10627.5	361.2	86.72
(376.4)		= 91.4%	^{193}Ir(d,4np)	-24597.6	502.5	89.38
^{192}Ir	73.829 d	$\epsilon = 4.76\%$	^{191}Ir(d,p)	3973.55	201.3112	0.471
(0.0)		$\beta^- = 95.24\%$	^{193}Ir(d,2np)	-9996.6	374.4852	0.727
					416.4688	0.670
					468.06885	47.84
					489.06	0.438
					612.46215	5.34
					1061.49	0.0531
^{194}Ir	19.28 h	$\beta^- = 100\%$	^{194}Ir(d,p)	3842.22	293.541	2.5
(0.0)					938.69	0.60
					1468.91	0.19
^{194m2}Ir	171 d	$\beta^- = 100\%$	^{194}Ir(d,p)	-	482.6	7
(190+X)					562.4	35
					687.8	3.6
^{188}Pt	10.16 d	$\epsilon = 99.999974\%$	^{191}Pt(d,2n)	-26109.0	195.05	18.4
(0.0)		$\alpha = 2.6E-5\%$			381.43	7.4
^{189}Pt	10.87 h	$\epsilon = 100\%$	^{191}Ir(d,4n)	-19389.0	94.34	6.5
(0.0)					113.82	2.5
					243.50	5.9
					317.65	2.8
					721.38	7.9
^{191}Pt	2.802 d	$\epsilon = 100\%$	^{191}Ir(d,2n)	-4017.0	178.96	12.5
(0.0)			^{193}Ir(d,4n)	-17988.0	351.17	42.6
					409.44	100
					456.47	42
					538.87	181
					624.06	18.5
^{193m}Pt	4.33 d	IT= 100%	^{193}Ir(d,2n)	-3063.5	66.831	7.21
(149.783)					135.5	0.1145475

Table C.3: Products observed for reactions on Iron foils. Iron has four stable isotopes: ^{54}Fe (5.845%), ^{56}Fe (91.754%), ^{57}Fe (2.119%) and ^{58}Fe (0.282%). Nuclear data from: [71, 72, 106–113]

Nuclide level (keV)	Half-life	Decay mode	Reaction route	Q value (keV)	E_γ (keV)	I_γ (%)
^{48}V	15.9735 d	$\epsilon = 100\%$	^{54}Fe(d,2α)	-3490.9	944.130	7.870
(0.0)			^{56}Fe(d,2n2α)	-23986.1	983.525	99.98
			^{57}Fe(d,3n2α)	-31632.2	1312.106	98.2
^{51}Cr	27.704 d	$\epsilon = 100\%$	^{54}Fe(d,pα)	-1381.3	320.0824	9.910
(0.0)			^{56}Fe(d,2npα)	-21876.5		
			^{57}Fe(d,3npα)	-29522.6		
			^{58}Fe(d,4npα)	-39567.2		
^{52}Mn	5.591 d d	$\epsilon = 100\%$	^{54}Fe(d,α)	5163.6	346.02	0.980
(0.0)			^{54}Fe(d,2n2p)	-23132.1	744.233	90.0
			^{57}Fe(d,2nα)	-15331.6	848.18	3.32
			^{57}Fe(d,3nα)	-22977.7	935.544	94.5
					1246.278	4.21
					1333.649	5.07
					1434.092	100.0
^{54}Mn	312.20 d	$\epsilon = 100\%$	^{54}Fe(d,2p)	-2139.1	834.8480	99.9760
(0.0)			^{56}Fe(d,α)	5661.4		
			^{57}Fe(d,nα)	-1984.7		
			^{58}Fe(d,2nα)	-12029.3		
^{56}Mn	2.5789 h	$\beta^- = 100\%$	^{56}Fe(d,2p)	-5137.8	846.7638	98.86
(0.0)			^{57}Mn(d,n2p)	-12783.8	1810.726	26.9
			^{58}Fe(d,α)	5467.2	2113.092	14.2
^{59}Fe	44.490 d	$\beta^- = 100\%$	^{58}Fe(d,p)	4356.44	1099.245	56.5
(0.0)					1291.590	43.2
^{55}Co	17.53 h	$\epsilon = 100\%$	^{54}Fe(d,n)	2839.8	91.9	1.16
(0.0)			^{56}Fe(d,3n)	-17655.4	477.2	20.2
			^{57}Fe(d,4n)	-25301.5	803.7	1.87
					827.0	0.21
					931.1	75
					1316.6	7.1
					1370.0	2.9
					1408.5	16.9
					2177.6	0.29
					2872.4	0.118
					2938.9	0.057
^{57}Co	271.74 d	$\epsilon = 100\%$	^{56}Fe(d,n)	3802.9	122.06065	85.60
(0.0)			^{57}Fe(d,2n)	-3843.2	136.47356	10.68
			^{58}Fe(d,3n)	-13887.8		
^{58}Co	70.86 d	$\epsilon = 100\%$	^{57}Fe(d,n)	4729.7	810.7593	99.450
(0.0)			^{58}Fe(d,2n)	-5314.9		

Table C.4: Products observed for reactions on Nickel foils. Nickel has five stable isotopes: ^{58}Ni (68.077%), ^{60}Ni (26.223%), ^{61}Ni (1.1399%), ^{62}Ni (3.6346%) and ^{64}Ni (0.9255%). Nuclear data from: [71, 72, 74, 108, 109, 111–115]

Nuclide level (keV)	Half-life	Decay mode	Reaction route	Q value (keV)	E_γ (keV)	I_γ (%)
^{52}Mn	5.591 d	$\epsilon = 100\%$	^{58}Ni(d,2α)	-1235.6	744.233	90.0
(0.0)			^{60}Ni(d,2n2α)	-21622.6	935.544	94.5
			^{61}Ni(d,3n2α)	-29442.7	1246.278	4.21
					1434.092	100.0
^{54}Mn	312.20 d	$\epsilon = 100\%$	^{58}Ni(d,2pα)	-8538.3	834.848	99.9760
(0.0)			^{60}Ni(d,2α)	-629.6		
			^{61}Ni(d,n2α)	-8449.7		
			^{62}Ni(d,2n2α)	-19045.4		
^{59}Fe	44.490 d	$\beta^- = 100\%$	^{60}Ni(d,3p)	-12539.5	1291.590	43.2
(0.0)			^{61}Ni(d,n3p)	-20359.6		
			^{62}Ni(d,pα)	-2659.7		
			^{64}Ni(d,2npα)	-19154.9		
^{55}Co	17.53 h	$\epsilon = 100\%$	^{58}Ni(d,nα)	-3559.4	385.4	0.54
(0.0)			^{58}Ni(d,3n2p)	-31855.0	520.0	0.83
			^{60}Ni(d,3nα)	-23946.4	803.7	1.87
			^{61}Ni(d,4nα)	-31766.5	931.1	75
					1212.8	0.26
					1316.6	7.1
					1370.0	2.9
					2177.6	0.29
^{56}Co	77.236 d	$\epsilon = 100\%$	^{58}Ni(d,α)	6522.5	787.743	0.3111
(0.0)			^{61}Ni(d,2nα)	-13864.5	846.770	99.9399
			^{61}Ni(d,3nα)	-21684.6	977.372	1.421
			^{62}Ni(d,4nα)	-32280.4	1175.101	2.252
					1963.741	0.707
					2015.215	3.016
					2034.791	7.77
^{57}Co	271.74 d	$\epsilon = 100\%$	^{58}Ni(d,n2p)	-10396.7	122.06065	85.60
(0.0)			^{60}Ni(d,nα)	-2488.1	136.47365	10.68
			^{61}Ni(d,2nα)	-10308.2		
			^{62}Ni(d,3nα)	-20903.9		
^{58}Co	70.86 d	$\epsilon = 100\%$	^{58}Ni(d,2n)	-1823.8	810.7593	99.450
(0.0)			^{60}Ni(d,α)	6084.9	863.951	0.686
			^{61}Ni(d,nα)	-1735.3	1674.725	0.517
			^{62}Ni(d,2nα)	-12331.0		
			^{64}Ni(d,4nα)	-28826.2		
^{58m}Co	9.10 h	IT= 100%	^{58}Ni(d,2n)	-1848.7	-	-
(24.88921)			^{60}Ni(d,α)	6060.0		
			^{61}Ni(d,nα)	-1760.2		
			^{62}Ni(d,2nα)	-12355.9		
			^{64}Ni(d,4nα)	-28851.1		

^{60}Co	1925.28 d	$\beta^- = 100\%$	^{60}Ni(d,2p)	-4265.0	1173.228	99.85
(0.0)			^{61}Ni(d,n2p)	-12085.1	1332.492	99.9826
			^{62}Ni(d,α)	5614.8		
			^{64}Ni(d,2nα)	-10880.4		
^{56}Ni	6.075 d	$\epsilon = 100\%$	^{58}Ni(d,3np)	-24688.4	158.38	98.8
(0.0)					480.44	36.5
					749.95	49.5
					811.85	86.0
					1561.80	14.0
^{57}Ni	35.60 h	$\epsilon = 100\%$	^{58}Ni(d,2np)	-14440.8	1757.55	5.75
(0.0)			^{60}Ni(d,4np)	-34827.8	1919.52	12.3
					2804.20	0.098
^{65}Ni	2.51719 h	$\beta^- = 100\%$	^{64}Ni(d,p)	3873.51	366.27	4.81
(0.0)					1481.84	23.59
					1623.42	0.498
					1724.92	0.399
^{60}Cu	23.7 m	$\epsilon = 100\%$	^{60}Ni(d,2n)	-9134.9	467.3	3.52
(0.0)			^{61}Ni(2,3n)	-16955.0	497.9	1.67
			^{62}Ni(d,4n)	-27550.7	643.2	0.97
					952.4	2.73
					1035.2	3.70
					1110.5	1.06
					1293.7	1.85
					1791.6	45.4
					1861.6	4.8
					1936.9	2.20
					2061.0	0.79
					2158.9	3.34
					2403.3	0.77
					2687.9	0.44
					2746.1	1.06
^{64}Cu	12.701 h	$\epsilon = 61.5\%$	^{64}Ni(d,2n)	-4681.3	1345.77	0.475
		$\beta^- = 38.5\%$				

Table C.5: Products observed on for reactions on Copper foils. Copper has two stable isotopes: ^{63}Cu (69.15%) and ^{65}Cu (30.85%). Nuclear data from: [64, 74, 111, 114, 115]

Nuclide level (keV)	Half-life	Decay mode	Reaction route	Q value (keV)	E_γ (keV)	I_γ (%)
^{59}Fe	44.490 d	$\beta^- = 100\%$	^{63}Cu(d,2pα)	-8782.1	1099.245	56.5
(0.0)			^{65}Cu(d,2α)	1687.0	1291.590	43.2
^{60}Co	1925.28 d	$\beta^- = 100\%$	^{63}Cu(d,pα)	-507.6	1173.228	99.85
(0.0)			^{65}Cu(d,2npα)	-18334.1	1332.492	99.9826
^{65}Ni	2.51719 h	$\beta^- = 100\%$	^{65}Cu(d,2p)	-3580.2	1481.84	23.59
(0.0)						
^{61}Cu	3.339 h	$\epsilon = 100\%$	^{63}Cu(d,3np)	-21962.9	282.956	12.2
(0.0)			^{65}Cu(d,5np)	-39789.4	656.008	10.8
					1185.234	3.7
^{64}Cu	12.701 h	$\epsilon = 61.5\%$	^{63}Cu(d,p)	5691.54	1345.77	0.475
(0.0)		$\beta^- = 38.5$	^{65}Cu(d,2np)	-12135.0		

Appendix D

Tabulated cross sections

This appendix contains the tabulated measured cross sections obtained in this work. ^{nat}Ir(d,x)-reactions are tabulated in Table D.1. ^{nat}Fe(d,x)-reactions are tabulated in Table D.2, ^{nat}Ni(d,x)-reactions are tabulated in Table D.3 and ^{nat}Cu(d,x)-reactions are tabulated in Table D.4.

Table D.1: The measured cross sections for ^{nat}Ir(d,x) reactions. Subscript i indicates that the measurement is independent while subscript c indicates that the measurement is cumulative.

	Production cross sections (mb)									
$E_d(MeV)$	$30.03^{+0.67}_{-0.67}$	$28.40^{+0.80}_{-0.79}$	$26.03^{+0.82}_{-0.82}$	$23.54^{+0.88}_{-0.87}$	$21.38^{+0.94}_{-0.92}$	$19.03^{+1.00}_{-0.99}$	$16.43^{+1.11}_{-1.08}$	$13.51^{+1.28}_{-1.22}$	$10.09^{+1.55}_{-1.41}$	$5.63^{+2.21}_{-1.83}$
$^{188}Pt_i$	0.95 (0.13)	0.30 (0.09)	0.17 (0.05)	-	-	-	-	-	-	-
$^{189}Pt_i$	486.47 (21.86)	341.24 (16.64)	172.11 (8.03)	30.72 (1.48)	1.04 (0.07)	0.09 (0.02)	-	-	-	-
$^{191}Ir_i$	597.10 (16.55)	483.60 (13.79)	353.99 (9.67)	165.12 (5.15)	71.05 (2.19)	77.53 (2.57)	128.24 (4.03)	137.37 (4.42)	53.45 (3.23)	1.05 (0.06)
$^{193m}Pt_i$	48.11 (6.33)	46.78 (2.18)	55.68 (2.17)	51.79 (2.12)	58.31 (1.96)	77.98 (2.89)	115.33 (4.09)	148.98 (5.54)	56.18 (2.85)	1.55 (0.12)
$^{188}Ir_c$	1.37 (0.01)	0.47 (0.07)	0.34 (0.08)	-	-	-	-	-	-	-
$^{188m1+g}Ir_c$	0.42 (0.16)	0.17 (0.11)	0.17 (0.09)	-	-	-	-	-	-	-
$^{189}Ir_c$	334.77 (22.25)	235.95 (16.33)	84.03 (6.03)	16.81 (5.17)	-	-	-	-	-	-
$^{190m2}Ir_i$	8.40 (0.25)	4.69 (0.14)	2.67 (0.08)	1.09 (0.04)	0.44 (0.01)	0.17 (0.01)	0.07 (0.01)	-	-	-
$^{190}Ir_c$	86.65 (2.89)	62.80 (2.14)	44.26 (1.47)	27.29 (1.02)	18.73 (0.71)	14.02 (0.55)	12.40 (0.51)	8.26 (0.43)	-	-
$^{190m1+g}Ir_c$	85.92 (2.89)	62.39 (2.14)	44.03 (1.47)	27.19 (1.02)	18.69 (0.71)	14.01 (0.55)	12.39 (0.51)	8.26 (0.43)	-	-
$^{192}Ir_c$	183.35 (5.18)	147.35 (4.28)	120.82 (3.34)	95.47 (3.02)	86.86 (2.70)	87.91 (2.93)	96.17 (3.05)	103.00 (3.35)	60.91 (2.44)	5.54 (0.32)
$^{194m2}Ir_i$	-	-	0.74 (0.17)	0.72 (0.06)	0.65 (0.13)	0.60 (0.14)	0.50 (0.09)	-	-	-
$^{194}Ir_c$	50.94 (2.28)	51.41 (2.29)	61.39 (2.39)	69.45 (2.76)	82.71 (3.21)	96.64 (4.15)	119.84 (4.66)	142.26 (5.72)	89.76 (4.22)	6.35 (0.43)

Table D.2: The measured cross sections for ^{nat}Fe(d,x) reactions. Subscript i indicates that the measurement is independent while subscript c indicates that the measurement is cumulative.

Production cross sections (mb)			
$E_d(MeV)$	$29.57^{+0.67}_{-0.67}$	$27.25^{+0.73}_{-0.72}$	$24.80^{+0.77}_{-0.75}$
$^{58}Co_c$	1.50 (0.05)	1.62 (0.05)	2.05 (0.07)
$^{57}Co_i$	35.91 (1.06)	38.37 (1.13)	42.63 (1.27)
$^{55}Co_i$	27.15 (0.80)	20.44 (0.60)	13.82 (0.40)
$^{59}Fe_i$	0.16 (0.02)	0.15 (0.02)	0.18 (0.04)
$^{56}Mn_c$	22.14 (0.65)	23.86 (0.80)	22.91 (0.65)
$^{54}Mn_i$	23.58 (0.70)	24.18 (0.72)	26.12 (0.79)
$^{52}Mn_c$	16.00 (0.46)	5.48 (0.16)	0.91 (0.03)
$^{51}Cr_c$	7.54 (0.23)	7.86 (0.25)	8.51 (0.29)
$^{48}V_c$	0.12 (0.01)	0.09 (0.01)	0.07 (0.00)
Monitor reaction			
$^{56}Co_i$	115.74 (3.55)	143.76 (4.22)	183.75 (5.41)

Table D.3: The measured cross sections for ^{nat}Ni(d,x) reactions. Subscript i indicates that the measurement is independent while subscript c indicates that the measurement is cumulative.

	Production cross sections (mb)									
$E_d(MeV)$	$31.29^{+0.66}_{-0.66}$	$29.08^{+0.70}_{-0.69}$	$26.74^{+0.74}_{-0.73}$	$24.28^{+0.79}_{-0.77}$	$22.19^{+0.84}_{-0.83}$	$19.92^{+0.92}_{-90}$	$17.42^{+1.00}_{-0.97}$	$14.63^{+1.14}_{-1.08}$	$11.41^{+1.35}_{-1.25}$	$7.40^{+1.84}_{-1.55}$
$^{64}Cu_i$	-	-	-	-	-	5.78 (1.66)	-	13.69 (6.64)	7.99 (1.19)	4.17 (2.02)
$^{60}Cu_i$	-	-	27.51 (1.68)	35.38 (1.71)	42.90 (3.55)	54.43 (4.62)	50.61 (4.68)	41.09 (4.89)	12.76 (2.64)	-
$^{65}Ni_i$	-	-	0.51 (0.06)	0.61 (0.05)	1.21 (0.23)	1.35 (0.25)	1.35 (0.23)	1.83 (0.27)	2.23 (0.29)	2.61 (0.19)
$^{57}Ni_c$	71.67 (2.37)	58.38 (2.21)	41.16 (1.38)	25.85 (0.95)	14.79 (0.62)	7.66 (0.36)	4.22 (0.18)	2.61 (0.15)	0.65 (0.05)	-
$^{56}Ni_c$	0.18 (0.01)	0.10 (0.01)	0.06 (0.01)	-	-	-	-	-	-	-
$^{60}Co_c$	12.94 (0.48)	20.26 (2.23)	18.91 (1.24)	20.17 (1.44)	13.48 (0.77)	11.25 (0.95)	9.64 (0.95)	7.69 (1.52)	1.94 (0.51)	-
$^{58m}Co_i$	68.06 (1.92)	77.42 (2.20)	102.27 (2.79)	118.56 (3.70)	110.28 (3.40)	115.36 (3.86)	109.86 (3.46)	98.24 (3.19)	59.93 (2.38)	12.66 (0.69)
$^{58g}Co_i$	53.45 (8.36)	58.67 (9.72)	58.02 (10.71)	72.68 (10.59)	99.10 (10.52)	113.57 (11.36)	112.78 (10.98)	99.08 (9.48)	64.66 (7.30)	11.36 (3.74)
$^{57}Co_c$	402.12 (11.70)	362.58 (10.85)	315.94 (9.06)	240.63 (7.74)	158.92 (5.17)	84.14 (3.08)	36.78 (1.23)	20.01 (0.75)	5.03 (0.23)	1.29 (0.29)
$^{57}Co_i$	330.46 (11.94)	304.20 (11.08)	274.78 (9.16)	214.79 (7.79)	144.12 (5.21)	76.48 (3.10)	32.56 (1.25)	17.40 (0.77)	4.38 (0.24)	1.29 (0.29)
$^{56}Co_i$	18.97 (0.56)	14.38 (0.46)	10.33 (0.31)	8.88 (0.30)	7.40 (0.25)	9.06 (0.33)	12.43 (0.41)	20.30 (0.69)	30.91 (1.24)	26.89 (1.50)
$^{55}Co_c$	14.19 (0.48)	17.59 (0.59)	20.47 (0.63)	23.50 (0.81)	23.03 (0.82)	19.13 (0.72)	13.11 (0.47)	7.57 (0.30)	0.71 (0.04)	0.18 (0.03)
$^{59}Fe_c$	0.24 (0.03)	-	0.15 (0.09)	-	0.11 (0.03)	-	-	-	-	-
$^{54}Mn_i$	21.17 (0.64)	15.11 (0.74)	9.55 (0.35)	5.42 (0.29)	1.23 (0.08)	0.76 (0.17)	-	-	-	-
$^{52}Mn_c$	3.22 (0.09)	3.17 (0.10)	2.56 (0.07)	1.83 (0.06)	1.19 (0.04)	0.57 (0.02)	0.13 (0.01)	0.05 (0.02)	-	-
					Monitor reactions					
$^{56}Co_c$	18.39 (1.02)	14.16 (2.10)	10.08 (1.12)	8.83 (0.27)	7.67 (0.24)	9.57 (0.31)	13.22 (0.41)	19.73 (0.60)	31.65 (0.91)	27.78 (0.96)
$^{58}Co_c$	116.66 (18.54)	133.05 (22.35)	155.58 (29.03)	190.24 (28.10)	217.14 (23.76)	241.76 (24.98)	236.83 (23.97)	191.83 (18.91)	127.59 (14.39)	24.81 (8.13)
$^{61}Cu_i$	14.46 (1.55)	14.87 (1.58)	14.73 (0.96)	14.60 (0.96)	14.96 (1.40)	16.24 (1.46)	19.13 (1.73)	24.96 (2.09)	37.82 (2.60)	65.82 (3.61)

Table D.4: The measured cross sections for ^{nat}Cu(d,x) reactions. Subscript i indicates that the measurement is independent while subscript c indicates that the measurement is cumulative.

	Production cross sections (mb)									
$E_d(MeV)$	$30.03^{+0.67}_{-0.67}$	$27.74^{+0.72}_{-0.71}$	$25.32^{+0.77}_{-0.76}$	$22.77^{+0.83}_{-0.82}$	$20.57^{+0.89}_{-0.87}$	$18.14^{+0.97}_{-0.95}$	$15.43^{+1.08}_{-1.04}$	$12.34^{+2.27}_{-1.20}$	$8.68^{+1.62}_{-1.43}$	$3.94^{+2.25}_{-2.22}$
$^{64}Cu_i$	170.76 (7.76)	153.78 (8.20)	132.56 (6.93)	121.54 (7.12)	106.07 (5.81)	95.92 (7.14)	123.79 (6.62)	156.65 (8.20)	209.38 (11.27)	73.54 (5.70)
$^{61}Cu_c$	4.54 (0.87)	2.07 (0.95)	1.18 (0.72)	-	-	-	-	-	-	-
$^{60}Co_c$	9.49 (0.52)	11.38 (0.51)	12.02 (0.51)	11.36 (0.43)	9.27 (0.41)	5.65 (0.26)	1.53 (0.12)	-	-	-
$^{59}Fe_c$	0.21 (0.03)	0.18 (0.02)	0.17 (0.02)	0.12 (0.01)	0.07 (0.01)	0.03 (0.01)	-	-	-	-
					Monitor reactions					
$^{62}Zn_i$	32.51 (1.24)	26.56 (1.09)	17.24 (0.83)	9.37 (0.43)	3.26 (0.17)	0.32 (0.13)	-	-	-	-
$^{63}Zn_i$	112.37 (9.38)	137.19 (11.41)	172.92 (13.89)	226.46 (16.14)	273.59 (19.27)	322.03 (22.76)	300.45 (21.21)	170.56 (12.23)	60.07 (3.19)	-
$^{65}Zn_i$	62.65 (1.90)	76.11 (2.47)	98.93 (2.87)	135.19 (4.09)	177.91 (4.97)	224.29 (8.55)	254.98 (7.25)	249.63 (7.83)	149.24 (8.45)	14.79 (5.49)

Appendix E

Excitation functions from the monitor foils

The excitation functions for ^{nat}Fe(d,x), ^{nat}Ni(d,x) and ^{nat}Cu(d,x) are listed in this appendix. The experimental cross section data found in the EXFOR database is from: [79–84, 87–96, 116–120]. The production of radionuclides in each target is also described below. Gamma-lines and Q-values are listed in Tables C.3, C.4 and C.5 from iron, nickel and copper, respectively.

^{nat}Fe(d,x)^{58}Co (cumulative)

The excitation function for the reaction ^{nat}Fe(d,x)$^{58m+g}$Co (isomer: $t_{1/2}$=9.10 h, IT=100%, ground state: $t_{1/2}$=70.86 d, ϵ=100% [71]) is represented in Figure E.1. The radionuclide can be produced via ^{57}Fe(d,n)^{58}Co (Q_{value}=4.7 MeV) and ^{58}Fe(d,2n)^{58}Co (Q_{value}=-5.3 MeV). The activities were calculated based on the strong gamma-line 810.7593 keV (99.450%), listed in Table C.3, emitted from the decay of the ground state. The gamma-line was not contaminated by background or other decay channels. The activities were fitted to a single decay curve with measurements taken approximately 90 hours after end of beam, when the isomer had decayed out (assuming complete decay after 10 half-lives). In the excitation function in Figure E.1, the single compound peak is caused by the two possible reactions via ^{57}Fe(d,n) and ^{58}Fe(d,2n). The measurements in this work extends the pre-equilibrium tale from existing experimental data [80–82, 84, 117], and agrees well with measurement by Sudar *et al.* (1994). CoH-3.5.3, TALYS-1.9 and ALICE-2017 reproduce the shape of the experimental data but are off in magnitude. TENDL-2019 predicts the magnitude of the compound peak correctly. EMPIRE-3.2.3 models the pre-equilibrium tale the best.

^{nat}Fe(d,x)^{57}Co (independent)

The excitation function for the reaction ^{nat}Fe(d,x)^{57}Co ($t_{1/2}$=271.74 d, ϵ=100% [113]) is represented in Figure E.2. The activities were calculated based on strong gamma-lines, listed in Table C.3, with good counting statistics. The calculated activities were fitted to a single-step decay fit. The measured data in this work is in good agreement with the experimental data [80–82, 84, 117]. ALICE-2017 does the best job peak shape and position wise, but the pre-equilibrium tale is overestimated. None of the codes performs well on the tale, but EMPIRE-3.2.3's predictive power is good from approximately 17 MeV, but clearly fails to model the compound peak. ALICE-2017 agrees with the location of the compound peak of the experimental data.

^{nat}Fe(d,x)^{55}Co (independent)

The excitation function for the reaction ^{nat}Fe(d,x)^{55}Co ($t_{1/2}$=17.53 h, ϵ=100% [112]) is represented in Figure E.3. The gamma-lines 91.9 keV, 477.2 keV and 1408.5 keV were weakly contaminated with background radiation, but the count rates were low in comparison. The end of beam activities was calculated using a single-step fit. The data obtained in this work belongs to the second compound peak, via ^{56}Fe(d,3n) and ^{57}Fe(d,4n). The data obtained in this work agrees with existing experimental data [81, 84, 95, 117]. TALYS-1.9, TENDL-2019 and COH-3.5.3 follows the curve well in the high energy region from 20 MeV. CoH-3.5.3 follows the shape best in the first compound peak.

^{nat}Fe(d,x)^{59}Fe (independent)

The excitation function for the reaction ^{nat}Fe(d,x)^{59}Fe ($t_{1/2}$=44.490 d, β^-=100%) is represented in Figure E.4. The activation was fairly low, but the gamma-lines were strongly fed and independent, and not-contaminated. The activities were fitted to a single-step decay fit. This product is only produced via ^{58}Fe(d,p) (the target has a low natural abundance), resulting in one compound peak. The data obtained in this work extends the pre-equilibrium tale from the data from by Khandaker *et al.* (2013), and the experimental data agree on the shape, even though the uncertainties are relatively large [81, 84]. TALYS-1.9 and TENDL-2019 follows the same shape as the experimental data but are off in magnitude. CoH-3.5.3, EMPIRE-3.2.3 and ALICE-2017 does not agree with the experimental data.

^{nat}Fe(d,x)^{56}Mn (cumulative)

The excitation function for the reaction ^{nat}Fe(d,x)^{56}Mn ($t_{1/2}$ = 2.5789 h, ϵ = 100%) is represented in Figure E.5. This is the first observed element in a decay chain and is therefore reported as cumulative. The gamma-lines used to calculate the end of beam activities were not contaminated by background radiation. However, the decay of ^{56}Co also populates 846.7638 keV (98.86%). Therefore, the calculated activities are based on measurements done in the first 11 hours after end of beam. The activities were estimated to a single-decay curve, with the relative uncertainties less than 0.9% for foils 1-3. There was no experimental data [81, 82] in this deuteron energy region, but the measured points extends the existing curves suggesting a compound peak at ca. 27 MeV. TALYS-1.9 TENDL-2019 predicts the same shape and values as the experimental data in energy region from 10-20 MeV. It is difficult to say whether the measured datapoints from this work is correct, but ALICE-2017 suggests peak location on the same location as this data.

^{nat}Fe(d,x)^{54}Mn (independent)

The excitation function for the reaction ^{nat}Fe(d,x)^{54}Mn ($t_{1/2}$=312.20 d, ϵ=100% [109]) is represented in Figure E.6. The intense gamma-line 834.8480 (99.9760%) was used to calculate the activities. The gamma-line was subject to weak feeding from background, but the count rates were low in comparison so this was ignored. The activities were fitted to a single decay fit. This data takes place on the pre-equilibrium tale of the first compound peak of the excitation function, right before it starts rising again. The experimental data [80–82, 84, 117] is not represented in this deuteron energy region, but the results looks reasonable, comparing to TENDL-2019, TALYS-1.9 and CoH-3.5.3 in this energy region.

^{nat}Fe(d,x)^{52}Mn (cumulative)

The excitation function for the reaction ^{nat}Fe(d,x)$^{52m+g}$Mn (isomer: $t_{1/2}$=21.1 m, IT=1.78%, ground state: $t_{1/2}$=5.591 d, ϵ=100% [108]) is represented in Figure E.7. This radionuclide is in addition the first observed element in a decay chain, but the parent radionuclide ^{52}Fe was not observed in this work. The gamma-lines used to calculate the activities were strong, and not contaminated. The activities were fitted to a single-decay curve since it was not possible to distinguish parent and isomer based on half-life and early counts. The data obtained in this work is located on the rise of the second compound peak, where the

^{54}Fe(d,2n2p) reaction channel opens. The experimental data [84, 117] agree in the first compound peak, and the data obtained in this work agree with Hermanne *et al.* (2000) in the second compound peak. TALYS-1.9 and TENDL-2019 agree with the experimental data in the first compound peak. EMPIRE-3.2.3 agree with the rise for the second compound peak up to approximately 30 MeV.

$^{\mathrm{nat}}$Fe(d,x)^{51}Cr (cumulative)

The excitation function for the reaction $^{\mathrm{nat}}$Fe(d,x)^{51}Cr ($t_{1/2}$=27.704 d, ϵ=100% [107]) is represented in Figure E.8. Reported as cumulative since it is the first observed element the a decay chain. The activities were calculated using a single independent gamma-line with no contamination. The activities were fitted to a single-decay curve. The threshold is at approximately 10 MeV, and the energetically possible reactions contribute to a "fat" compound peak. The data obtained in this work is located on the fall of this peak. There is no existing experimental data for this reaction in the EXFOR database. The reaction models agree on the shape of the excitation function, although there are disagreements in the magnitude.

$^{\mathrm{nat}}$Fe(d,x)^{48}V (cumulative)

The excitation function for the reaction $^{\mathrm{nat}}$Fe(d,x)^{48}V ($t_{1/2}$ = 15.9735 d, ϵ = 100%) is represented in Figure E.9. This is the first observed element in a decay chain and is therefore reported as cumulative. The end of beam activities were calculated from independent gamma-lines which were weakly contaminated with background radiation. The cross section can therefore appear as slightly larger. The activities were fitted to a single-decay curve. This reaction can be produced via a variety of reaction channels. The reaction is however weakly fed, and there is no existing experimental data for this reaction. The experimental data agree with TALYS-1.9, but the other reaction models suggests a higher magnitude.

$^{\mathrm{nat}}$Ni(d,x)^{64}Cu (independent)

The excitation function for the reaction $^{\mathrm{nat}}$Ni(d,x)^{64}Cu ($t_{1/2}$=12.701 h, ϵ=61.5%, β^-=38.5% [115]) is represented in Figure E.10. The activities were calculated based on the single weak gamma-line 1345.77 keV (0.475%), so the

counting statistics were poor, and the radionuclide was only observed in foils 6, 8-10. This resulted in large uncertainties in final cross sections. The compound peak is from the ^{64}Ni(d,2n). The measurements obtained in this work is within uncertainties in agreement with the existing experimental data [87, 89, 91]. The reaction model codes also agree with the experimental data on the shape and magnitude of the compound peak.

^{nat}Ir(d,x)^{60}Cu (independent)

The excitation function for the reaction ^{nat}Ni(d,x)^{60}Cu ($t_{1/2}$=23.7 m, ϵ=100% [114]) is represented in figure Figure E.11 The gamma-lines used to calculate activities were not background contaminated, but the strongest lines were however weakly fed by a few nuclei. Because of the short half-life of this isomer, and the low intensity from the other gamma-lines, this was not taken out of the analysis. Activities were fitted to a single-decay curve. This product is produced via multiple neutron emission, and the three contributing reactions within the energy threshold is contributes to one single "fat" compound peak. The data obtained in this work agree with existing experimental data [80, 83, 87]. Regarding the reaction models, the magnitude of the compound peak from the experimental data agree with TENDL-2019, TALYS-1.9 and CoH-3.5.3. The location of the compound peak seem to agree with ALICE-2017 which is off in magnitude. EMPIRE-3.2.3 seem to follow the same shape as the experimental data best.

^{nat}Ir(d,x)^{65}Ni (independent)

The excitation function for the reaction ^{nat}Ni(d,x)^{65}Ni ($t_{1/2}$=2.51719 h, β^-=100% [74]) is represented in Figure E.12. The gamma-lines used to calculate the activities were not background contaminated. Contamination from ^{57}Co and ^{59}Fe was present, but because the half-lives were much longer, activities measured after 20 hours were not used further in the analysis. The activities were fitted to a single-decay curve fit. This nuclide is produced via ^{64}Ni(d,p), which gives rise to one compound peak. The measurements obtained in this work agree with shape of the data from Avrigeanu *et al.* (2016), but the measured cross sections are slightly larger. In addition, the uncertainties are larger. The reactions model predicts the compound peak differently, but TALYS-2017 and TENDL-2019 predicts the shape like the experimental data but the magnitude and location is shifted towards low energies.

^{nat}Ni(d,x)^{57}Ni (cumulative)

The excitation function for the reaction ^{nat}Ni(d,x)^{57}Ni ($t_{1/2}$=35.60 h, ϵ=100% [113]) is represented in represented in Figure E.13. This radionuclide is the first observed element in a decay chain and is therefore reported as cumulative. The gamma-lines used to obtain activities are not background contaminated. However 1919.52 keV (12.3%) is shared between ^{60}Cu (23.7 m) [114], but since ^{60}Cu decay fast and is weakly fed, this was ignored. The activities were fitted to a single-decay curve fit. The radionuclide can be produced via ^{58}Ni(d,2np) and via ^{60}Ni(d,4np), and both reaction feed into a large compound peak. In addition, the ^{58}Ni(d,t) (Q_{value}=-6.0 MeV) reaction channel is possible, which seems like is weakly fed, due to the measured cross sections below 14 MeV. This data agrees with the experimental data [83, 87–89, 91], but the two highest energy points the values are above the experimental data. For the reaction models, TENDL-2019, TALYS-1.9 and CoH-3.5.3 follows the experimental data up in this energy region.

^{nat}Ni(d,x)^{56}Ni (cumulative)

The excitation function for the reaction ^{nat}Ni(d,x)^{56}Ni ($t_{1/2}$=6.075 d, ϵ=100% [72]) is represented in Figure E.14. The radionuclide is the first observed element in a decay chain and is therefore reported as cumulative. The gamma-lines used to calculate the end of beam activities were not contaminated. The activities were fitted to a single-decay curve. ^{56}Ni can be produced via ^{58}Ni(d,3np) (Q_{value}=-24.7 MeV). The cross sections obtained in this work is therefore in the threshold region. There was no existing experimental data in the EXFOR database for this reaction. The reaction modelling codes does not agree on where the threshold for the reaction is, but according to the Q-value, the threshold should be at approximately 25 MeV.

^{nat}Ni(d,x)^{60}Co (cumulative)

The excitation function for the reaction ^{nat}Ni(d,x)$^{60m+g}$Co (isomer: $t_{1/2}$=10.467 m, IT=99.75%, ground state: $t_{1/2}$=1925.28 d, β^-=100% [114]) is represented in Figure E.15 Due to the short half-life of the isomer, it was not possible to have precise measurements before the isomer had decayed out. In addition, this radionuclide is the first observed element in a decay chain. ^{60}Co was present in the background, and the gamma-lines used had to be background subtracted. This

lead to an additional uncertainty. The gamma-lines were intense, but because of the long half-life of the ground state, very long counts were necessary to reduce the statistical errors. For this particular radionuclide, the counts should have been much longer because of the long half-life. The measured activities in each foil were fitted to a single decay curve. There is a large spread in the experimental data [87–90]. This work agrees acceptably with the work done by Usman *et al.* (2016) and Avrigeneau *et al.* (2016). The reaction models TENDL-2019, TALYS-1.9, CoH-3.5.3 and EMPIRE-3.2.3 agree that there is a compound peak around which is formed due to the reaction channels (d,2np) (^{61}Ni) and (d,2n2p) (^{63}Ni). In addition, the codes seems to predict a small compound peak opening at ca. 5 MeV where the low energetic reactions feed in.

^{nat}Ni(d,x)^{58}Co and ^{58m}Co (independent)

The excitation function for the reaction ^{nat}Ni(d,x)^{58}Co is represented for both the isomer ($t_{1/2}$=9.10 h, IT=100%) in Figure E.16 and the groundstate ($t_{1/2}$=70.86 d, ϵ=100%) in Figure E.17 [71]. Independent measurements of both were made using the strong gamma-line 810.7593 keV along with two weaker gamma-lines, listed in Table C.4, from the decay of the groundstate. The strong gamma-line was not subject to background contamination or contamination. Since the isomer does not emit observable gamma-lines, the activities was measured using the gamma-lines from ^{58}Co in a two-step decay fit, where the parent activity and the daughter activity were optimized. Both the isomer and groundstate can be produced via multiple reaction routes from natural nickel.

No existing experimental data was found for ^{58m,58g}Co, independently. For ^{58m}Co, ALICE-2017 reproduce the shape of the measured cross sections in this work, but the magnitude is lower. For ^{58}Co, both TENDL-2019 and TALYS-1.9 reproduce the exxperimental data in this work. The cumulative (monitor) reaction can be seen in Figure E.18, where the feeding proportions of $^{58m/58g}$Co are visible. The summed cross sections agree well with the experimental data [87, 91, 92] (except from Takacs *et al.* (1997) [83]).

^{nat}Ni(d,x)^{57}Co (independent and cumulative)

The excitation function for ^{nat}Ni(d,x)^{57}Co ($t_{1/2}$=271.75 d, ϵ=100%) is represented in Figure E.19 (cumulative) and Figure E.20. ^{57}Co is subject to beta-feeding from ^{57}Ni ($t_{1/2}$=35.60 h) [113]. The two strong gamma-lines 122.06065 keV (85.60%) and 136.47365 keV (10.68%), listed in Table C.4, were used in the

analysis, and was not subject to feeding from other decay channels. 122.06065 keV was however present in some background spectra in cave 4C, but with count rates in the order of 10^3 it was ignored as it did not impact the result compared to other experimental data. The activity was calculated using a single-decay fit with the activity from end of beam activity from ^{57}Ni, with activities measured about 300 hours after end of beam. This radionuclide can be produced via a variety of routes directly, in addition to the indirect production of ^{57}Ni. The cumulative cross section agree with existing experimental data [80, 83, 87–92]. The spread in the data increases with higher energies. The reaction models agree internally on shape (not magnitude).

The reaction models does not agree on the location of the compound peak. The independent cross section was obtained by subtracting the cumulative cross section and the independent 57Ni cross section. The figure show that the contribution from 57Ni increases with energy, which can be a contribution to the large spread in the data over higher energies.

^{nat}Ni(d,x) (^{nat}Ni(d,x)^{56}Co (independent))

The independent cross section ^{56}Co ($t_{1/2}$=77.236 d, ϵ=100%. The radionuclide is subject to beta-feeding from ^{56}Ni ($t_{1/2}$=6.075 d) [72]) is represented in Figure E.21. The gamma-lines which were used to obtain the activities and gamma-lines where independent and not contaminated. The activities were fitted to a two-step decay function for the three first foils. The remaining foils were fitted to a single decay curve. The independent measurement and the cumulative measurement looks very much the same- does not have experimental data to compare to. Cumulative cross section shows that feeding component of 56Ni was very small. he high energitic points agrees very well with the reaction modelling codes TENDL-2019, TALYS-1.9 and CoH-3.5.3 after about 20 MeV. EMPIRE-3.2.3 seems to model the first compound peak better. From Figure E.22, the contribution from ^{56}Ni can be seen which is very low. The experimental data agrees well with the data measured in this work [80, 87–92].

^{nat}Ni(d,x)^{55}Co (cumulative)

The cumulative measurement of ^{55}Co ($t_{1/2}$=17.53 h, ϵ=100%) is represented in Figure E.23. It is the first observable element in a decay chain, and is therefore reported as cumulative. The gamma-lines which were not subject to background contamination or from other nuclei. Was fitted to a single decay curve. This radionuclide can be produced from a variety of ways, where all the reactions contribute to a broad compound peak. This reaction have well experimented

[80, 83, 87–92]. Regarding reaction modelling codes, EMPIRE-3.2.3 follows the shape of the measure point more or less consistently all the way, which is an impressive predicting power.

^{nat}Ni(d,x)^{59}Fe (cumulative)

The cumulative measurement of ^{59}Fe ($t_{1/2}$=44.490 d, β^-=100% [111]) is represented in Figure E.24. The first observed in a decay chain and is therefore reported as cumulative. The gamma-lines used were independent and not background contaminated, calculated to single step decay. The activation here is low, so this product was only observed in foil 1, 3 and 5. There is no existing experimental data for this radionuclide. CoH-3.5.3 agree with the data obtained in this work. The remaining reaction codes does not agree.

^{nat}Ni(d,x)^{54}Mn (independent)

^{54}Mn ($t_{1/2}$=312.20 d, ϵ=100% [109]). The activities were calculated based on the 834.848 keV (99.9760%) gamma-line which was independent but weakly background contaminated. Therefore, the three last measurements are not used in (foils 7,8,9) was not used because, because the foils were irradiated with deuterons under threshold for this reaction. This product can be produced via emission of alpha-particles, protons and neutrons (not all reaction routes are included). The cross section start to increase around 16 MeV, and multiple reactions feed into a broad compound peak. The data from this work aligned well with the experimental data [88–90, 92]. In addition, EMPIRE-3.2.3, TALYS-1.9, CoH-3.5.3, TENDL-2019 predicts the shape very well, and CoH-3.5.3 and EMPIRE-3.5.3 predicts the magnitude well too.

^{nat}Ni(d,x)^{52}Mn (cumulative)

The cumulative cross section for $^{52m+g}$Mn (isomer: $t_{1/2}$=21.1 m, IT=1.78%, ground state: $t_{1/2}$=5.591 d, ϵ=100% [108]) is represented in Figure E.26. In addition there possible feeding from ^{52}Fe [108]. The gamma-lines used to calculate activities are only present in isomer and the groundstate, and not background contaminated. Therefore, the measured activities were fitted to a single decay curve fit after the isomer had decayed out. This product nucleus can be produced via decay of multiple alpha-particles, protons and neutrons (not all possible reaction channels are included) and the results is a broad compound peak. This data

is in good agreement with the experimental data [88–90, 92]. None of the reaction models predicts the magnitude of the experimental data, but ALICE-2017 and EMPIRE-3.2.3 predicts the same shape as the experimental data.

^{nat}Cu(d,x)^{64}Cu (independent)

The independent measurement of ^{64}Cu ($t_{1/2}$=12.701 h, ϵ=61.5%, β^-=38.5% [74]) represented in Figure E.27. The gamma-line which was used to calculate the activities was not subject to background radiation and was not shared with other nuclei. The end of beam activity was calculated using a single-step decay. The intensity of the gamma-line was weak, but since the channel is heavily fed, the statistical uncertainty was relatively low, ranging from 3.7% to 6.7%. This radionuclide can be produced via ^{63}Cu(d,p) and ^{65}Cu(d,2np). Compared to existing experimental data [79, 80, 93, 94, 94, 96, 119, 120], the data obtained in this work agree well. ALICE-2017 and CoH-3.5.3 does a different approximation in comparison to TENDL-2019, TALYS-1.9 and EMPIRE-3.2.3, where EMPIRE-3.2-3 approximates the first compound peak like the experimental data.

^{nat}Cu(d,x)^{61}Cu (cumulative)

The cumulative measurement of ^{61}Cu ($t_{1/2}$=3.339 h, ϵ=100% [64]) is represented in Figure E.28. Three intense gamma-lines were used to calculate the activities, which were not contaminated by background radiation, nor by other nuclei. The activities were fitted to a single-decay curve. Because of the low activation in the foils, the relative uncertainty in the end of beam activities were large, being 19.1%, 45.9%, 61.0% in foils 1-3, which were the only ones which were activated. The cross section was reported as cumulative as this was the first observed element in the decay chain. The cross section starts to increase from ca. 22 MeV, which is where the ^{63}Cu(d,3np) opens. The rise of the compound peak aligns well with existing experimental data [95, 120]. CoH-3.5.3 agree very well with the previos experimental data, predicting the excitation function for the increasing experimental data. ALICE-2017, TALYS-1.9 and TENDL-2019 were also matching the experimental data for the measurements in the threshold region.

^{nat}Cu(d,x)^{60}Co (cumulative)

The cumulative cross section of $^{60m+g}$Co (isomer: 10.467 m, IT=99.75%, ground state: $t_{1/2}$=1925.28 d, β^-=100% [114]) is represented in Figure E.29. The gamma-lines used in this analysis was 1173.228 keV (99.85%) and 1332.492 keV (99.9826%). The cross section was reported as cumulative as there is possible feeding from the very long lived ^{60}Fe ($t_{1/2} = 2.62 \cdot 10^6$ y), but this was not observed. ^{60}Co is present in the background, and it was necessary to use background subtraction, which was a contributing factor to higher uncertainties in the number of counts. The measured activities in the foils were fitted to a single-decay curve. The relative uncertainty in the foils were between 2.1% and 7.2% in foils 1-7. The excitation function opens at ca. 10 MeV, and the first measured point in this work is at 11.41 MeV. The cross section increases to a compound peak when the next reaction channel opens. The cross sections measured in this work aligns well with existing experimental data [79, 93]. ALICE-2017 agrees with the experimental data on the shape of the compound peak. The other prediction models are off.

^{nat}Cu(d,x)^{59}Fe (cumulative)

The cumulative measurement of ^{59}Fe ($t_{1/2}$=44.490 d, β^-=100% [111]) is represented in Figure E.30. This is the first observed element in a decay chain, so reported as cumulative. The gamma-lines used in the analysis is listed in table, the two most intense gamma-lines 1099.245 keV (56.5%) and 1291.590 keV (43.2%) were used, which are not subject to background radiation. However, the former gamma-line was also present in ^{61}Cu, but with a large difference in half-life and intensity of the gamma-line, this was ignored. The activity was calculated using a single-step decay fit. The induced activities were low, so followingly, the statistical uncertainty from the number of counts were quite large, ranging from 6.4% to 22.1% in foils 1-6. This nucleus was the first observed element in a decay chain and is therefore cumulative, with the possible feeding from ^{59}Mn ($t_{1/2}$=4.59 s, which can contribute via reaction ^{65}Cu(d,2pdα) (Q_{value}=-28.7 MeV), as the cross section increases around 30 MeV. ^{59}Fe can be produced directly via ^{63}Cu(d,2pα) (Q_{value}=-8.8 MeV) or via ^{65}Cu(d,2α) (Q_{value}=1.7 MeV). Figure E.30 shows the excitation function for the reaction. The reaction channel opens at ca. 14 MeV, and the first measured point in this work is at 18 MeV (0.03 mb). In comparison to existing data [79, 93], the data from this work agrees with the data from Khandaker *et al.* (2014), and for Tacaks *et al.* (2006), the values are lower, but mostly within uncertainty. In comparison to reaction models, CoH-3.5.3 does a very good job magnitude and shape wise, TENDL-2019 and TALYS-1.9 approximates the same shape as the experimental data. EMPIRE-3.2.3 and ALICE-2017 approximates the peak in a different way which looks unphysical.

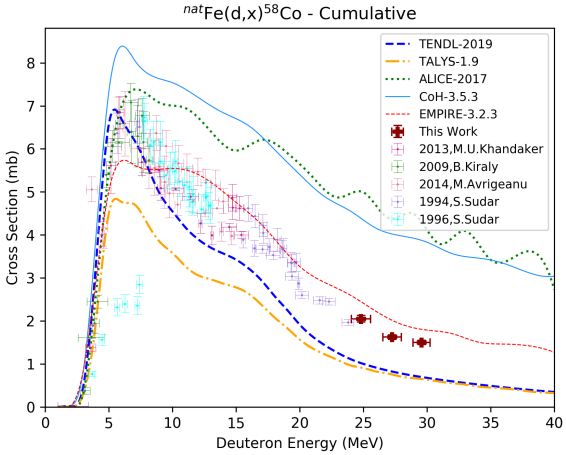

Figure E.1: The excitation function for ^{nat}Fe(d,x)^{58}Co.

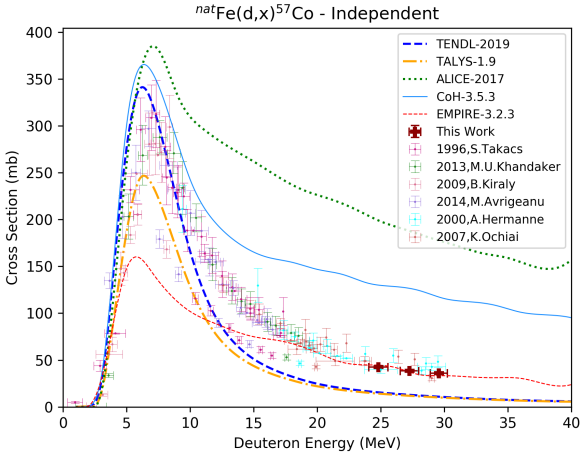

Figure E.2: The excitation function for ^{nat}Fe(d,x)^{57}Co.

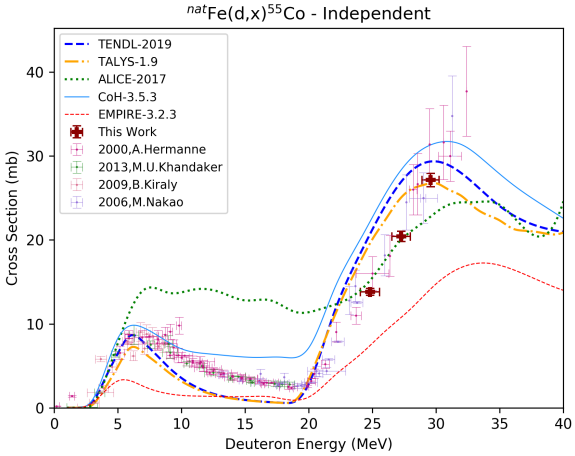

Figure E.3: The excitation function for ^{nat}Fe(d,x)^{55}Co.

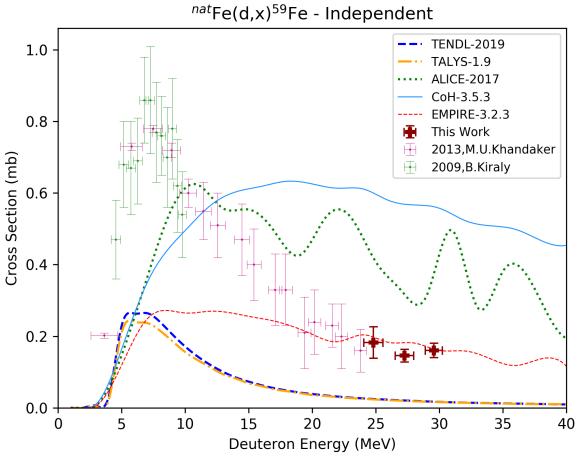

Figure E.4: The excitation function for ^{nat}Fe(d,x)^{59}Fe.

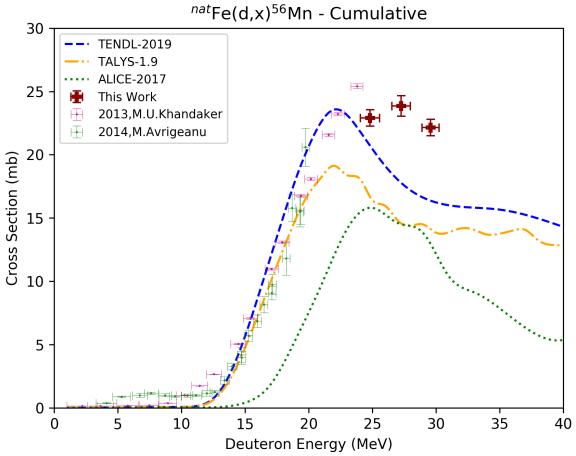

Figure E.5: The excitation function for $^{\text{nat}}$Fe(d,x)^{56}Mn.

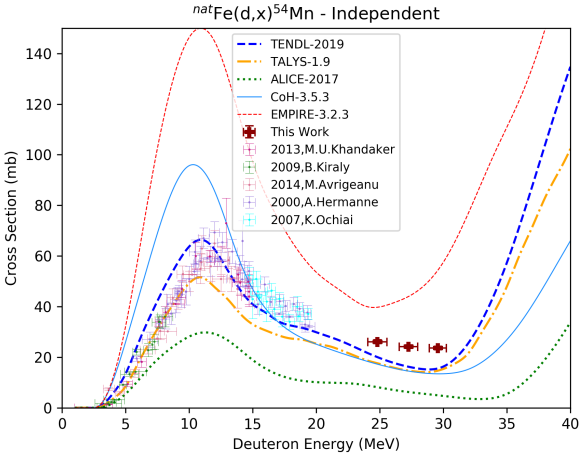

Figure E.6: The excitation function for $^{\text{nat}}$Fe(d,x)^{54}Mn.

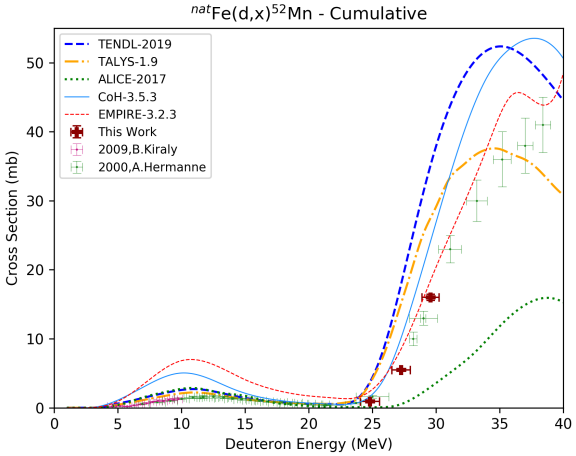

Figure E.7: The excitation function for $^{\text{nat}}$Fe(d,x)^{52}Mn.

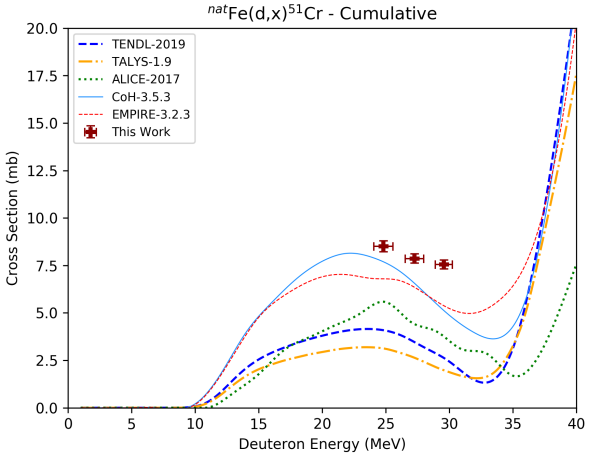

Figure E.8: The excitation function for $^{\text{nat}}$Fe(d,x)^{51}Cr.

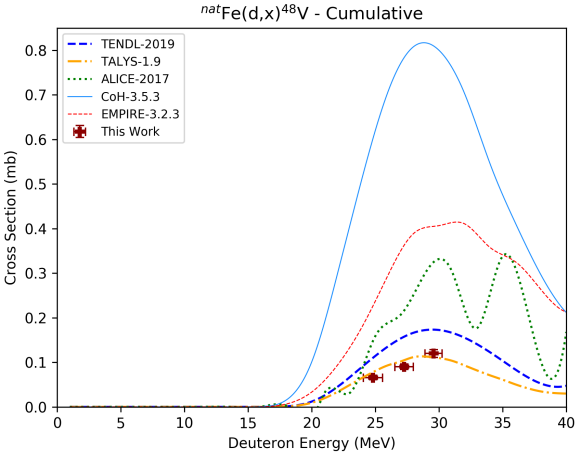

Figure E.9: The excitation function for $^{\text{nat}}$Fe(d,x)^{48}V.

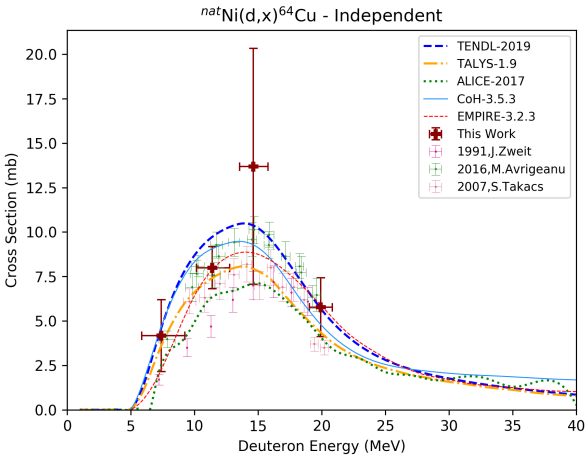

Figure E.10: The excitation function for ^{nat}Ni(d,x)^{64}Cu.

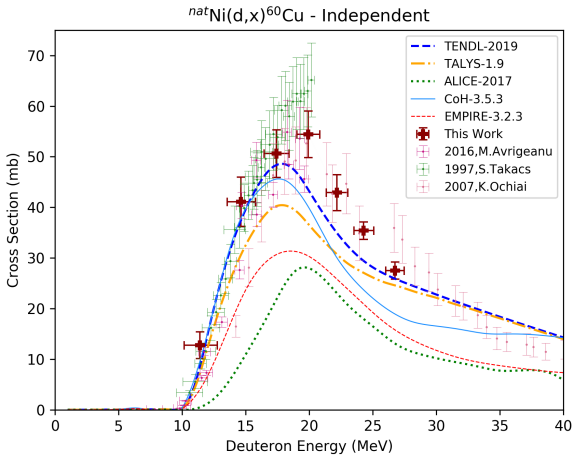

Figure E.11: The excitation function for ^{nat}Ni(d,x)^{60}Cu.

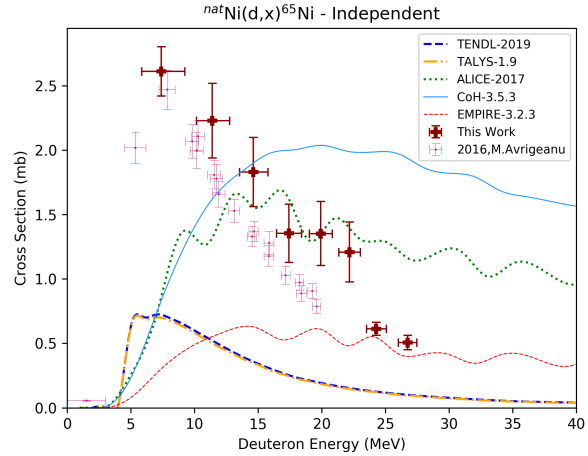

Figure E.12: The excitation function for ^{nat}Ni(d,x)^{65}Ni.

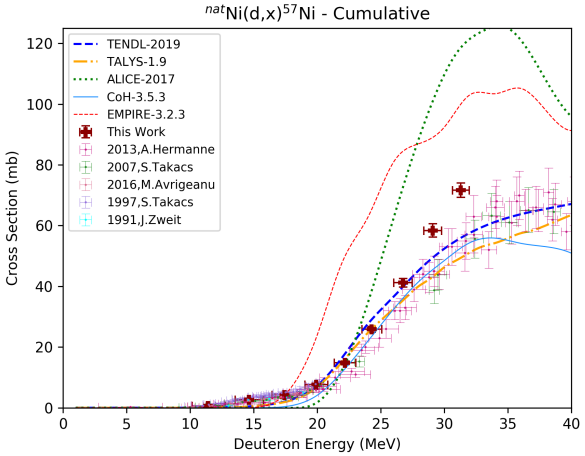

Figure E.13: The excitation function for ^{nat}Ni(d,x)^{57}Ni.

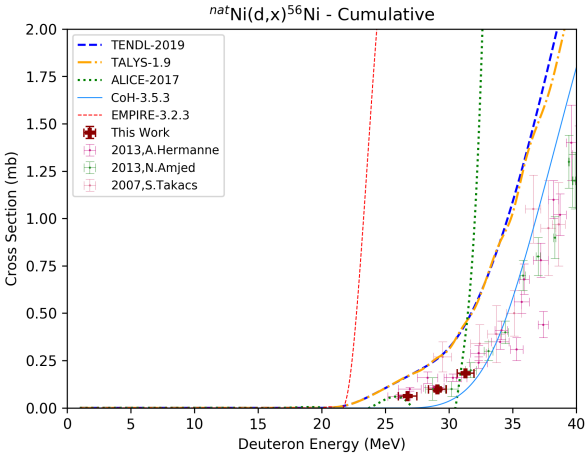

Figure E.14: The excitation function for ^{nat}Ni(d,x)^{56}Ni.

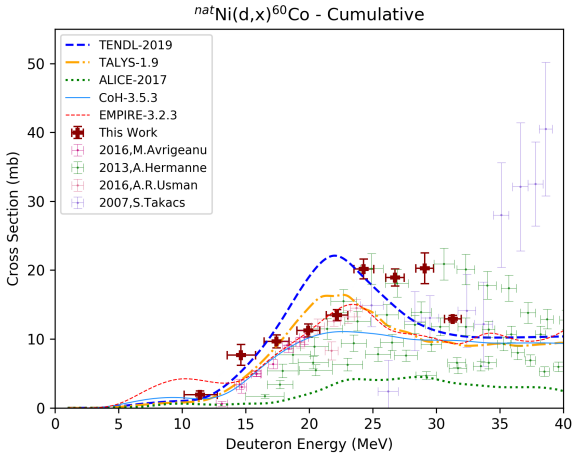

Figure E.15: The excitation function for ^{nat}Ni(d,x)^{60}Co.

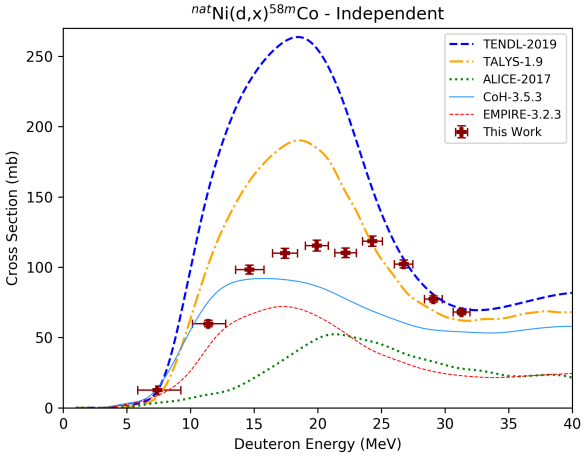

Figure E.16: The excitation function for ^{nat}Ni(d,x)^{58m}Co (independent).

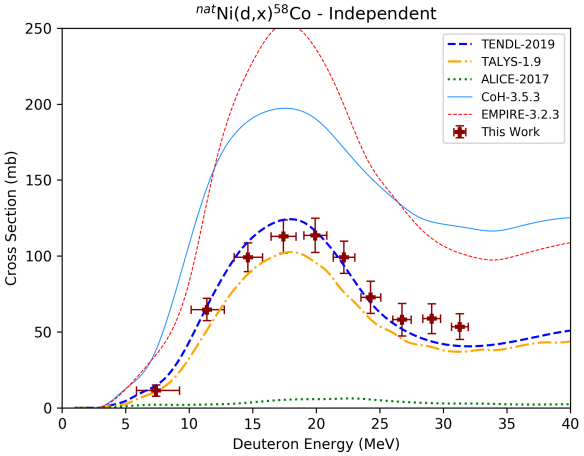

Figure E.17: The excitation function for ^{nat}Ni(d,x)^{58}Co (independent).

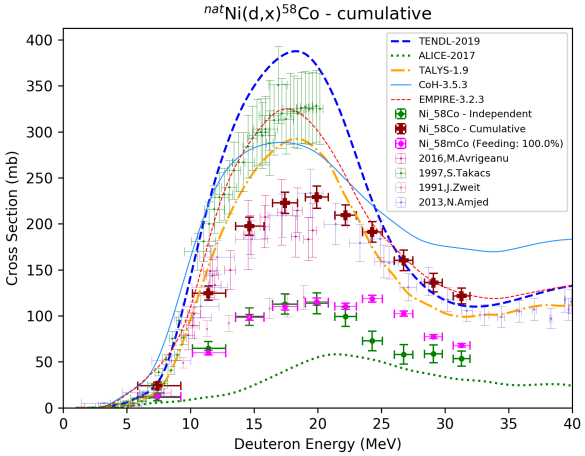

Figure E.18: The excitation function for ^{nat}Ni(d,x)^{58}Co (cumulative).

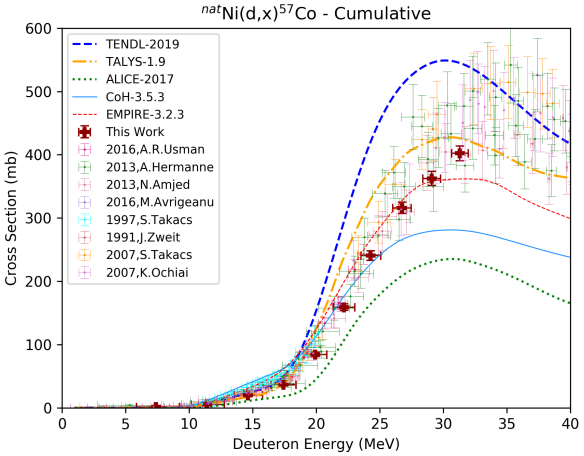

Figure E.19: The excitation function for ^{nat}Ni(d,x)^{57}Co.

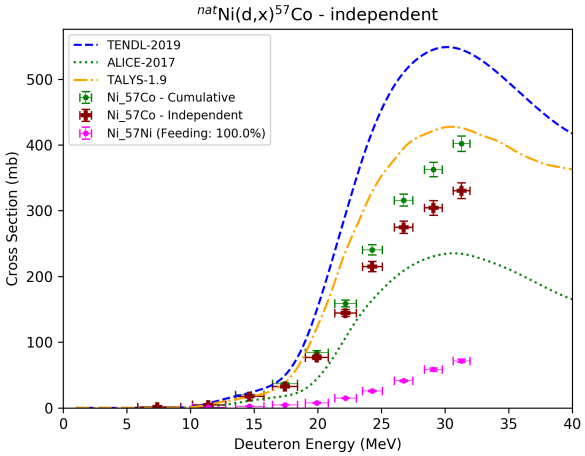

Figure E.20: The excitation function for ^{nat}Ni(d,x)^{58}Co (cumulative).

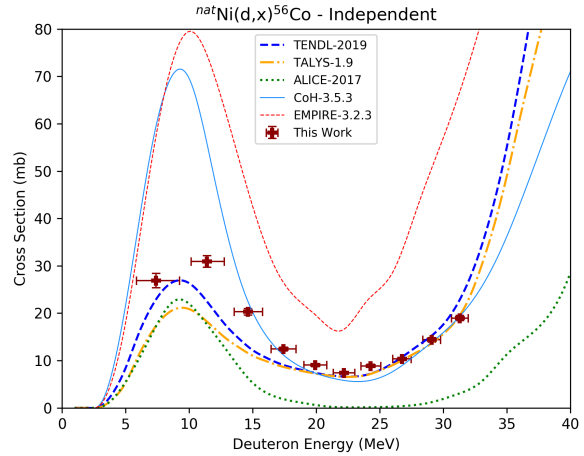

Figure E.21: The excitation function for ^{nat}Ni(d,x)^{56}Co (independent).

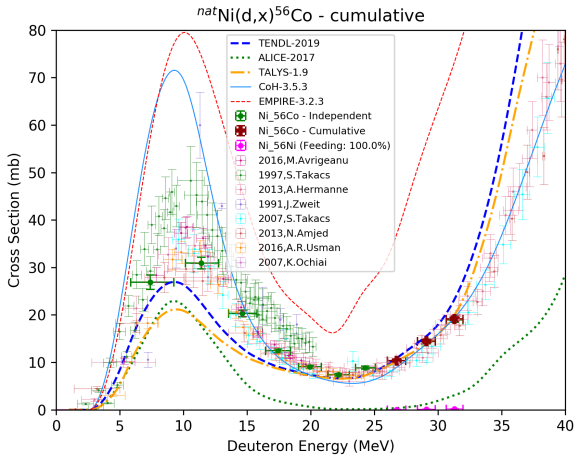

Figure E.22: The excitation function for ^{nat}Ni(d,x)^{56}Co (cumulative).

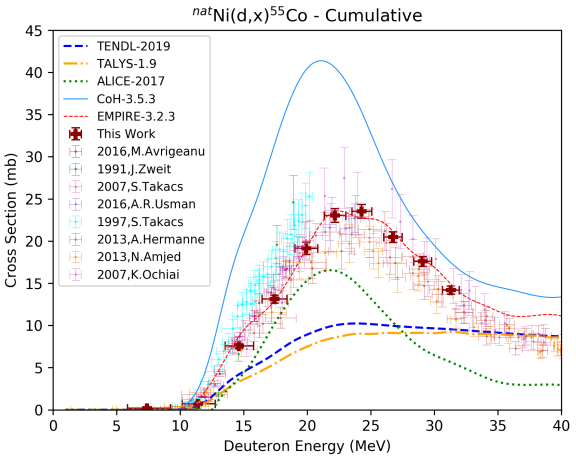

Figure E.23: The excitation function for ^{nat}Ni(d,x)^{55}Co.

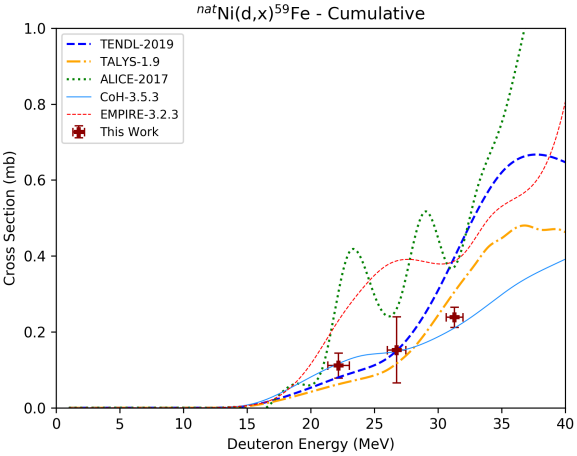

Figure E.24: The excitation function for ^{nat}Ni(d,x)^{59}Fe.

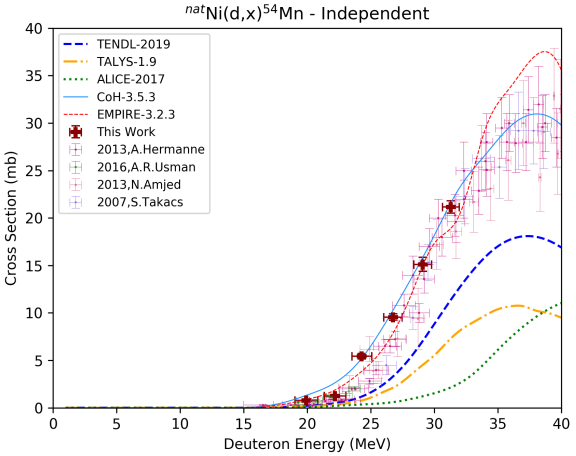

Figure E.25: The excitation function for ^{nat}Ni(d,x)^{54}Mn.

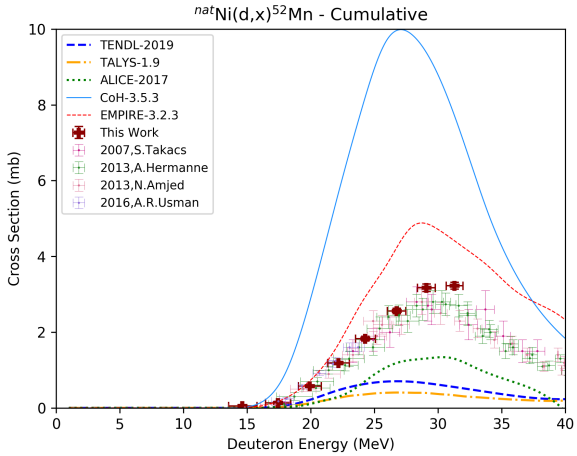

Figure E.26: The excitation function for ^{nat}Ni(d,x)^{52}Mn.

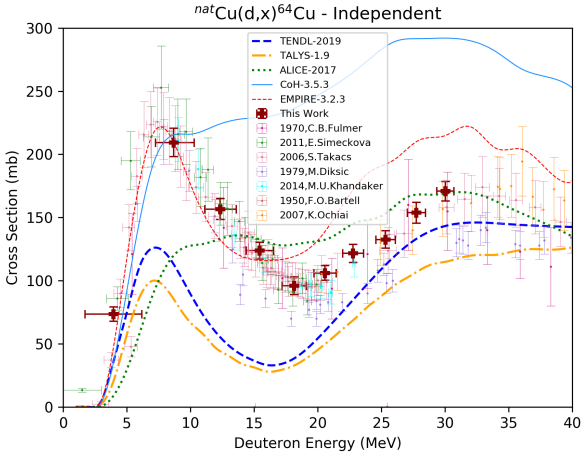

Figure E.27: The excitation function for $^{\text{nat}}$Cu(d,x)^{64}Cu.

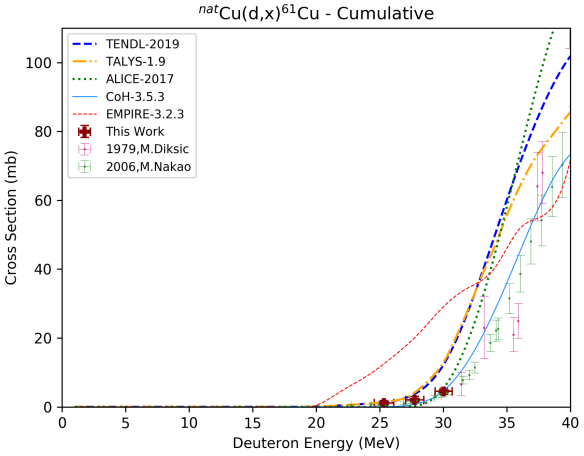

Figure E.28: The excitation function for $^{\text{nat}}$Cu(d,x)^{61}Cu.

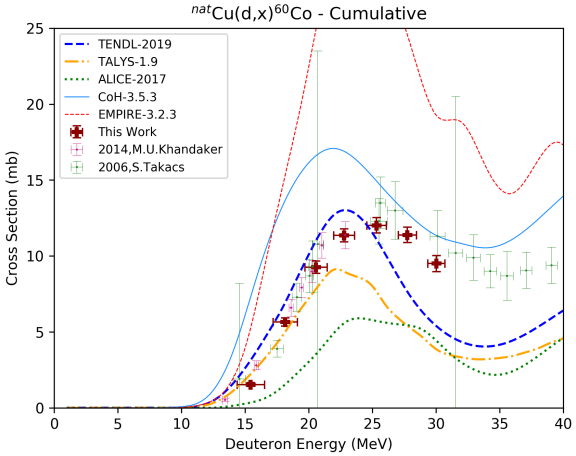

Figure E.29: The excitation function for $^{\text{nat}}$Cu(d,x)^{60}Co.

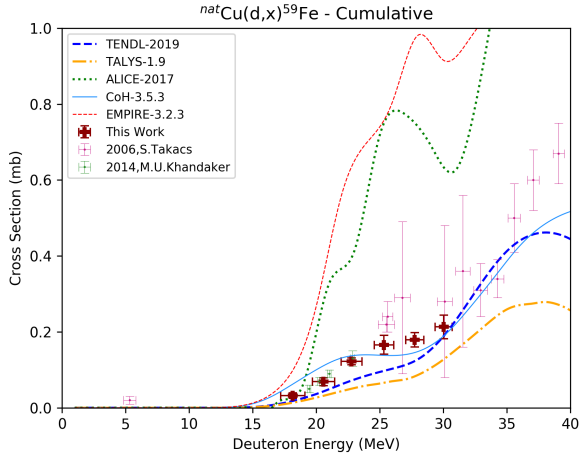

Figure E.30: The excitation function for $^{\text{nat}}$Cu(d,x)^{59}Fe.

Bibliography

[1] *Advancing Nuclear Medicine Through Innovation*. National Academies Press, Washington, D.C., sep. (Chapter 2).

[2] World Nuclear Association. Radioisotopes in Medicine. https://www.world-nuclear.org/information-library/non-power-nuclear-applications/radioisotopes-research/radioisotopes-in-medicine.aspx. Accessed: 2020-05-21.

[3] Dandamudi V. Howell, Roger W., Sastry, Kandula, S. R., Hill, Helene Z. , Rao. CIS-PLATINUM-193m: Its microdosimetry and potential for chemo-auger combination therapy of cancer. In Evelyn E. Schlafke-Stelson, Audrey T., Watson, editor, *Fourth International Radiopharmaceutical Dosimetry Symposium*. Oak Ridge, Tennessee, 4 edition, 1985.

[4] M. Shamsuzzoha Basunia. Nuclear Data Sheets for A=193. *Nuclear Data Sheets*, 143:1–381, jul 2017.

[5] Eric J. Hall. *Radiobiology for the radiologist*. Wolters Kluwer Health, 2018.

[6] World Health Organization. Cancer. https://www.who.int/news-room/fact-sheets/detail/cancer. Accessed: 2020-05-24.

[7] World Health Organization, Regional Office for Europe. Data and statistics. http://www.euro.who.int/en/health-topics/noncommunicable-diseases/cancer/data-and-statistics. Accessed: 2020-05-25.

[8] R. Qaim, S. M., TÁrkányi, F, Capote, editor. *Nuclear Data for the Production of Therapeutic Radionuclides*. Number 473 in Technical Reports Series. Internation Atomic Energy Agency, Vienna, 2011.

[9] Syed M. Qaim. Nuclear data for production and medical application of radionuclides: Present status and future needs. *Nuclear Medicine and Biology*, 44:31–49, jan 2017.

[10] Chai-Hong Yeong, Mu-hua Cheng, and Kwan-Hoong Ng. Therapeutic radionuclides in nuclear medicine: current and future prospects. *Journal of Zhejiang University Science B*, 15(10):845–863, oct 2014.

[11] F. Tárkányi, B. Király, F. Ditrói, S. Takács, J. Csikai, A. Hermanne, M. S. Uddin, M. Hagiwara, M. Baba, Yu N. Shubin, and S. F. Kovalev. Cross sections of deuteron induced nuclear reactions on iridium. *Nuclear Instruments and Methods in Physics Research, Section B: Beam Interactions with Materials and Atoms*, 247(2):210–216, 2006.

[12] F. Tárkányi, A. Hermanne, F. Ditrói, S. Takács, and A.V. Ignatyuk. Measurement of activation cross sections of deuteron induced reactions on natIr in the 17–50 MeV energy range. *Nuclear Instruments and Methods in Physics Research Section B: Beam Interactions with Materials and Atoms*, 458:105–117, nov 2019.

[13] M. Herman, R. Capote, B.V. Carlson, P. Obložinský, M. Sin, A. Trkov, H. Wienke, and V. Zerkin. EMPIRE: Nuclear Reaction Model Code System for Data Evaluation. *Nuclear Data Sheets*, 108(12):2655–2715, dec 2007.

[14] Toshihiko Kawano, Patrick Talou, Mark B. Chadwick, and Takehito Watanabe. Monte Carlo Simulation for Particle and γ-Ray Emissions in Statistical Hauser-Feshbach Model. *Journal of Nuclear Science and Technology*, 47(5):462–469, may 2010.

[15] M. Blann. New precompound decay model. *Physical Review C*, 54(3):1341–1349, sep 1996.

[16] A.J. Koning and D. Rochman. Modern Nuclear Data Evaluation with the TALYS Code System. *Nuclear Data Sheets*, 113(12):2841–2934, dec 2012.

[17] A.J. Koning, D. Rochman, J.-Ch. Sublet, N. Dzysiuk, M. Fleming, and S. van der Marck. TENDL: Complete Nuclear Data Library for Innovative Nuclear Science and Technology. *Nuclear Data Sheets*, 155:1–55, jan 2019.

[18] Andrew S. Voyles. *Nuclear Excitation Functions for the Production of Novel Medical Radionuclides*. PhD thesis, UC Berkeley, 2018. Retrieved from https://escholarship.org/uc/item/3nd6913p.

[19] Attila Vértes, Sándor Nagy, Zoltán Klencsár, Rezső G. Lovas, and Frank Rösch, editors. *Handbook of Nuclear Chemistry*. Springer US, Boston, MA, second edition, 2011.

[20] Shankar Vallabhajosula. *Molecular Imaging*. Springer Berlin Heidelberg, Berlin, Heidelberg, 2009.

[21] Jyothi Thundimadathil. Cancer Treatment Using Peptides: Current Therapies and Future Prospects. *Journal of Amino Acids*, 2012:1–13, 2012.

[22] Frank Rösch, Hans Herzog, and Syed Qaim. The Beginning and Development of the Theranostic Approach in Nuclear Medicine, as Exemplified by the Radionuclide Pair 86Y and 90Y. *Pharmaceuticals*, 10(4):56, jun 2017.

[23] M. Alotiby. *Accurately determining the number of Auger electrons per nuclear decay for medical isotopes*. PhD thesis, Australian National University, 2019.

[24] C. Hillyar. *Auger electron radionuclide therapy utilising F3 peptide to target the nucleolus*. PhD thesis, University of Oxford, 2015.

[25] Jean-Pierre Pouget, Isabelle Navarro-Teulon, Manuel Bardiès, Nicolas Chouin, Guillaume Cartron, André Pèlegrin, and David Azria. Clinical radioimmunotherapy—the role of radiobiology. *Nature Reviews Clinical Oncology*, 8(12):720–734, dec 2011.

[26] Kenneth S. Krane. *Introductory Nuclear Physics*. John Wiley & Sons, Inc., 1988.

[27] William R. Leo. *Techniques for Nuclear and Particle Physics Experiments*. Springer Berlin Heidelberg, Berlin, Heidelberg, 1994.

[28] Stephen A. Graves, Paul A. Ellison, Todd E. Barnhart, Hector F. Valdovinos, Eva R. Birnbaum, Francois M. Nortier, Robert J. Nickles, and Jonathan W. Engle. Nuclear excitation functions of proton-induced reactions (Ep= 35–90 MeV) from Fe, Cu, and Al. *Nuclear Instruments and Methods in Physics Research Section B: Beam Interactions with Materials and Atoms*, 386:44–53, nov 2016.

[29] J. M. Koning, A. J., Akkermans. *Pre-equilibrium nuclear reactions: An introduction to classical and quantum-mechanical models*. 1999.

[30] Antonio Moro. Models for nuclear reactions with weakly-bound systems. 07 2018. Scientic figure from resarchgate: https://www.researchgate.net/figure/Direct-and-compound-nucleus-reaction-channels-taking-place-in-a-d-10-Be-reaction_fig8_326366718. Accessed: 2020-05-13.

[31] IAEA. Cyclotron produced radionuclides: Physical characteristics and production methods. *Technical Reports series*, 468, 2009.

[32] Toshihiko Kawano. CoH: The Hauser-Feshbach-Moldauer statistical model with the coupled-channels theory. *Los Alamos National Laboratory, unpublished*, 2003.

[33] Andrew S Voyles, Amanda M Lewis, Jonathan T Morrell, M Shamsuzzoha Basunia, Lee A Bernstein, Jonathan W Engle, Stephen A Graves, and Eric F Matthews. Proton-induced reactions on fe, cu, & ti from threshold to 55 mev. *arXiv preprint arXiv:1910.11135*, 2019.

[34] Walter Hauser and Herman Feshbach. The inelastic scattering of neutrons. *Phys. Rev.*, 87:366–373, Jul 1952.

[35] Marshall Blann. Preequilibrium decay. *Annual Review of Nuclear Science*, 25(1):123–166, 1975.

[36] V. F. Weisskopf and D. H. Ewing. On the yield of nuclear reactions with heavy elements. *Phys. Rev.*, 57:472–485, Mar 1940.

[37] Johan Areberg, Kristina Norrgren, and Sören Mattsson. Absorbed doses to patients from 191pt-, 193mpt- and 195mpt-cisplatin. *Applied Radiation and Isotopes*, 51:581–586, nov 1999.

[38] Adisorn Ratanaphan. A DNA Repair Protein BRCA1 as a Potentially Molecular Target for the Anticancer Platinum Drug Cisplatin. In *DNA Repair*. InTech, nov 2011.

[39] Michael T. Azure, Kandula S. R. Sastry, Ronald D. Archer, W. Howeel, and Dandamudi V. Rao. Microscale synthesis of carboplatin labeled with the auger emitter platinum-193m: Radiotoxicity versus chemotoxicity of the antitumor drug in mammalian cells. *Biophysical Aspects of Auger Processes, AAPM Symposium Series no. 8*, 1992.

[40] K. Hilgers, H. H. Coenen, and S. M. Qaim. Production of the therapeutic radionuclides 193mPt and 195mPt with high specific activity via α-particle-induced reactions on 192Os. *Applied Radiation and Isotopes*, 66(4):545–551, 2008.

[41] M.S. Uddin, B. Scholten, A. Hermanne, S. Sudár, H.H. Coenen, and S.M. Qaim. Radiochemical determination of cross sections of α-particle induced reactions on 192os for the production of the therapeutic radionuclide 193mpt. *Applied Radiation and Isotopes*, 68(10):2001–2006, oct 2010.

[42] A.S. Voyles, M.S. Basunia, J.C. Batchelder, J.D. Bauer, T.A. Becker, L.A. Bernstein, E.F. Matthews, P.R. Renne, D. Rutte, M.A. Unzueta, and K.A. van Bibber. Measurement of the 64Zn,47Ti(n,p) cross sections using a DD neutron generator for medical isotope studies. *Nuclear Instruments and Methods in Physics Research Section B: Beam Interactions with Materials and Atoms*, 410:230–239, nov 2017.

[43] Lidija Vrapcenjak and Viktor Zerkin. NuDat 2.8. https://www.nndc.bnl.gov, 2015.

[44] Roger W. Howell, Dandamudi V. Rao, De-Yan Hou, Venkat R. Narra, and Kandula S. R. Sastry. The Question of Relative Biological Effectiveness and Quality Factor for Auger Emitters Incorporated into Proliferating Mammalian Cells. *Radiation Research*, 128(3):282, dec 1991.

[45] Roger W. Howell. Radiation spectra for Auger-electron emitting radionuclides: Report No. 2 of AAPM Nuclear Medicine Task Group No. 6. *Medical Physics*, 19(6):1371–1383, nov 1992.

[46] Franz Buchegger, Florence Perillo-Adamer, Yves M. Dupertuis, and Angelika Bischof Delaloye. Auger radiation targeted into DNA: a therapy perspective. *European Journal of Nuclear Medicine and Molecular Imaging*, 33(11):1352–1363, oct 2006.

[47] Jonathan T. Morrell, Andrew S. Voyles, M. S. Basunia, Jon C. Batchelder, Eric F. Matthews, and Lee A. Bernstein. Measurement of 139La(p,x) cross sections from 35–60 MeV by stacked-target activation. *European Physical Journal A*, 56(1), 2020.

[48] Andrew S. Voyles, Lee A. Bernstein, Eva R. Birnbaum, Jonathan W. Engle, Stephen A. Graves, Toshihiko Kawano, Amanda M. Lewis, and Francois M. Nortier. Excitation functions for (p,x) reactions of niobium in the energy range of Ep = 40–90 MeV. *Nuclear Instruments and Methods in Physics Research Section B: Beam Interactions with Materials and Atoms*, 429:53–74, aug 2018.

[49] A. Hermanne, A.V. Ignatyuk, R. Capote, B.V. Carlson, J.W. Engle, M.A. Kellett, T. Kibédi, G. Kim, F.G. Kondev, M. Hussain, O. Lebeda, A. Luca, Y. Nagai, H. Naik, A.L. Nichols, F.M. Nortier, S.V. Suryanarayana, S. Takács, F.T. Tárkányi, and M. Verpelli. Reference Cross Sections for Charged-particle Monitor Reactions. *Nuclear Data Sheets*, 148:338–382, feb 2018.

[50] M. Kireeff Covo, R. A. Albright, B. F. Ninemire, M. B. Johnson, A. Hodgkinson, T. Loew, J. Y. Benitez, D. S. Todd, D. Z. Xie, T. Perry, L. Phair, L. A. Bernstein, J. Bevins, J. A. Brown, B. L. Goldblum, M. Harasty, K. P. Harrig, T. A. Laplace, E. F. Matthews, A. Bushmaker, D. Walker, V. Oklejas, A. R. Hopkins, D. L. Bleuel, J. Chen, and S. B. Cronin. The 88-Inch Cyclotron: A one-stop facility for electronics radiation and detector testing. *Measurement: Journal of the International Measurement Confederation*, 127:580–587, 2018.

[51] Lawrence Berkeley Laboratory. Berkeley lab - About the lab. https://www.lbl.gov/about/. Accessed: 2020-05.04.

[52] Lawrence Berkeley Laboratory. 88-Inch Cyclotron. http://cyclotron.lbl.gov/home. Accessed: 2020-05-20.

[53] I Y Lee, M A Deleplanque, and K Vetter. Developments in large gamma-ray detector arrays. *Reports on Progress in Physics*, 66(7):1095–1144, jul 2003.

[54] Gordon R. Gilmore. *Practical Gamma-ray Spectroscopy*. John Wiley & Sons, Ltd, second edition, 2008.

[55] J. Fitzgerald. FitzPeaks gamma aualysis and calibration software. 2009.

[56] E. Browne and J.K. Tuli. Nuclear Data Sheets for A = 137. *Nuclear Data Sheets*, 108(10):2173–2318, oct 2007.

[57] Yu. Khazov, A. Rodionov, and F.G. Kondev. Nuclear Data Sheets for A = 133. *Nuclear Data Sheets*, 112(4):855–1113, apr 2011.

[58] M.J. Martin. Nuclear Data Sheets for A = 152. *Nuclear Data Sheets*, 114(11):1497–1847, nov 2013.

[59] William J. Gallagher and Sam J. Cipolla. A model-based efficiency calibration of a Si(Li) detector in the energy region from 3 to 140 keV. *Nuclear Instruments and Methods*, 122:405–414, nov 1974.

[60] Matthews, Eric F., Lewis, Amanda M. and Bernstein, Lee A. Significance of gamma-ray detector efficiency calibration bias on nuclear astrophysics and nuclear data evaluations. 2020. (preprint).

[61] Pauli Virtanen, Ralf Gommers, Travis E. Oliphant, Matt Haberland, Tyler Reddy, David Cournapeau, Evgeni Burovski, Pearu Peterson, Warren Weckesser, Jonathan Bright, Stéfan J. van der Walt, Matthew Brett, Joshua Wilson, K. Jarrod Millman, Nikolay Mayorov, Andrew R. J. Nelson, Eric Jones, Robert Kern, Eric Larson, C J Carey, İlhan Polat, Yu Feng, Eric W. Moore, Jake VanderPlas, Denis Laxalde, Josef Perktold, Robert Cimrman, Ian Henriksen, E. A. Quintero, Charles R. Harris, Anne M. Archibald, Antônio H. Ribeiro, Fabian Pedregosa, and Paul van Mulbregt. SciPy 1.0: fundamental algorithms for scientific computing in Python. *Nature Methods*, 17(3):261–272, mar 2020.

[62] Coral M. Baglin. Nuclear Data Sheets for A = 192. *Nuclear Data Sheets*, 113(8-9):1871–2111, aug 2012.

[63] Bai Erjun and Huo Junde. Nuclear Data Sheets for A = 63. *Nuclear Data Sheets*, 92(1):147–252, jan 2001.

[64] Kazimierz Zuber and Balraj Singh. Nuclear Data Sheets for A = 61. *Nuclear Data Sheets*, 125:1–200, mar 2015.

[65] Alan L. Nichols, Balraj Singh, and Jagdish K. Tuli. Nuclear Data Sheets for A = 62. *Nuclear Data Sheets*, 113(4):973–1114, apr 2012.

[66] Wayne Rasband. ImageJ 1.52K, 2010.

[67] R.B. Chu, S.Y.F, Ekström, L.P., Firestone. The LUND/LBNL Nuclear Data Search. http://nucleardata.nuclear.lu.se/toi, 1999.

[68] Brookhaven National Laboratory Pritychenko, B., Sonzogni, A., NNDC. Q-value Calculator (Q-calc). https://www.nndc.bnl.gov/qcalc.

[69] M.J. Berger, J.H. Hubbell, S.M. Seltzer, J. Chang, J.S. Coursey, R. Sukumar, D.S. Zucker and K. Olsen. XCOM: Photon Cross Sections Database, 2010.

[70] O.M. Pop, V.M. Simulik, and M.V. Stets. Nuclide Spectra of Activities of Thorium, Uranium Series and Application in Gamma-spectroscopy of Point Technogenic Samples. *International Journal of Physics, 2016, Vol. 4, No. 2, 37-42*, 2016.

[71] Caroline D. Nesaraja, Scott D. Geraedts, and Balraj Singh. Nuclear Data Sheets for A = 58. *Nuclear Data Sheets*, 111(4):897–1092, apr 2010.

[72] Huo Junde, Huo Su, and Yang Dong. Nuclear Data Sheets for A = 56. *Nuclear Data Sheets*, 112(6):1513–1645, jun 2011.

[73] Morell, Jonathan T. NPAT: Nuclear Physics Analysis Tool. https://pypi.org/project/npat/, 2019.

[74] E. Browne and J.K. Tuli. Nuclear Data Sheets for A = 65. *Nuclear Data Sheets*, 111(9):2425–2553, sep 2010.

[75] J. F. Ziegler. Stopping of energetic light ions in elemental matter. *Journal of Applied Physics*, 85(3):1249–1272, feb 1999.

[76] J.F. Ziegler and J.P. Biersack. *Treatise on Heavy-Ion Science: Volume 6: Astrophysics, Chemistry, and Condensed Matter*. Springer US Boston, MA, 1985.

[77] Stéfan van der Walt, S Chris Colbert, and Gaël Varoquaux. The NumPy Array: A Structure for Efficient Numerical Computation. *Computing in Science & Engineering*, 13(2):22–30, mar 2011.

[78] Experimental nuclear reaction data (exfor). https://www-nds.iaea.org/exfor/, 2020.

[79] S. Takács, F. Tárkányi, B. Király, A. Hermanne, and M. Sonck. Evaluated activation cross sections of longer-lived radionuclides produced by deuteron-induced reactions on natural copper. *Nuclear Instruments and Methods in Physics Research Section B: Beam Interactions with Materials and Atoms*, 251(1):56–65, sep 2006.

[80] K. Ochiai, M. Nakao, N. Kubota, S. Sato, M. Yamauchi, N. H. Ishioka, T. Nishitani, and C. Konno. Deuteron induced activation cross section measurement for IFMIF. In *ND2007*, Les Ulis, France, may 2007. EDP Sciences.

[81] Mayeen Uddin Khandaker, Hiromitsu Haba, Jumpei Kanaya, and Naohiko Otuka. Activation cross-sections of deuteron-induced nuclear reactions on natural iron up to 24MeV. *Nuclear Instruments and Methods in Physics Research Section B: Beam Interactions with Materials and Atoms*, 316:33–41, dec 2013.

[82] M. Avrigeanu, V. Avrigeanu, P. Bém, U. Fischer, M. Honusek, K. Katovsky, C. Mănăilescu, J. Mrázek, E. Šimečková, and L. Závorka. Low energy deuteron-induced reactions on Fe isotopes. *Physical Review C*, 89(4):044613, apr 2014.

[83] S. Takács, M. Sonck, A. Azzam, A. Hermanne, and F. Tárkányi. Activation Gross Section Measurements of Deuteron Induced Reactions on nat Ni with Special Reference to Beam Monitoring and Production of for 61Cu Medical Purpose. *Radiochimica Acta*, 76(1-2), jan 1997.

[84] B. Király, S. Takács, F. Ditrói, F. Tárkányi, and A. Hermanne. Evaluated activation cross sections of longer-lived radionuclides produced by deuteron induced reactions on natural iron up to 10MeV. *Nuclear Instruments and Methods in Physics Research Section B: Beam Interactions with Materials and Atoms*, 267(1):15–22, jan 2009.

[85] J. W. Clark, C. B. Fulmer, and I. R. Williams. Excitation Functions for Radioactive Nuclides Produced by Deuteron-Induced Reactions in Iron. *Physical Review*, 179(4):1104–1108, mar 1969.

[86] S Takács, F Szelecsényi, F Tárkányi, M Sonck, A Hermanne, Yu Shubin, A Dityuk, M.G Mustafa, and Zhuang Youxiang. New cross-sections and intercomparison of deuteron monitor reactions on Al, Ti, Fe, Ni and Cu. *Nuclear Instruments and Methods in Physics Research Section B: Beam Interactions with Materials and Atoms*, 174(3):235–258, apr 2001.

[87] M. Avrigeanu, E. Šimečková, U. Fischer, J. Mrázek, J. Novak, M. Štefánik, C. Costache, and V. Avrigeanu. Deuteron-induced reactions on Ni isotopes up to 60 MeV. *Physical Review C*, 94(1):014606, jul 2016.

[88] A. Hermanne, S. Takács, R. Adam-Rebeles, F. Tárkányi, and M.P. Takács. New measurements and evaluation of database for deuteron induced reaction on Ni up to 50MeV. *Nuclear Instruments and Methods in Physics Research Section B: Beam Interactions with Materials and Atoms*, 299:8–23, mar 2013.

[89] S. Takács, F. Tárkányi, B. Király, A. Hermanne, and M. Sonck. Evaluated activation cross sections of longer-lived radionuclides produced by deuteron induced reactions on natural nickel. *Nuclear Instruments and Methods in Physics Research Section B: Beam Interactions with Materials and Atoms*, 260(2):495–507, jul 2007.

[90] Ahmed Rufai Usman, Mayeen Uddin Khandaker, Hiromitsu Haba, Masashi Murakami, and Naohiko Otuka. Measurements of deuteron-induced reaction cross-sections on natural nickel up to 24 MeV. *Nuclear Instruments and Methods in Physics Research Section B: Beam Interactions with Materials and Atoms*, 368:112–119, feb 2016.

[91] J. Zweit, A.M. Smith, S. Downey, and H.L. Sharma. Excitation functions for deuteron induced reactions in natural nickel: Production of no-carrier-added 64Cu from enriched 64Ni targets for positron emission tomography. *International Journal of Radiation Applications and Instrumentation. Part A. Applied Radiation and Isotopes*, 42(2):193–197, jan 1991.

[92] N. Amjed, F. Tárkányi, F. Ditrói, S. Takács, and H. Yuki. Activation cross-sections of deuteron induced reaction of natural Ni up to 40MeV. *Applied Radiation and Isotopes*, 82:87–99, dec 2013.

[93] Mayeen Uddin Khandaker, Hiromitsu Haba, Masashi Murakami, Naohiko Otuka, and Hasan Abu Kassim. Deuteron-induced activation cross-sections on natural copper up to 24 MeV. *Journal of Radioanalytical and Nuclear Chemistry*, 302(2):759–764, nov 2014.

[94] F. O. Bartell, A. C. Helmholz, S. D. Softky, and D. B. Stewart. Excitation Functions for Spallation Reactions on Cu. *Physical Review*, 80(6):1006–1010, dec 1950.

[95] M. Nakao, J. Hori, K. Ochiai, N. Kubota, S. Sato, M. Yamauchi, N.S. Ishioka, and T. Nishitani. Measurements of deuteron-induced activation cross-sections for IFMIF accelerator structural materials. *Nuclear Instruments and Methods in Physics Research Section A: Accelerators, Spectrometers, Detectors and Associated Equipment*, 562(2):785–788, jun 2006.

[96] C.B. Fulmer and I.R. Williams. Excitation functions for radioactive nucleides produced by deuteron-induced reactions in copper. *Nuclear Physics A*, 155(1):40–48, oct 1970.

[97] L. Weissman, A. Kreisel, T. Hirsh, O. Aviv, D. Berkovits, O. Girshevitz, and Y. Eisen. Accurate measurements of the 63Cu(d,p)64Cu and natCu(d,x)65Zn cross-sections in the 2.77–5.62MeV energy range. *Nuclear Instruments and Methods in Physics Research Section B: Beam Interactions with Materials and Atoms*, 342:7–12, jan 2015.

[98] V.R. Vanin, N.L. Maidana, R.M. Castro, E. Achterberg, O.A. Capurro, and G.V. Martí. Nuclear Data Sheets for A = 191. *Nuclear Data Sheets*, 108(11):2393–2588, nov 2007.

[99] F.G. Kondev, S. Juutinen, and D.J. Hartley. Nuclear Data Sheets for A=188. *Nuclear Data Sheets*, 150:1–364, may 2018.

[100] T.D. Johnson and Balraj Singh. Nuclear Data Sheets for A=189. *Nuclear Data Sheets*, 142:1–330, may 2017.

[101] Balraj Singh. Nuclear Data Sheets for A = 190. *Nuclear Data Sheets*, 99(2):275–481, jun 2003.

[102] Balraj Singh. Nuclear Data Sheets for A = 194. *Nuclear Data Sheets*, 107(6):1531–1746, jun 2006.

[103] G. L. Squires. *Practical Physics*. Cambridge University Press, fourth edition, 2001.

[104] Michael Dobbert and Bart Schrijver. Uncertainty Propagation for Measurements with Multiple Output Quantities. (2).

[105] Markku J. Koskelo, Pertti A. Aarnio, and Jorma T. Routti. SAMPO80: An accurate gamma spectrum analysis method for minicomputers. *Nuclear Instruments and Methods in Physics Research*, 190(1):89–99, nov 1981.

[106] T.W. Burrows. Nuclear Data Sheets for A = 48. *Nuclear Data Sheets*, 107(7):1747–1922, jul 2006.

[107] Jimin Wang and Xiaolong Huang. Nuclear Data Sheets for A = 51. *Nuclear Data Sheets*, 144:1–296, sep 2017.

[108] Yang Dong and Huo Junde. Nuclear Data Sheets for A = 52. *Nuclear Data Sheets*, 128:185–314, sep 2015.

[109] Yang Dong and Huo Junde. Nuclear Data Sheets for A = 54. *Nuclear Data Sheets*, 121:1–142, sep 2014.

[110] Huo Junde. Nuclear Data Sheets for A = 53. *Nuclear Data Sheets*, 110(11):2689–2814, nov 2009.

[111] M. Shamsuzzoha Basunia. Nuclear Data Sheets for A=59. *Nuclear Data Sheets*, 151:1–333, jul 2018.

[112] Huo Junde. Nuclear Data Sheets for A = 55. *Nuclear Data Sheets*, 109(4):787–942, apr 2008.

[113] M.R. Bhat. Nuclear Data Sheets for A = 57. *Nuclear Data Sheets*, 85(3):415–536, nov 1998.

[114] E. Browne and J.K. Tuli. Nuclear Data Sheets for A = 60. *Nuclear Data Sheets*, 114(12):1849–2022, dec 2013.

[115] Balraj Singh. Nuclear Data Sheets for A = 64. *Nuclear Data Sheets*, 108(2):197–364, feb 2007.

[116] S. Sudár and S. M. Qaim. Isomeric cross-section ratio for the formation of 58Comg in neutron, proton, deuteron, and alpha-particle induced reactions in the energy region up to 25 MeV. *Physical Review C*, 53(6):2885–2892, jun 1996.

[117] A Hermanne, M Sonck, S Takács, and F Tárkányi. Experimental study of excitation functions for some reactions induced by deuterons (10–50 Mev) on natural Fe and Ti. *Nuclear Instruments and Methods in Physics Research Section B: Beam Interactions with Materials and Atoms*, 161-163:178–185, mar 2000.

[118] S. Sudár and S. M. Qaim. Excitation functions of proton and deuteron induced reactions on iron and alpha-particle induced reactions on manganese in the energy region up to 25 MeV. *Physical Review C*, 50(5):2408–2419, nov 1994.

[119] E. Šimečková, P. Bém, M. Honusek, M. Štefánik, U. Fischer, S. P. Simakov, R. A. Forrest, A. J. Koning, J.-C. Sublet, M. Avrigeanu, F. L. Roman, and V. Avrigeanu. Low and medium energy deuteron induced reactions on cu63,65 nuclei. *Physical Review C*, 84(1):014605, jul 2011.

[120] Mirko Dikšić, Jean-Louis Galinier, Heather Marshall, Leo Yaffe, Robert B. Moore, and Dallas C. Santry. Absolute cross sections for 64Cu and 61Cu produced by deuteron-induced reactions in copper. *Nuclear Instruments and Methods*, 159(1):171–175, feb 1979.